

國立交通大學

光電工程研究所

博士論文

快速響應、高對比、超輕薄之
向列型液晶顯示元件

*Fast Switching, High Optical Contrast, and Slim Form Factor
Nematic Liquid Crystal Display Devices*

研究生：楊柏儒

指導教授：謝漢萍教授

中華民國九十七年十月

快速響應、高對比、超輕薄之
向列型液晶顯示元件

*Fast Switching, High Optical Contrast, and Slim Form Factor
Nematic Liquid Crystal Display Devices*

研究生：楊柏儒
指導教授：謝漢萍

Student : Bo-Ru Yang
Advisor : Han-Ping D. Shieh

國立交通大學
光電工程研究所
博士論文

A Thesis
Submitted to Institute of Electro-Optical Engineering
College of Electrical and Computer Engineering
National Chiao Tung University
for the Degree of Doctor of Philosophy
in
Department of Photonics
2008
Hsinchu, Taiwan, Republic of China

中華民國 九十七 年 十 月

快速響應、高對比、超輕薄之 向列型液晶顯示元件

博士研究生：楊柏儒

指導教授：謝漢萍教授

國立交通大學

光電工程研究所

摘 要

本論文的主要研究目標在於探究一個液晶元件在顯示性能上面的極限。其中，我們特別針對向列型液晶元件在快速響應、高對比、輕薄化這些特徵上面做了深入的研究。

快速響應能力是實踐色序法驅動及時域分割之立體顯示技術的重要決定因素。而光學補償彎曲模態(optically compensated bend, OCB)是現階段響應速度最快的向列型液晶模態，因此，其被視為是最有可能用來實現上述之新穎顯示技術的液晶模態。不過，由於此液晶模態會有態間回復(inter-state recovery)的問題，使得應用上面困難重重。因此，在此論文中，我們提出利用水平對稱模態(symmetric H, Hs)以及高分子安定化之光學補償彎曲模態來避免態間回復的問題。採用水平對稱模態的難處在於其存在時間很短，因此，我們以一種搭配閃頻光源的錐光偏振儀來捕捉其暫態的液晶分子排列，並利用此結果，設計出一種高分子牆結構來延長其存在時間。藉由模擬顯示，利用這種設計結構，其存在時間可以延長十倍以上。

高對比是一個液晶顯示元件在表現生動影像時不可或缺的要素。在此論文中，我們提出兩個方法來提升影像對比。一個方法是將光學補償彎曲模態的液晶元件，藉由高分子反應，使其原來是暫態的鬆弛彎曲態(relaxed bend state)安定下

來，由於鬆弛彎曲態具有高亮度的特性，因此，此安定化之後的液晶元件比傳統的高分子安定化元件於對比度方面至少提升 1.5 倍。另一個方法則是利用體散射層(volumetric scattering layer)來反射外界環境光，使炫光效應減少，因此，在日光下的對比度可以提升 12 倍。

輕量化與薄型化在行動顯示技術上面是極其重要的一環。我們在此提出將厚重的背光模組直接以輕薄的有機發光二極體(organic light emitting diode, OLED)取代。並且，更直接地將有機發光元件嵌入液晶顯示元件中，如此，其體積與重量將大幅減少。同時，此整合元件的有機發光二極體部分在暗態操作下可以將光源關掉，反觀現行的透反式(trans-flective)顯示器，在暗態下，其背光仍處於打開的狀態，因此，我們提出的整合元件同時可以在對比上大幅提昇、耗電量也可以減少許多。

本論文在科學上的貢獻在於提出一種利用閃頻光源來觀察甚至穩定本來只能暫時存在的液晶模態，此方法在液晶科學方面開創了一個新的研究領域。而在技術上，我們成功地實現了將有機發光元件嵌入液晶元件，並進一步地以體散射層來優化其光學性能，這在有機發光二極體的研究領域上是個重要的突破。最後，倘若整合所有本論文中得到的研究成果，我們將可以製作出一個具有高影像品質、低耗電、極輕薄且可撓式的新穎液晶顯示元件。

Fast Switching, High Optical Contrast, and Slim Form Factor Nematic Liquid Crystal Display Devices

Doctoral Student: Bo-Ru Yang

Advisor: Prof. Han-Ping D. Shieh

**Institute of Electro-Optical Engineering
National Chiao Tung University**

Abstract

The main objective of this dissertation is to explore the ultimate features of a liquid crystal display (LCD) device. Particular attention is spent on the nematic type LCD device with the attributes of fast-switching, high-optical-contrast, and slim-form-factor.

Fast-switching is a demanding requirement of an LCD device for realizing the novel display systems such as field sequential color LCD and temporally multiplexing 3D display. Regarding this requirement, pi-cell (also known as optically compensated bend, OCB) is the most promising LCD mode whose fast-switching results from its symmetric LC profile and parallel backflow. However, the issue of undesirable recovery hinders the pi-cell from commercial applications. In this thesis, we propose to use the symmetric H (Hs) state and the polymerized bend state to overcome this unwanted recovery. The difficulty of utilizing the Hs state results from its short lifetime. To resolve this issue, we propose a stroboscopic illumination assisted conoscopy to verify its transient LC profile. According to this result, we further design a polymer wall structure to extend its lifetime. With the verification of LCD simulation, the lifetime can be elongated by a factor of more than 10.

High-optical-contrast is a critical attribute for an LCD device to show a vivid image. Here, we propose two methods for enhancing the optical contrast in the

polymerized OCB-LCD and the organic light emitting diode (OLED) embedded LCD. In the polymerized OCB-LCD, we stabilize the relaxed bend state which has the highest brightness among the bend states. The optical contrast is enhanced by a factor of 1.5 compared with that of the conventionally polymerized OCB-LCD. In the OLED embedded LCD, after adopting the volumetric scattering layer (VSL), the optical contrast in the reflective mode is increased by a factor of 12.

Slim-form-factor is the most important factor as considering the mobile display applications. We propose and successfully accomplish the experiment of embedding an OLED directly into an LCD device, which thus eliminate the bulky backlight module. Meanwhile, the contrast ratio can be significantly increased compared with the case of trans-flective display. Because the OLED section can be turned off, whereas the conventional trans-flective display should sustain the backlight to be turned on even in the dark state. Referring to the neology of “trans-flective” display, we therefore term this OLED embedded LCD as “emi-flective” display, which is a combination of “emissive” and “reflective.”

Considering the scientific achievements, this dissertation demonstrates a stroboscopic illumination method, which opens a new era in observing and further stabilizing the transient states in an LCD device. As for the technical achievements, the realization of embedding the OLED into an LCD and the optical optimization with VSL have demonstrated a tremendous progress in OLED area. Combing these results, the integrated device is able to be low power consumption, high image quality, slim form factor, and fully flexible.

Acknowledgement

I would like to show my best gratitude to my thesis advisor, Prof. Han-Ping D. Shieh, for his guidance and support during my time as a PhD student. With his encouragement during these 4 years, I have not only cultivated my professional knowledge but also broadened my horizon through collaborating with industry, studying abroad, and taking an extra MBA program.

In addition, I would also like to acknowledge my supervisors at University of Oxford, Professors Peter Raynes and Steve Elston, and supervisors at Tohoku University, Professors Tatsuo Uchida and Tetsuya Miyashita for giving me the training and advices during my time studying at their groups. I further want to show my gratitude to National Science Council (Taiwan) and Interchange Association (Japan) for their financial supports which enable me to complete these visiting and exchanging programs.

This research work is supported by several colleagues including Jen-Chieh Hsieh, Kung-Yuen Lin, Chuan-Wei Hsu, and Shih-Nan Lee. Without their assistance, I would not be able to complete these tasks. I am also very grateful to my industrial colleagues including Sze-Feng Chen (CPT), Kung-Hun Liu, (ITRI), Chun-Hun Lee (Samsung), Wook-Sung Kim (LG Philips) for their valuable knowledge of display industry.

Lastly and most importantly, I am very thankful to my family members for their encouragement and supports.

Contents

Chapter 1 Introduction	1
1.1 The evolution of information display technology.....	1
1.2 Nematic liquid crystal display technologies	2
1.2.1 Fast-switching LC modes	2
1.2.2 High-contrast-ratio LCD technologies.....	5
1.2.3 Slim-form-factor devices for LCD backlight.....	7
1.3 Motivation and objectives.....	7
1.4 Organization of this thesis	9
Chapter 2 Theory and principle	11
2.1 Principle of mechanical design on LC cells.....	11
2.1.1 Continuum theory	11
2.1.2 Anchoring effect.....	14
2.1.3 Mechanical design of pi-cells.....	16
2.2 Principle of optical design on LC cells.....	19
2.2.1 Operational principle of an LCD device.....	19
2.2.2 Extended Jones matrix for light field distribution calculation.....	19
2.2.3 Principles of optical compensation	22
2.2.4 Optical compensation on pi-cells.....	27
Chapter 3 Device fabrication and measurements	29
3.1 Fabrication technologies	29
3.1.1 LCD device fabrication.....	29
3.1.2 OLED device fabrication	30
3.2 Measurement instruments	31
3.2.1 Conoscopic system.....	31
3.2.2 Spectroscopic ellipsometry	34
3.2.3 Focused ion beam assisted scanning electron microscopy	36

Chapter 4 High dynamic range LC mode in a pi-cell37

4.1 Introduction.....37

4.2 Preliminary observation on the relaxed bend state39

 4.2.1 Observation with the polarizers incorporated optical microscopy39

 4.2.2 Observation with the impulse driven pi-cell.....41

4.3 Fabrication of relaxed bend state stabilized pi-cell.....42

4.4 Confirmation of LC director profile by spectroscopic ellipsometry.....45

4.5 Results.....47

4.6 Discussion51

4.7 Summary52

Chapter 5 Investigation of symmetric H state in a pi-cell.....54

5.1 Introduction.....54

5.2 Investigation of the transient symmetric H state.....55

 5.2.1 An introduction of the symmetric H state.....55

 5.2.2 Preliminary observation on the symmetric H state.....57

 5.2.3 Stroboscopic illumination assisted conoscopy.....58

 5.2.4 Simulation on transient symmetric H state.....60

 5.2.5 Results of the investigation on symmetric H state.....61

5.3 Design for extending the lifetime of symmetric H state62

 5.3.1 A proposed structure for fixing the central LC director of Hs state.....62

 5.3.2 Simulation on the lifetime of proposed device structure63

 5.3.3 Polymer-stabilization without incorporating a photomask.....66

 5.3.4 Photomask assisted polymer-stabilization70

5.4 Summary75

Chapter 6 Embedding the OLED backlight into an LC cell..... 76

6.1 Introduction.....76

6.2 Design and operational principles of emi-flective LCD78

 6.2.1 Device and fabrication designs78

 6.2.2 Preliminary test of optical performance.....79

6.3 Fabrication process for embedding the OLED into an LC cell	81
6.3.1 Low temperature process for LC alignment	81
6.3.2 Thin film encapsulation for OLED device.....	81
6.3.3 Directly building the LCD on the OLED.....	82
6.4 Results of integrated emi-flective LCD device.....	83
6.4.1 Lifetime of the integrated device	83
6.4.2 Optical contrast of the emi-flective LCD.....	84
6.5 Optimization on the optical contrast in reflective mode.....	85
6.5.1 Principle of contrast ratio enhancement with volumetric scattering layer.....	85
6.5.2 Simulation results.....	86
6.5.3 Experimental results.....	88
6.6 Summary	90
Chapter 7 Conclusion and future work	92
7.1 Conclusions.....	92
7.1.1 Investigating the fast-switching symmetric H state	92
7.1.2 Stabilizing the high-brightness relaxed bend state.....	94
7.1.3 Embedding the OLED backlight into an LCD cell.....	96
7.2 Future works	98
7.2.1 Implementing the RB stabilization into actual LCD fabrication	98
7.2.2 Incorporating symmetric H state with flashing backlight.....	99
7.2.3 Fabricating the thoroughly flexible emi-flective LCD	100
7.2.4 Integration of fast switching OCB-LCD with embedded OLED.....	101

Figure captions

Fig. 1-1 The evolution of information display technology.	1
Fig. 1-2 LC molecular profiles of (a) FLC, (b) Ch-LC, and (c) NLC [1-7].	2
Fig. 1-3 Operational principle of IPS mode.	3
Fig. 1-4 Operational principle of MVA mode.	4
Fig. 1-5 Operational principle of the OCB-LCD [1-7].	5
Fig. 1-6 The schematic diagram of light transmission in the on/off states.	6
Fig. 1-7 The evolution of backlight module.	7
Fig. 2-1 The LC cell strain induced by the (a) splay, (b) twist, and (c) bend motions	12
Fig. 2-2 Different alignment arrangements of upper and lower substrates in (a) TN, (b) ECB, and (c) pi cells.	15
Fig. 2-3 Gibbs's free energy of bend and splay states	16
Fig. 2-4 Phase transition in a pi-cell.	17
Fig. 2-5 Schematic diagram of two equivalent halves of Fréedericksz cell.	18
Fig. 2-6 Backflows in the OCB and TN cells.	18
Fig. 2-7 Comparison of response times in (a) TN and (b) OCB cells [2-4].	18
Fig. 2-8 Optical configuration of a general LCD device [1-7].	19
Fig. 2-9 Schematic diagrams for describing the interaction between the incident light and media.	21
Fig. 2-10 (a) the configuration of Poincare sphere and (b) its corresponding ellipticity.	23
Fig. 2-11 Projection of polarizer and analyzer at (a) normal and (b) oblique directions.	25
Fig. 2-12 The compensation mechanism with wave-plates.	25
Fig. 2-13 (a) The asymmetric contrast degradation and (b) grey-scale inversion phenomenon.	26
Fig. 2-14 The configuration of optical compensation foils.	27
Fig. 2-15 Incomplete dark state under high electrical field in a pi-cell.	28
Fig. 2-16 Compensation mechanism of using wave-plates on the pi-cell.	28
Fig. 3-1 Standard LCD fabrication.	30
Fig. 3-2 Standard OLED fabrication.	31
Fig. 3-3 Display measurement setup of Conoscope.	32
Fig. 3-4 Conventional measurement for R-LCD.	33
Fig. 3-5 Segment recording function.	34
Fig. 3-6 Experimental setup of a spectroscopic ellipsometry.	35
Fig. 3-7 Methodology of using spectroscopic ellipsometry to characterize parameters of an LC cell.	35

Fig. 3-8 Scanning electron microscopy assisted focus ion beam.....	36
Fig. 4-1 Inter-state transition in a pi-cell.....	37
Fig. 4-2 Suppressed bright state after polymer-stabilization.	38
Fig. 4-3 Placing the rubbing direction of the pi-cell parallel to one of the crossed polarizers to examine the occurrence of twist state.	39
Fig. 4-4 Oscilloscopic image of the bend to twist transition. Note that the rubbing direction of the pi-cell is parallel to one of the crossed polarizers.	40
Fig. 4-5 LC texture changing from the bend state to the twist state. Note that the rubbing direction of the pi-cell is parallel to one of the crossed polarizers.	41
Fig. 4-6 Oscilloscopic traces for demonstrating the impulse driving method.	42
Fig. 4-7 Photographs taken while driving the pi-cell with impulse waveform.....	42
Fig. 4-8 Experimental setup of synchronized polymer-stabilization.	43
Fig. 4-9 Scheme of synchronized polymer-stabilization.	44
Fig. 4-10 Oscilloscopic traces of synchronized polymer-stabilization.	45
Fig. 4-11 Method used for verifying the LC profile of relaxed bend state.	45
Fig. 4-12 The LC profiles measured by spectroscopic ellipsometry at (a) lowest bend, (b) 5V bend, and (c) 10 V bend states.....	47
Fig. 4-13 Transmission-voltage relations of pi cells.....	48
Fig. 4-14 Comparison between the different pi-cells whose rubbing directions are placed at 45° to the crossed polarizers, where the pi-cells are operated in the (a) on-state and (b) off state.	49
Fig. 4-15 The viewing-angle dependent phase retardation of the pi-cells.	50
Fig. 4-16 Response times of the pi cells. The pi-cells are positioned at 45° to the crossed polarizers.....	51
Fig. 4-17 Proposed optical compensation for the relaxed bend state stabilized pi-cell.	52
Fig. 5-1 Hs state director profile and its response time.	54
Fig. 5-2 Phase transition by continuous driving waveform.	56
Fig. 5-3 The state transition from splay to Hs to Ha state.	57
Fig. 5-4 LC director profiles of splay, Hs, and Ha states in a pi-cell.....	59
Fig. 5-5 The methodology of measuring the LC director profiles of splay, Hs, and Ha states in a pi-cell.....	59
Fig. 5-6 Burst driving waveform for the device and illuminating LED.	60
Fig. 5-7 The director configurations of (a) splay, (b) Ha, and (c) Hs states.	60
Fig. 5-8 Measured conoscopic images of device.....	62
Fig. 5-9 Concept of Hs lifetime extension by polymer stabilization.	63
Fig. 5-10 Structure used for simulating the Hs lifetime extension.	63
Fig. 5-11 Initial stage of simulation setup.....	65

Fig. 5-12 Two cases of Hs state collapsing via (a) twist and (b) Ha state formations.	65
Fig. 5-13 LC director profile after 2000 ms in the best case of Hs state lifetime.	65
Fig. 5-14 Concept of synchronized polymerization.	67
Fig. 5-15 Oscilloscopic image of synchronized signals, where curve 1 represents the optical signal of LC device, curve 2, triggering signal, and curve 3, monitored UV light signal.	67
Fig. 5-16 Oscilloscopic image of the dynamics during the synchronized polymerization on the Hs state.	69
Fig. 5-17 Oscilloscopic image of phase-suppressed pi-cell.	69
Fig. 5-18 The optical setup of polymerization with a photo-mask.	71
Fig. 5-19 Optical microscopic images of polymerized pi-cell with photomask.	72
Fig. 5-20 The microscopic images of four different flow conditions.	73
Fig. 5-21 The microscopic images of the pi-cells. The polymer walls are against the flow during the polymerization (sample 4).	74
Fig. 5-22 The microscopic images of the pi-cells whose polymer walls are along the flow during the polymerization (sample 3).	74
Fig. 6-1 The configurations of (a) conventional transflective and (b) stacked OLED/LCD displays.	77
Fig. 6-2 OLED devices with (a) high and (b) low resolutions.	77
Fig. 6-3 (a) Configuration and (b) driving circuit of emi-flective LCD.	79
Fig. 6-4 Proposed stacking structure of OLED/LCD.	79
Fig. 6-5 Iso-contrast contours of two emi-flective LCD configurations.	80
Fig. 6-6 Schematic diagram of TFE structure.	82
Fig. 6-7 Fabrication scheme of building LCD on an OLED device.	83
Fig. 6-8 (a) The SEM image of TFE and (b) the lifetime of OLED after integration.	84
Fig. 6-9 Photographs of the functioning of integrated OLED and R-LCD.	84
Fig. 6-10 Conoscopic images of the integrated device in OLED and R-LCD modes.	85
Fig. 6-11 Operational principle in (a) emissive and (b) reflective modes.	86
Fig. 6-12 Mechanism of light-out-coupling enhancement by VSL.	86
Fig. 6-13 Three conditions for comparing the haze component.	87
Fig. 6-14 Simulated haze component in Lambertian, mirror, and the VSL cases.	88
Fig. 6-15 SEM images of VSL at the surface and cross-section.	88
Fig. 6-16 Photograph of LCD with and without adopting VSL.	89
Fig. 6-17 The transmission mode of adopting sparse and dense type VSLs.	90
Fig. 7-1 The research topics explored and concluded in this thesis.	92
Fig. 7-2 Stroboscopic conoscopy is the first method verifying the transient profile of Hs state.	93
Fig. 7-3 The polymer wall structure designed for extending the Hs lifetime has been	

simulated and fabricated.	94
Fig. 7-4 The high-brightness relaxed bend state has been stabilized by our proposed synchronized polymerization.	95
Fig. 7-5 The OLED and LCD have been successfully integrated.....	96
Fig. 7-6 The VSL demonstration in the transmissive and reflective modes.	97
Fig. 7-7 The implementation of RB stabilization into actual LCD processes.	99
Fig. 7-8 Utilizing the flashing backlight technique along with the burst driving method to realize the application of the Hs state pi-cell.	100
Fig. 7-9 The proposed structure of entirely flexible emi-flective LCD.	101
Fig. 7-10 The proposed device structure adopting all of the results obtained in this thesis.	102



List of tables

Table 1-1 Comparison of LC modes.	8
Table 2-1 The Stokes parameters and their physical definitions.....	23
Table 5-1 Simulation results of Hs state lifetime extension with polymer wall.	66
Table 5-2 Summary of conditions and results of tested pi-cell.....	68
Table 5-3 The different flow conditions of the pi-cell.	72
Table 6-1 The transmission mode without and with different cases of VSL.....	90
Table 7-1 Comparison of different pi-cells.	96
Table 7-2 Comparison of proposed OLED/LCD device structures.	98



Chapter 1

Introduction

1.1 The evolution of information display technology

Flat panel display (FPD) technologies have revolutionized the whole display industry during the past 10 years owing to its outstanding feature of slim form factor. This feature not only makes the FPD as a part of the house decoration but also makes the personal mobile gadgets to be prevailing. The old-fashioned cathode ray tube (CRT) display is overwhelmed by the FPD technologies which include plasma display panel (PDP) [1], field emission display (FED) [2], organic light emitting diode (OLED) [3,4], and liquid crystal display (LCD) [5, 6], as summarized in Fig. 1-1. Among these FPD technologies, nematic LCD is the most popular one because of its high fabrication yield and adaptability to any panel sizes. On the other hand, OLED is regarded as a promising display technology because of its advantages of slim-form-factor, high energy efficiency, and good image quality. However, owing to its low fabrication yield, it is not prevailing in the commercial display products at present. In this thesis, most effort will be devoted on the nematic LCD and OLED to explore the ultimate features of a future display device.

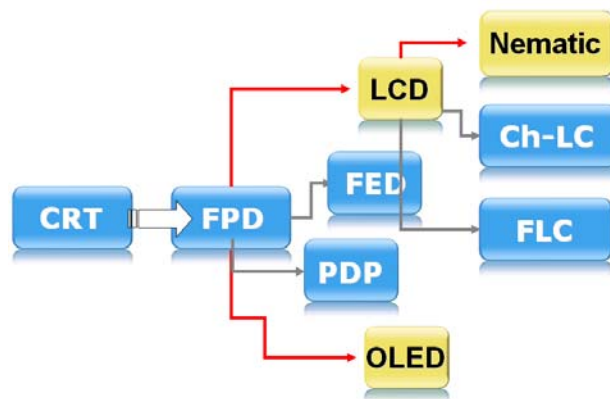


Fig. 1-1 The evolution of information display technology.

1.2 Nematic liquid crystal display technologies

Three LC materials attract most attention in the LCD research area; they are ferroelectric LC (FLC) [7], cholesteric LC (Ch-LC) [7], and nematic LC (NLC). Their molecular profiles are shown in Fig. 1-2. The ferroelectric one has very short response time (on the μs scale); however, due to its high viscosity and difficulty for adopting into current mass production, we are not going to discuss it in this thesis. The Ch-LC has bi-stability and flexibility [8-10]. Because it can be made without alignment, adopting it into the LCD fabrication can avoid the high temperature alignment process. In addition, owing to its selective reflectivity, it is also used to be a reflective color filter. However, because of its low contrast and not applicable for the transmissive mode LCDs, it is not as popular as nematic LCs nowadays. Considering the nematic LCs, its easy fabrication process makes it dominating the LCD area for the time being. Consequently, many techniques were proposed to further improve the nematic LCD devices on the features of switching speed, contrast ratio, and form factor.

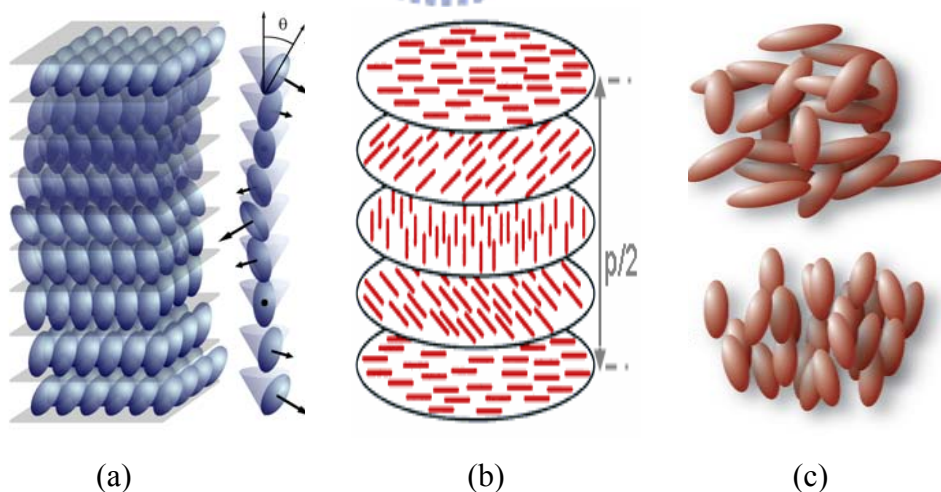


Fig. 1-2 LC molecular profiles of (a) FLC, (b) Ch-LC, and (c) NLC [1-7].

1.2.1 Fast-switching LC modes

Three kinds of LCD modes are currently in the mainstream of the LCD industry.

They are multi-domain vertically aligned (MVA) [11], in-plane switching (IPS) [12], and optically compensated bend (OCB) [13] mode LCs. They are interesting to the LCD companies and researchers is due to their distinguished feature of “wide viewing angle.” This feature is an important requirement for LCD-TV applications. Therefore, these three wide-viewing LC modes are selected to develop for further requirement of fast-switching. Here, we will introduce these three LC modes to understand their advantages and issues.

1.2.1.1 In-plane switching mode

Conventional IPS mode uses homogeneously aligned LC materials driven by lateral field. As shown in Fig. 1-3 [7], the field adjacent to the substrate is not uniform, resulting in fringing effect that causes the degradation of image quality. In spite of this degradation, the IPS still has very good wide-viewing performance, since the LC director deformation is isotropically in-plane.

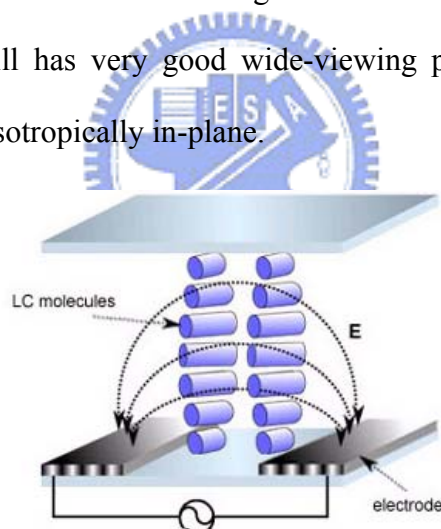


Fig. 1-3 Operational principle of IPS mode.

1.2.1.2 Multi-domain vertically aligned mode

Conventional VA mode uses homeotropically aligned LC materials, and all LC directors align in the same direction. This LC configuration makes the viewing property significantly varied at off-axis direction. To resolve this issue, as shown in Fig. 1-4 [7], protrusions were introduced to vary the orientation of LC directors in

multi-direction. This structure makes the phase retardation symmetric to certain directions.

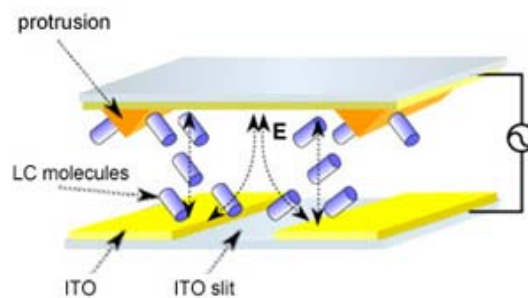
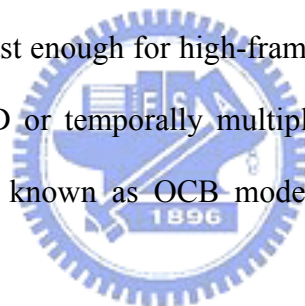


Fig. 1-4 Operational principle of MVA mode.

1.2.1.3 Optically compensated bend mode

Though IPS and MVA modes have very outstanding wide-viewing characteristic, their response times are not fast enough for high-frame-rate display applications, such as field sequential color LCD or temporally multiplexing 3D display. Therefore, a novel technique, pi-cell also known as OCB mode, was proposed to fulfill these requirements.



Though OCB-LCD is regarded as the fastest switching LCD mode among the nematic LCDs, it still has some issues to be resolved. Among them, the most critical issue is the recovery from the bend state back to the splay or twist states. As shown in **Fig. 1-5**, the OCB cell is normally operated in the bend state; however, because of the topological difference between the ground splay state and the bend state, a nucleation transition has to be completed before operation. This transition can be initiated by applying a critical voltage (V_{cr}), and then this voltage is held to sustain the device in the bend state. However, the pi cell still has the tendency of recovering into the splay state. Therefore, in this thesis, we will propose two methods to prevent this issue. One is to use the symmetric H (Hs) state whose LC profile is continuous to the ground splay state, thus no priming is required [14]. The other is to use a polymerization

technique which can simultaneously sustain the bend state and increase the brightness.

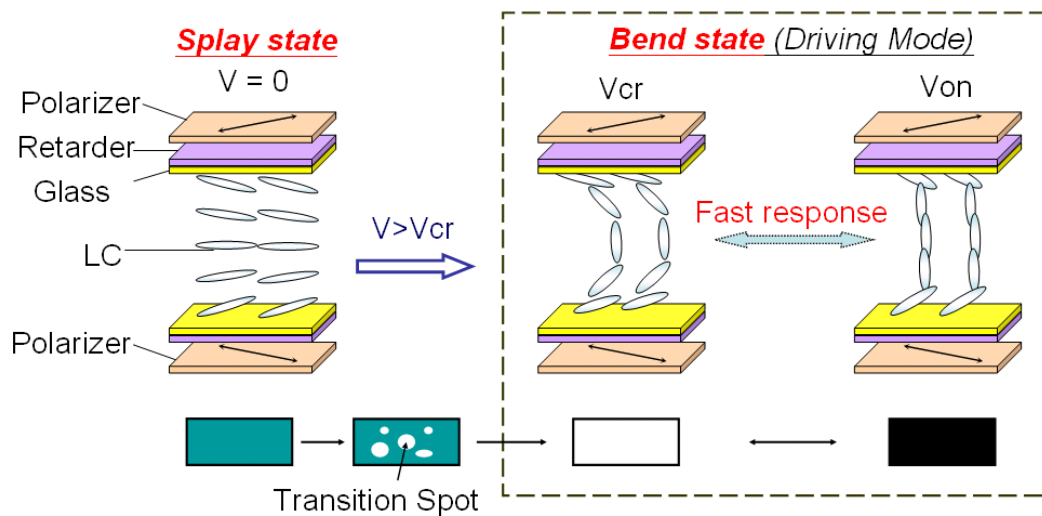


Fig. 1-5 Operational principle of the OCB-LCD [1-7].

1.2.2 High-contrast-ratio LCD technologies

To exhibit a vivid image, high-contrast-ratio is a very crucial feature in a display. In the conventional LCD system, as shown in Fig. 1-6 (a), the backlight is kept in the status of “turned-on” during the operation. The grey scale of image is rendered by tuning the transmittance of the LCD device, which means the light irradiated from the backlight is likely to be leaked even the LCD device is in the off-state. This operational mechanism results in incompleting dark state and waste of power.

To increase the contrast ratio, there were three major techniques proposed. One was to stack more LCD devices to cut off more light intensity in the off-state [15]. Another was to increase the brightness of on-state or decrease the light leakage of the off-state in an LCD device [16]. The other was to use the regionally flashing backlight to make the dark state complete [17]. These proposed techniques are summarized in Figs. 1-6 (b), (c), and (d), respectively.

Considering the technique of using dual-LCD-panel, since the LC device is regarded as an “intensity modulator,” stacking two or more LCD panels results in

more effectiveness of intensity filtering. Adopting this technique, the LCD system is able to achieve the contrast ratio of $10^6:1$. However, this kind of technique is not very competitive in the cost. As for the technique shown in Fig. 1-6 (c), incorporating one or more birefringent films in the LC cell is able to decrease the light leakage in the off-state. This technique was successfully used in Prof. T. Uchida's optical design on the pi-cell. In his design, the birefringent films were used for compensating the residual phase retardation in the off-state to yield a complete dark-state. However, a more elegant way of cutting off the light leakage in the off-state is to turn off the backlight directly, as shown in Fig. 1-6 (d). This method not only increases the contrast ratio but also decreases the power consumption of an LCD system. In this thesis, the latter two techniques will be adopted in our proposed devices.

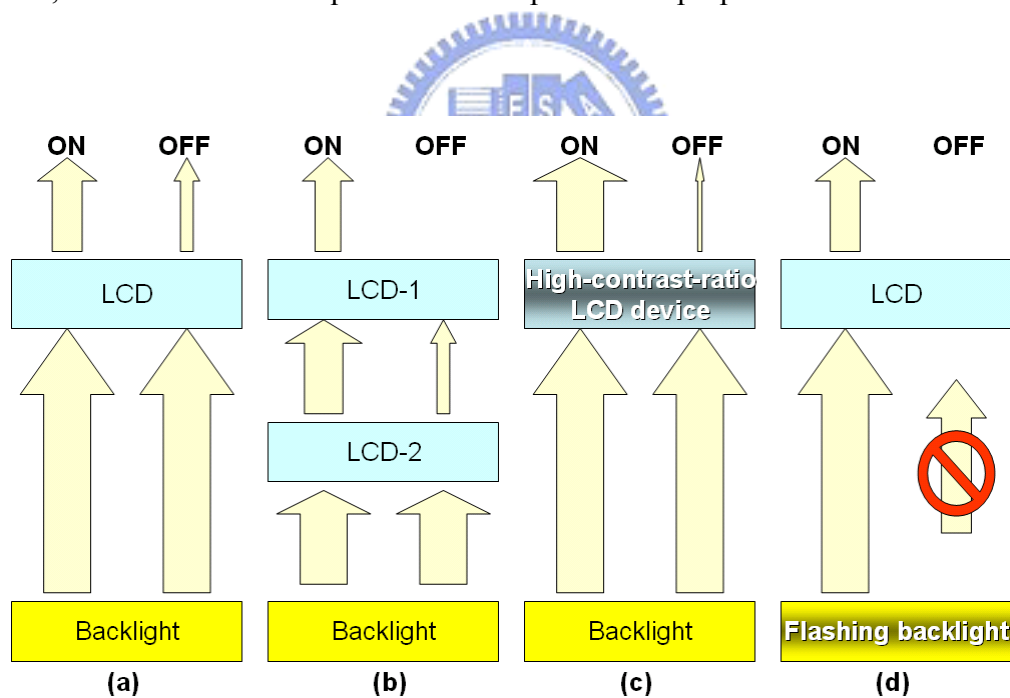


Fig. 1-6 The schematic diagram of light transmission in the on/off states. (a) is the conventional LCD system. (b)~(d) is the newly-proposed LCD technologies, where (b) utilizes dual-LCD-panel technique to decrease the off-state transmission, (c) emphasizes the design of LCD device to increase the on-state brightness and decrease the off-state light leakage, and (d) exploits a flashing backlight to complete the dark-state.

1.2.3 Slim-form-factor devices for LCD backlight

In mobile display applications, to make an LCD system thinner, the most effective way is to decrease the thickness of backlight, since the backlight occupies the most volume among the components in an LCD. For this reason, the LCD backlight was evolved from the directly-lit type to the side-lit type, and then lately to the slim-LED type. As shown in Fig. 1-7, generally, the direct-lit type backlight is quite bulky, because the optical path for diffusing the emitted light has to be long enough to achieve uniform illumination. To shrink the thickness of backlight, the side-lit type backlight exploits a lateral light guide plate instead of the vertical diffuser plate. Since the optical path is constructed laterally, the thickness can be largely decreased. With proper designs of LED packaging and light guide, the volume of LED backlight can be further reduced without sacrificing the illumination uniformity (as shown in Fig 1-7 (c)). In this thesis, we propose to embed the LED directly into the LCD device for largely decreasing the form factor, as shown in Fig. 1-7 (d).

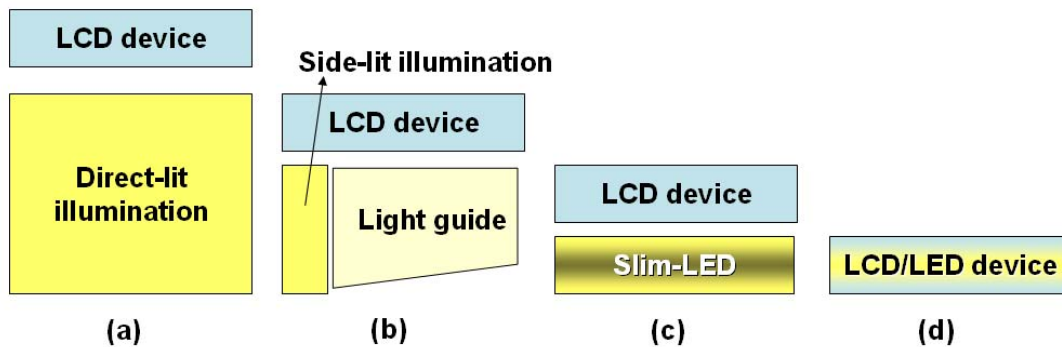


Fig. 1-7 The evolution of backlight module. (a) The direct-lit type, (b) the side-lit type, and (c) the slim-LED type. We further propose to embed the LED backlight into an LCD device as shown in (d).

1.3 Motivation and objectives

As the LCDs overwhelmed the bulky and old-fashioned CRTs, the revolution in display industry has been initiated. To play the important roles as a human/machine

interface or a multi-media player, the criterion of the LCD display has been drastically elevated. While evaluating an LCD, the most important factors to be considered are switching speed, optical contrast, and form factor. Therefore, the major objective of this thesis is to explore the ultimate performances of a future LCD in these three factors.

A comparison among the prevailing LCD technologies is made to assess their advantage and weakness. As summarized in Table 1-1, among the IPS, MVA, and OCB modes, only OCB mode (pi-cell) is able to operate at the response time of less than 3 ms. As a result, this thesis basically focuses on the pi-cell rather than the others.

Table 1-1 Comparison of LC modes.

items	TN	FLC	IPS	MVA	OCB
Response time	X (~20 ms)	⊙ (μ s)	△ (~10 ms)	△ (~10 ms)	○ (less than 3ms)
Contrast	△ (600:1)	X (100:1)	○ (1000:1)	⊙ (1200:1)	△ (800:1)
Viewing angle	X	○	○	⊙	⊙
Fabrication	⊙	X (too viscous)	○	○	⊙
Driving	⊙	X (30 V)	⊙	⊙	△ (splay recovery)

TN: twist nematic ⊙ : Excellent ○ : Good △ : Acceptable X : Poor
 FLC: ferroelectric liquid crystal IPS: in-plane switching
 MVA: multi-domain vertically aligned OCB: optically compensated bend

To investigate the fast-switching pi-cell, we aim to exploit its full range including the symmetric H (Hs) and the relaxed bend (RB) states. The Hs state was reported to have overall response times of 1 millisecond [14]; however, owing to its short lifetime of around 100 ms, it is not suitable for display applications. To increase its lifetime, it

is necessary to know its LC director profile first. Nevertheless, as mentioned above, the lifetime is very short; no direct evidence of its LC director profile has been reported. In this thesis, we will verify its profile first and then propose a method to extend its lifetime.

To increase the pi-cell's optical contrast, we aim to stabilize the RB state which was reported to have the highest brightness among the states in a pi-cell [18, 19]. The difficulty of stabilizing this state is due to its transient existence. Nowadays, people can only use it dynamically. Here, we will use polymer-stabilization to stabilize this non-permanent state. After stabilizing this RB state, not only the high optical contrast can be obtained but also the undesirable recoveries can be avoided.

To largely decrease the form factor, we will examine the possibility of embedding an OLED into an LCD device. The difficulty of embedding an OLED into an LCD is owing to the fragile cathode of OLED, since the cathode is very likely to be damaged by the thermal process of LCD. To overcome this issue, we will use the multi-layer thin-film-encapsulation to protect the OLED section from the possible damage by LCD processing. Because the cathode of OLED is very smooth and highly reflective, the specular effect may be induced. Therefore, we will design a volumetric scattering layer to increase its sunlight visibility.

1.4 Organization of this thesis

This thesis is organized as follows: in **chapter 2**, basic principles and theories used in this thesis will be introduced. The principles of mechanical design on the LC cells including the continuum theory and anchoring effect are described, and the principles of optical design on the LC cell including the extended Jones matrix and optical compensation methodologies are also presented. In **chapter 3**, the device fabrication and measurement will be reported. In **chapter 4**, a polymerization

technique for preventing the OCB cell from the undesirable recoveries is proposed, where the merit of this method is that the optical contrast will not be suppressed after the stabilization. In **chapter 5**, the Hs state in a pi-cell is investigated in depth. We verify the transient profile of LC director with the newly proposed synchronized illumination method. According to the measured profile, a method for extending the lifetime of Hs state is proposed and simulated. In **chapter 6**, the realization of embedding an OLED device directly into an LCD cell is demonstrated. Additionally, a volumetric scattering layer is introduced to further increase its sunlight visibility. Finally, the conclusions and future works are presented in **chapter 7**.



Chapter 2

Theory and Principle

The mechanical and optical designs of an LCD are introduced in this chapter. In the principle of mechanical design, the continuum theory is used to calculate the Gibbs's energy of a certain state, and Rapini-Papoular approach is used to calculate the alignment effect on the orientation of LC director. In the principle of optical design, the extended Jones matrix method is used to calculate the polarization state transformation between the birefringent media, and Poincare sphere is used to visualize the optical compensation mechanism.

2.1 Principle of mechanical design on LC cells

The switching performance of an LC device relies on its mechanical design. To design the response time, flow direction, and equilibrium LC profile, continuum theory is well-used by the LCD researchers. A basic continuum theory considers the elastic relaxation of the LC molecules. Taking more factors into consideration, such as the electric field, the magnetic field, and the anchoring effect makes the equation more appropriate to the actual LCD cases. The detailed description of continuum theory is explained as follows.

2.1.1 Continuum theory

Frank-Oseen continuum theory is well-used in calculating the equilibrium profile of LC directors in a cell [20-22]. This theory can be explained by equation (2-1), where \mathbf{n} is the vector of the LC director, q_0 is $2\pi/p$ (p : Pitch of liquid crystal helix), and K_{11} , K_{22} , and K_{33} are the elastic constants of splay, twist, and bend motions, respectively (as depicted in Fig. 2-1). These motions and the external electric field (E)

induce strain energy to the system, and thus the free energy of the system changes.

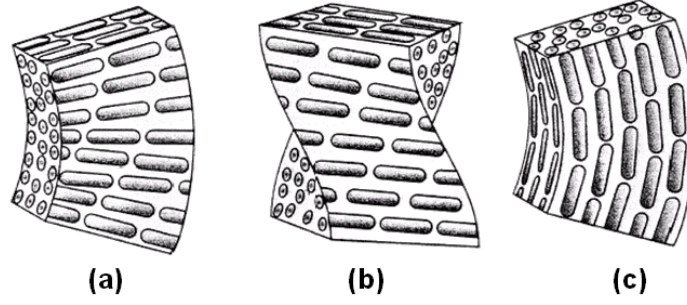


Fig. 2-1 The LC cell strains induced by the (a) splay, (b) twist, and (c) bend motions [23].

$$F = \frac{1}{2} \left\{ K_{11} (\nabla \cdot \mathbf{n})^2 + K_{22} [\mathbf{n} \cdot (\nabla \times \mathbf{n}) - q_0]^2 + K_{33} [\mathbf{n} \times (\nabla \times \mathbf{n})]^2 \right\} - \frac{1}{2} (\mathbf{D} \cdot \mathbf{E}) \quad (2-1)$$

By postulating $\hat{\mathbf{n}} = \begin{bmatrix} n_x \\ n_y \\ n_z \end{bmatrix}$ and using the large pixel assumption, i.e. $\frac{\partial F}{\partial x} = \frac{\partial F}{\partial y} = 0$,

where F is an arbitrary function.

The elastic energy can be expressed as:

$$E_e = \frac{1}{2} \left\{ K_{11} (\dot{n}_z)^2 + K_{22} [q^2 + (n_y \dot{n}_x + n_x \dot{n}_y)^2 - 2q(n_y \dot{n}_x - n_x \dot{n}_y)] + K_{33} [n_z^2 (\dot{n}_x^2 + \dot{n}_y^2) + (n_x \dot{n}_x - n_y \dot{n}_y)^2] \right\} \quad (2-2)$$

Furthermore, the electro-static energy can be considered as follows:

$$E_s = -\frac{1}{2} \bar{\mathbf{D}} \cdot \bar{\mathbf{E}} = -\frac{1}{2} \epsilon_0 \epsilon_{zz} E_z^2 \quad : \text{out-of-plane field} \quad (2-3)$$

$$= -\frac{1}{2} \epsilon_0 \epsilon_{xx} E_x^2 \quad : \text{in-plane field} \quad (2-4)$$

$$\text{Relative permittivity tensor: } \bar{\epsilon} = \begin{bmatrix} \epsilon_{//} & 0 & 0 \\ 0 & \epsilon_{\perp} & 0 \\ 0 & 0 & \epsilon_{\perp} \end{bmatrix} \quad (2-5)$$

where $\epsilon_{//}$ and ϵ_{\perp} denote the permittivities along and perpendicular to the long axis

of the LC director, respectively.

Since the LC directors are positioned randomly at (θ, φ) angles, the reference axis has to be rotated about the y axis by θ and about the z axis by φ .

$$R = \begin{bmatrix} \cos \varphi & \sin \varphi & 0 \\ -\sin \varphi & \cos \varphi & 0 \\ 0 & 0 & 1 \end{bmatrix} \begin{bmatrix} \cos \theta & 0 & -\sin \theta \\ 0 & 1 & 0 \\ \sin \theta & 0 & \cos \theta \end{bmatrix} \quad (2-6)$$

$$\bar{\varepsilon} = R \bullet \bar{\varepsilon}_d \bullet R^T = \begin{bmatrix} \Delta\varepsilon \bullet n_x^2 + \varepsilon_{\perp} & \Delta\varepsilon \bullet n_x n_y & \Delta\varepsilon \bullet n_x n_z \\ \Delta\varepsilon \bullet n_x n_y & \Delta\varepsilon \bullet n_y^2 + \varepsilon_{\perp} & \Delta\varepsilon \bullet n_y n_z \\ \Delta\varepsilon \bullet n_x n_z & \Delta\varepsilon \bullet n_y n_z & \Delta\varepsilon \bullet n_z^2 + \varepsilon_{\perp} \end{bmatrix} \quad (2-7)$$

$$\therefore \text{out-of-plane field: } E_{\text{out}} = -\frac{1}{2} \varepsilon_0 \varepsilon_{zz} E_z^2 = -\frac{1}{2} \varepsilon_0 (\Delta\varepsilon \bullet n_z^2 + \varepsilon_{\perp}) E_z^2 \quad (2-8)$$

$$\therefore \text{in-plane field: } E_{\text{in}} = -\frac{1}{2} \varepsilon_0 \varepsilon_{xx} E_x^2 = -\frac{1}{2} \varepsilon_0 (\Delta\varepsilon \bullet n_x^2 + \varepsilon_{\perp}) E_x^2 \quad (2-9)$$

The external electric field E can be substituted as follows:

$$\begin{aligned} D &= \varepsilon \varepsilon_0 E \Rightarrow E = \frac{D}{\varepsilon \varepsilon_0} \\ \Rightarrow -V &= \int_0^d \frac{D}{\varepsilon \varepsilon_0} dz = D \int_0^d \frac{1}{\varepsilon \varepsilon_0} dz \\ \Rightarrow D &= \frac{-V}{\int_0^d \frac{1}{\varepsilon \varepsilon_0} dz} \\ \Rightarrow E &= \frac{-V}{\varepsilon \varepsilon_0 \int_0^d \frac{1}{\varepsilon \varepsilon_0} dz} \end{aligned} \quad (2-10)$$

Substituting this electric field term into Eq. 2-2 so that the electro-static energy can be obtained.

To solve the continuum equation, the large pixel approximation is conventionally used, where the x and y directional variations are assumed to be very tiny. Therefore, the free energy density “g” can be simplified to be a function of $n_x(z)$, $n_y(z)$, $n_z(z)$,

$$\frac{dn_x}{dz}, \frac{dn_y}{dz}, \frac{dn_z}{dz}$$

Integrating the free energy density throughout the whole volume,

$$\begin{aligned}
\Delta G &= \int_{\text{volume}} \Delta g \cdot \Delta v \\
&= \int_{\text{volume}} \left[\frac{\partial g}{\partial n_i} \cdot \delta n_i + \frac{\partial g}{\partial \left(\frac{dn_i}{dz} \right)} \cdot d \left(\frac{dn_i}{dz} \right) \right] \Delta v \\
&= \int_{\text{volume}} \left[\frac{\partial g}{\partial n_i} \cdot \delta n_i + \frac{\partial (g \delta n_i)}{\partial \left(\frac{dn_i}{dz} \right)} \left(\frac{dn_i}{dz} \right) - \frac{\partial (\delta n_i)}{\partial \left(\frac{dn_i}{dz} \right)} \left(\frac{dg}{dz} \right) \right] \Delta v \\
&= \int_{\text{volume}} \left[\frac{\partial g}{\partial n_i} - \frac{\partial}{\partial \left(\frac{dn_i}{dz} \right)} \left(\frac{dg}{dz} \right) \right] \delta n_i \Delta v + \int_{\text{volume}} \frac{d}{dz} \left[\frac{\partial (g \delta n_i)}{\partial \left(\frac{dn_i}{dz} \right)} \delta n_i \right] \Delta v \\
&\because \int_{\text{volume}} \frac{d}{dz} \left[\frac{\partial (g \delta n_i)}{\partial \left(\frac{dn_i}{dz} \right)} \delta n_i \right] \Delta v = \int_{\text{surface}} \left[\frac{\partial (g \delta n_i)}{\partial \left(\frac{dn_i}{dz} \right)} \delta n_i \right] ds = 0 \quad (\text{Strong anchoring makes}
\end{aligned}$$

no energy change at the surfaces)

$$\therefore \Delta g = \left[\frac{\partial g}{\partial n_i} - \frac{\partial}{\partial \left(\frac{dn_i}{dz} \right)} \left(\frac{dg}{dz} \right) \right] \delta n_i \quad (2-11)$$

Calculating Eq. (2-2) and Eq. (2-10) by energy relaxation method described in Eq. (2-11), the minimum of free energy can be obtained, and the preferred LC director profile can be acquired.

2.1.2 Anchoring effect

The LC alignment affects the equilibrium state, switching property, and director configuration of an LC cell. This alignment is generally achieved by the anchoring effect with a pretreated layer. Most preferably, polyimide is used owing to its low cost, high stability, and easy process. Two major methods are used to pre-treat the alignment material: mechanical rubbing and photo-alignment. The mechanical

rubbing method is executed by a roller covered with woolen texture. By brushing in the same direction, the alignment layer is strained, and this strain aligns the LC director in a certain direction. The other method of pre-treating the alignment material is to use polarized UV light to orient the molecules of alignment layer in a certain direction. This method can be used along with a photomask to make multi-directional alignments in one substrate, but the uniformity is still an issue.

By varying the alignment directions of the upper and lower substrates, the cells can be stabilized in different LC profiles. As shown in Fig. 2-2, the 90°, anti-parallel, and parallel alignments can produce the twist nematic (TN), electrically controlled birefringence (ECB), and pi cells, respectively [23].

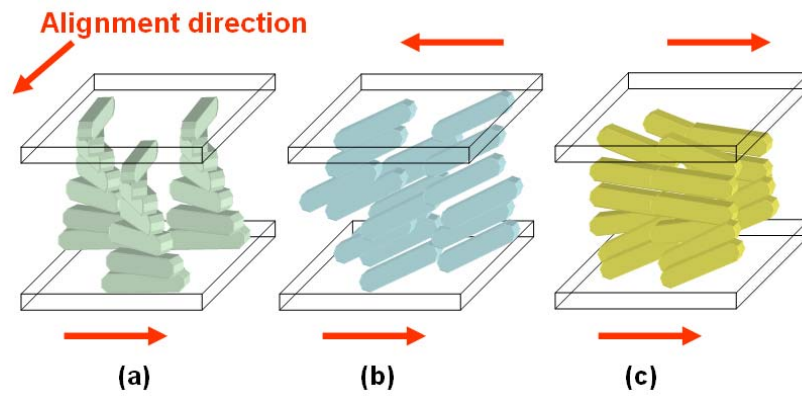


Fig. 2-2 Different alignment arrangements of upper and lower substrates in (a) TN, (b) ECB, and (c) pi cells.

This stabilization mechanism can be expressed by Rapini-Papoular approach [24-26] as follows:

$$F_s = F_\theta + F_\varphi \quad (2-12)$$

$$F_\theta = \frac{1}{2} W_\theta \sin^2(\theta - \theta_0) \quad (2-13)$$

$$F_\varphi = \frac{1}{2} W_\varphi \sin^2(\varphi - \varphi_0) \quad (2-14)$$

where θ and φ denote the polar and azimuthal angles, F_s denotes the total free

energy resulting from the anchoring effect, F_θ denotes the free energy component in terms of the polar angle, F_ϕ denotes the free energy component in terms of the azimuthal angle. W_θ and W_ϕ are the constants whose physical meanings are the interactions between the substrates and the LC directors. θ_o and ϕ_o are the equilibrium angles in the polar and azimuthal dimensions, respectively.

By considering the anchoring effect, the overall continuum equation is then modified as follows. This equation can be used to describe the stabilized LC director profile of an LC cell.

$$F = \frac{1}{2} \left\{ K_{11} (\nabla \cdot \mathbf{n})^2 + K_{22} [\mathbf{n} \cdot (\nabla \times \mathbf{n}) - q_o]^2 + K_{33} [\mathbf{n} \times (\nabla \times \mathbf{n})]^2 \right\} - \frac{1}{2} (\mathbf{D} \cdot \mathbf{E}) + F_s \quad (2-15)$$

2.1.3 Mechanical design of pi-cells

According to the continuum theory mentioned above, the pi-cell can be designed to operate in the specific state. By calculating the Gibbs's free energy in equation 2-15, the stable state corresponding to the applied voltage can be obtained. As shown in Fig. 2-3, without applying a voltage signal, this cell is stabilized in the splay state. While applying a voltage larger than the critical voltage, the bend state becomes more stable than the splay state [27-29].

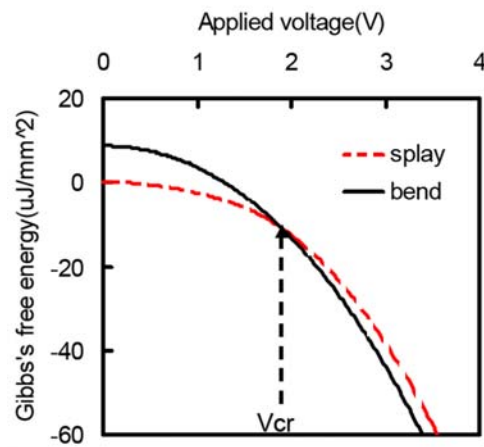


Fig. 2-3 Gibbs's free energy of bend and splay states as a function of applied voltage.

Taking the pretilt into consideration, the Gibbs's free energy diagram can be used to determine whether the bend state is possible to be obtained or not. As shown in Fig. 2-4 (a), if the pretilt is too low, the Gibbs's free energy of bend state is too high, so the bend state can not be stabilized (no matter how much voltage signal is applied). On the other hand, if the pretilt is higher than the critical pretilt (the intersection in Fig. 2-4 (a)), the bend state can be stabilized without an external field. While in the intermediate case, the bend state can be initiated with nucleation by an applied voltage as shown in Fig. 2-4 (b) [35-39].

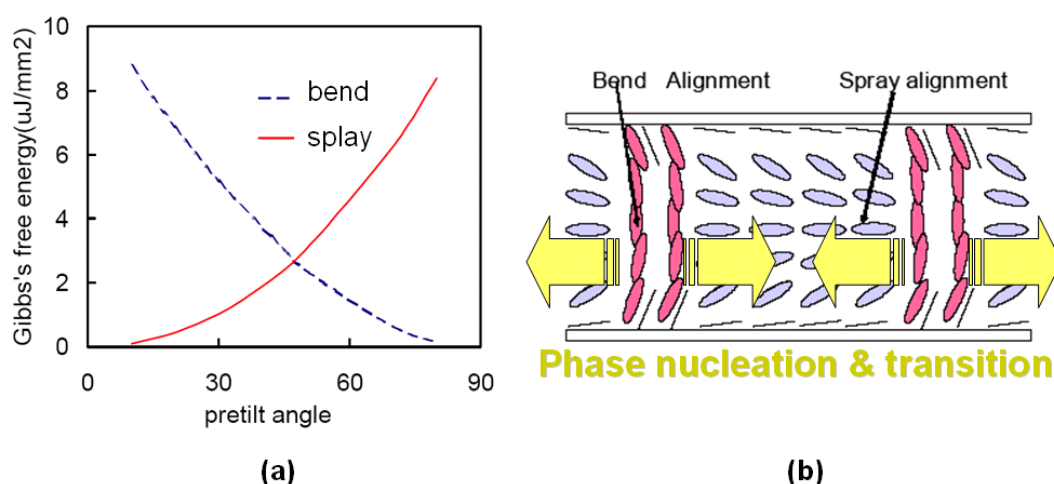


Fig. 2-4 Phase transition in a pi-cell, where (a) is the pretilt effect and (b) is the nucleation mechanism in a phase transition process.

In addition to the operational state, the switching speed is also an important factor related to the mechanical design of an LC cell. The pi-cell is noted for its fast switching due to its symmetric LC director profile and parallel backflow. As shown in Fig. 2-5, the central director of the pi-cell is fixed during the operation. Hence, this cell can be regarded as two halves of Fréedericksz cell. Because the equivalent cell gap is reduced to half, the response time is increased by a factor of 4. Moreover, the parallel backflow in pi-cell makes the relaxation faster, whereas in the case of TN mode, as shown in Fig 2-6, the anti-parallel backflows make the relaxation slower.

Experimentally, the intensity drop while turning off the voltage in the case of TN is slower than that of pi-cell, as shown in Fig. 2-7. Thus, while designing the pi-cell operations, the twist motion or asymmetric flow has to be avoided.

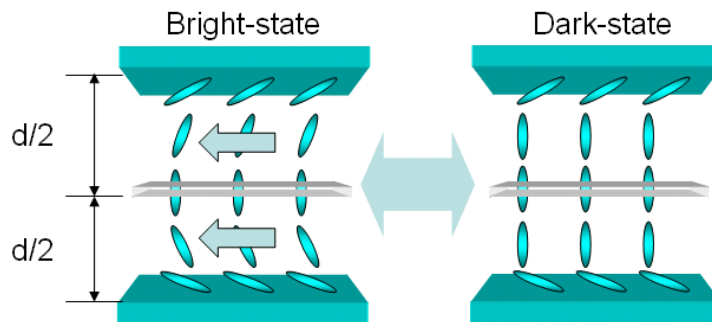


Fig. 2-5 Schematic diagram of two equivalent halves of Fréedericksz cell.

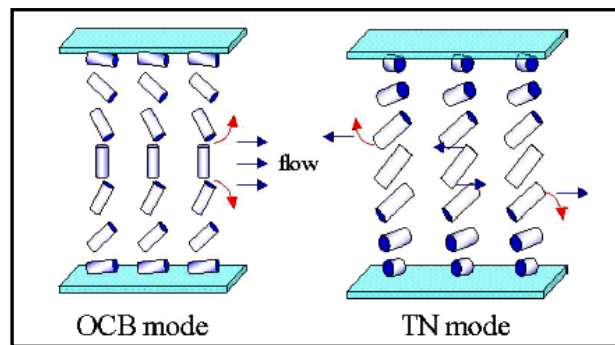


Fig. 2-6 Backflows in the OCB and TN cells.

Anti-parallel relaxation makes response slower!!

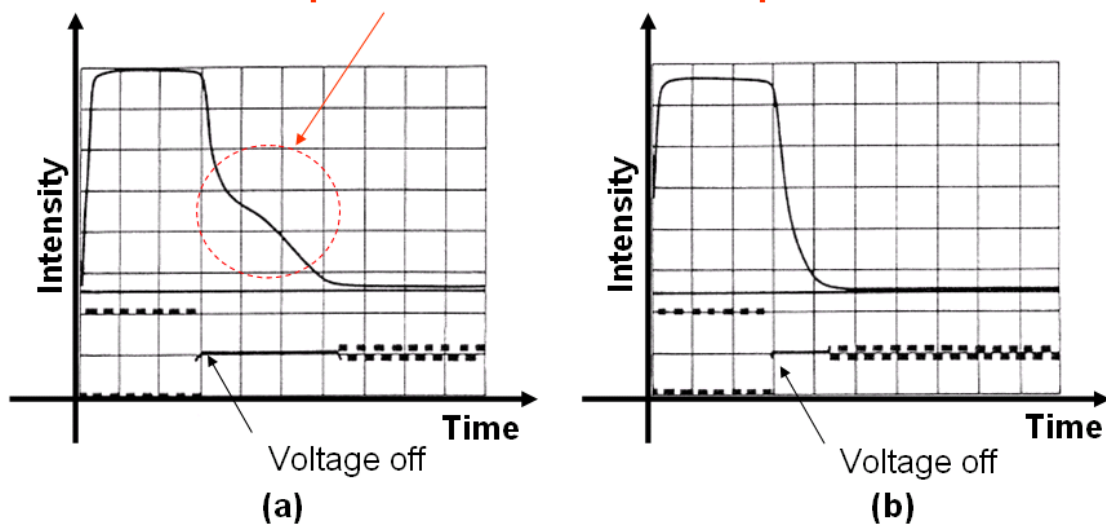


Fig. 2-7 Comparison of response times in (a) TN and (b) OCB cells [23].

2.2 Principle of optical design on LC cells

In the optical design of an LCD device, the most important factors to be considered are: contrast ratio, viewing angle, brightness, and color accuracy. In this section, we will discuss the principles for optimizing these factors.

2.2.1 Operational principle of an LCD device

The general LCD device includes an LC cell, a pair of crossed polarizers, a color filter, and possibly some phase retarders. As shown in Fig. 2-8, the light impinges on the first polarizer (to purify the state of incident light to be linearly polarized), passes through the LC cell (to alter its polarization state), and then be attenuated by the second polarizer to exhibit the grey scale. After that, the light will be filtered by a color filter to show the specific color. A further phase retarder can be adopted in the position before the light passing through the second polarizer to optimize the viewing angle and contrast ratio performances of the LC cell.

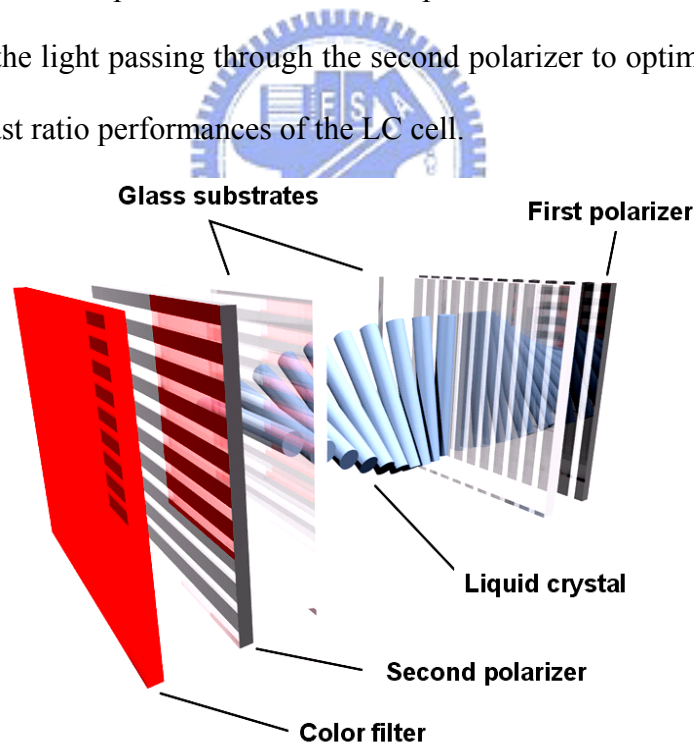


Fig. 2-8 Optical configuration of a general LCD device [7].

2.2.2 Extended Jones matrix for light field distribution calculation

The gray scale is shown by modulating the intensity of incident light passing

through the LCD device. To accurately control the gray scale for rendering the high quality images, the changes of polarization state between the components in the LCD device have to be precisely designed. The principle of this intensity modulation can be expressed by Jones matrix, which was first derived by Jones in 1941 and widely used to study the transmission characteristic of an optical system consisting of birefringent materials. This method; however, is limited to the case of normal incidence. To generalize the case from the normal incidence to the oblique incidence, Prof. P. Yeh introduced an extended Jones matrix method in 1982, which can be used to calculate the transmission of off-axis light in a birefringent network [30,31]. The method is described as follows: referring to Fig. 2-9, the relations between the electric field of incident, reflected, and refracted lights can be written as:

$$\text{Incident: } E = (A_s S + A_p P) \exp[i(\omega t - k \cdot r)], \quad (2-16)$$

$$\text{Reflected: } E = (B_s S + B_p P) \exp[i(\omega t - k \cdot r)], \quad (2-17)$$

$$\text{Refracted: } E = (C_o e^{-ikr} + C_e e^{-ikr}) \exp(i\omega t), \quad (2-18)$$

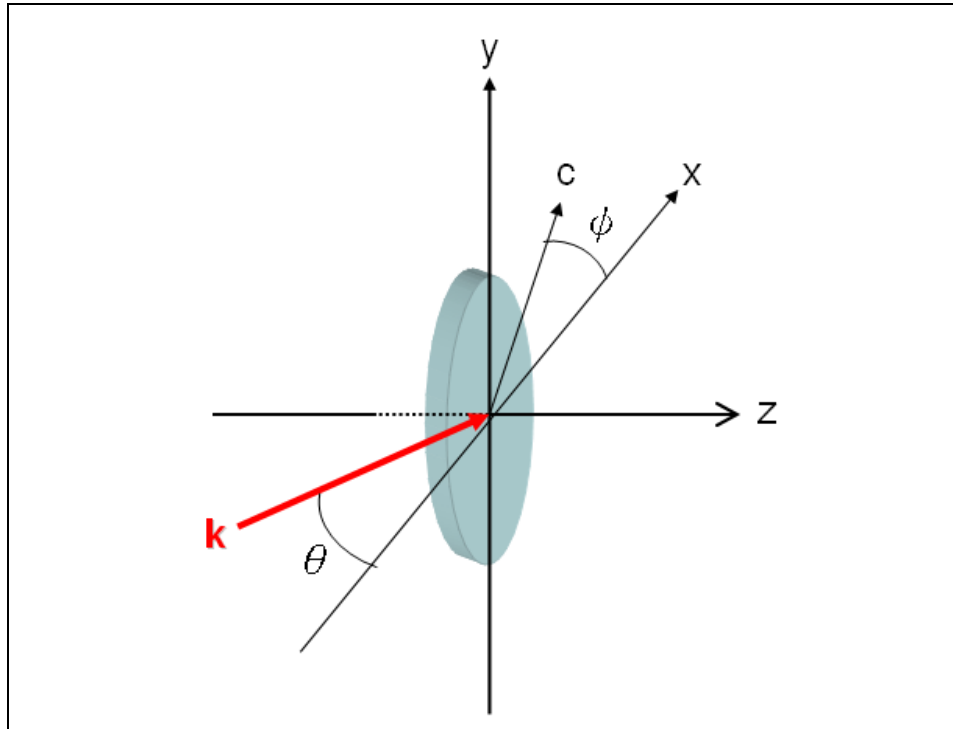
where the suffixes “e” and “o” denote the extra-ordinary and ordinary ray, respectively. In addition, the suffix “s” is a unit vector parallel to the incident plane (plane y-z) and “p” is a unit vector perpendicular to the incident plane. Hence, the relations between p and s, o and e can be written as

$$p = \frac{k \times s}{|k|}, \quad (2-19)$$

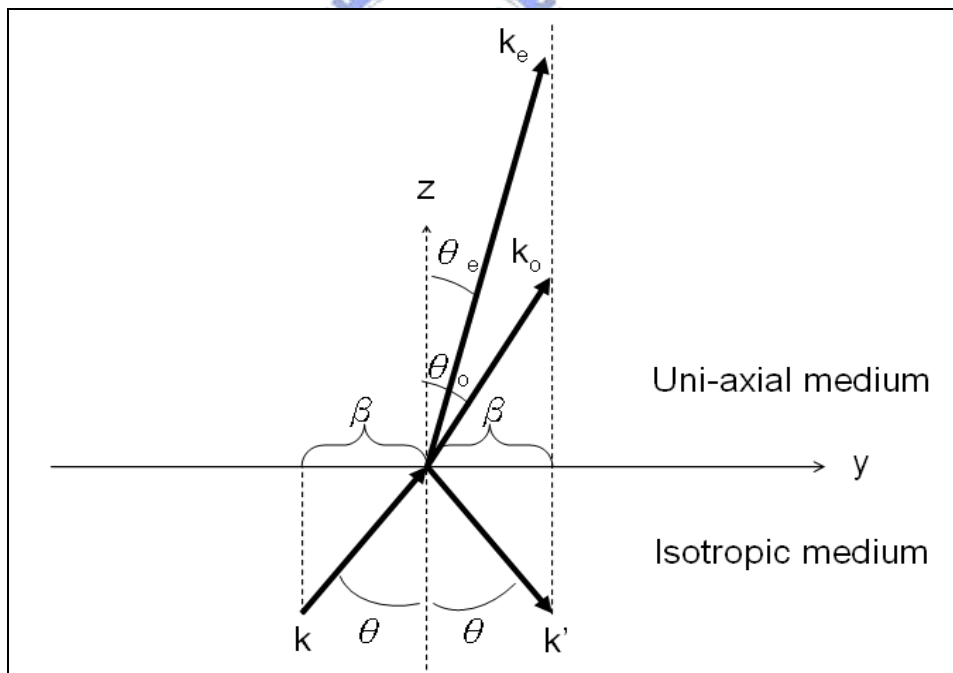
$$p' = \frac{-k' \times s}{|k'|}, \quad (2-20)$$

$$o = -x \sin \varphi + y \cos \varphi, \quad (2-21)$$

$$e = x \cos \varphi + y \sin \varphi, \quad (2-22)$$



(a)



(b)

Fig. 2-9 Schematic diagrams for describing the interaction between the incident light and media. (a) the incident wave-vector k lies on the yz plane and the c axis of the birefringent medium lies on the xy plane; (b) reflection and refraction at the interface between the uni-axial and iso-tropic mediums.

Because the tangential components of electric and magnetic fields must be continuous at the boundary, we can thus obtain four equations. By using several mathematical operations, the transmission coefficients of t_{so} , t_{po} , t_{se} , and t_{pe} can be obtained. Moreover, the expression of Jones matrix describing a light passing through a uniaxial plate can be further simplified as

$$\begin{pmatrix} A'_s \\ A'_p \end{pmatrix} = \begin{pmatrix} t_{es} & t_{os} \\ t_{ep} & t_{op} \end{pmatrix} \begin{pmatrix} e^{-ik_{ez}d} & 0 \\ 0 & e^{-ik_{oz}d} \end{pmatrix} \begin{pmatrix} t_{se} & t_{pe} \\ t_{so} & t_{po} \end{pmatrix} \begin{pmatrix} A_s \\ A_p \end{pmatrix} \quad (2-23)$$

This is the general form of extended Jones matrix used for calculating the transmission characteristic of uniaxial medium such as liquid crystal layers, polarizers, or compensation films. With this calculation, the contrast ratio, viewing angle, and color accuracy can be optimized.

2.2.3 Principles of optical compensation

Most optical design for an LCD device assumes that the observer is in the normal direction. However, this assumption makes the images distorted in the oblique observing angle. To resolve this issue, there are two kinds of optical compensation: one is to compensate the oblique deviation of polarizers; the other is to compensate the inaccurate phase retardation of LC director.

Before discussing the optical compensation methods, it is necessary to introduce the Stokes parameter and Poincare sphere first, since they are very elegant methods for describing the concept of optical compensation.

The Stokes parameters were defined by G. G. Stokes in 1852, which have been used for defining the polarization states of electro-magnetic wave. Generally, the electro-magnetic wave can be described as $E = A(t) \exp[i(\omega t - kr)]$. In this case, the polarization states can be further defined by four parameters listed below:

Table 2-1 The Stokes parameters and their physical definitions.

	Mathematical expression	Physical meaning
S_0	$S_0 = E_x ^2 + E_y ^2$	Light intensity
S_1	$S_1 = E_x ^2 - E_y ^2$	0° or 180° linearly polarized component
S_2	$S_2 = 2 E_x E_y \cos\delta$	$\pm 45^\circ$ linearly polarized component
S_3	$S_3 = 2 E_x E_y \sin\delta$	Circularly polarized component

To visualize the polarization conversion, Poincare sphere was introduced. As shown in Fig. 2-10 (a) [30], the equator represents the linear polarization states, where the polarization state of axis S_1 is orthogonal to that of $-S_1$. In addition, the axis S_3 denotes a circularly polarized state, and the meridians represent the ellipsoidal polarization states. Each polarization state on Poincare sphere can be described by two factors (ε, θ) , where ε is the ellipticity defined as $\tan\left(\frac{b}{a}\right)$, as shown in Fig. 2-10 (b), and θ is the rotation angle between the long axis of the ellipse and the x axis. As a result, the Stokes parameters have correlations between the (ε, θ) as follows:

$$S_1 = \cos(2\varepsilon)\cos(2\theta), \quad S_2 = \cos(2\varepsilon)\sin(2\theta), \quad S_3 = \sin(2\varepsilon)$$

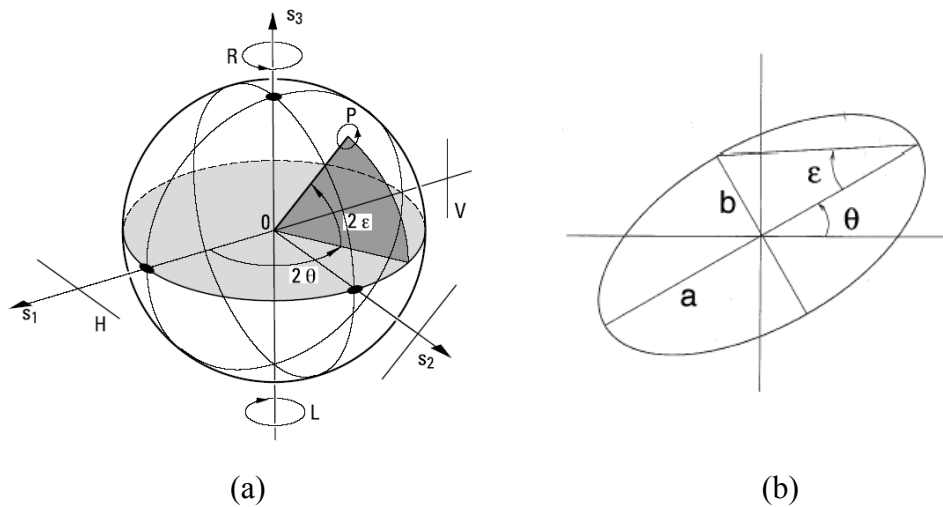


Fig. 2-10 (a) the configuration of Poincare sphere and (b) its corresponding ellipticity.

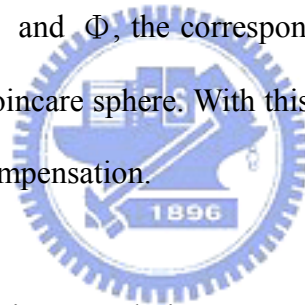
In the case of polarized light passing through a wave-plate, there are two factors shall be considered: one is the relative phase retardation Γ (which is correlated to the relative angle between the incident ray and the optical axis of the wave-plate); the other is the absolute phase retardation Φ (which is correlated to the birefringence and the thickness of the wave-plate)

$$\Gamma = \frac{2\pi}{\lambda}(n_s - n_f)d$$

$$\Phi = \frac{1}{2}(n_s + n_f)\frac{2\pi}{\pi}d$$

Where λ denotes the wavelength of the incident ray, d denotes the thickness of the wave-plate, and n_s and n_f denote the refractive indexes of the slow and fast axes, respectively.

With the calculation of Γ and Φ , the corresponding polarization state variation can be also obtained on the Poincare sphere. With this calculated result, we can easily visualize the outcome after compensation.



2.2.3.1 Optical compensation on polarizer

The crossed polarizers can accurately control the light intensity passing through the LC cell when they are exactly orthogonal to each other (i.e. the polarization states of the incident and exit rays are on the opposite sides of Poincare sphere). As shown in **Fig. 2-11 (a)**, in the ideal case, as the first and second polarizers are perfectly orthogonal to each other, the first polarizer is used for refining the polarization state of the incident light, and the analyzer is used to block certain amount of the light to exhibit the specific gray scale of the image. However, as shown in **Fig. 2.11 (b)**, as the observation is at the oblique direction, the crossed polarizers are not exactly orthogonal in this case. This deviation makes the dark state incomplete.

To resolve this issue, a stacking of A- and C- plates was proposed **[32-36]**. This

method can be explained by Fig. 2-12. When the deviation occurs as shown in Fig. 2-12 (a), the polarization state of P_1 is not orthogonal to A_1 ; therefore, it is needed to transfer the polarization state of P_1 to E . One of the methods proposed by P. J. Bos was to use an A-plate and a C-plate to rotate the polarization state, as shown in Fig. 2-12 (b). Note that using bi-axial film is also capable of having the same effect.

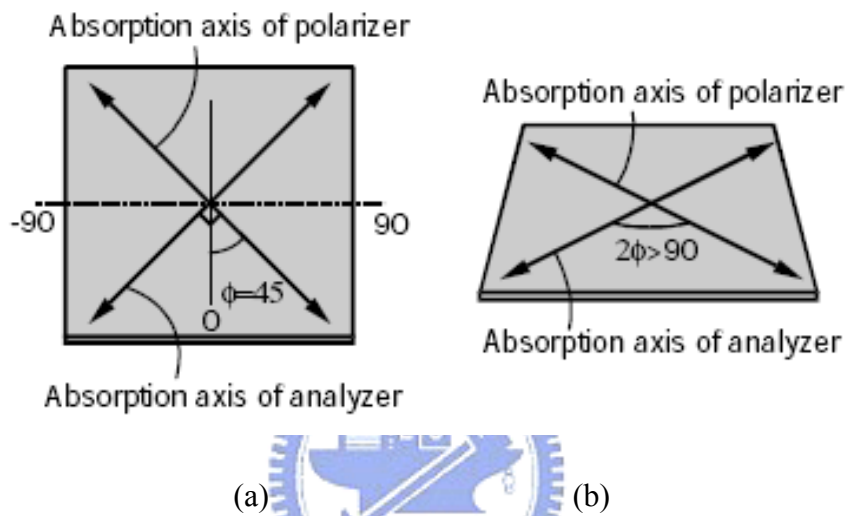


Fig. 2-11 Projection of polarizer and analyzer at (a) normal and (b) oblique directions.

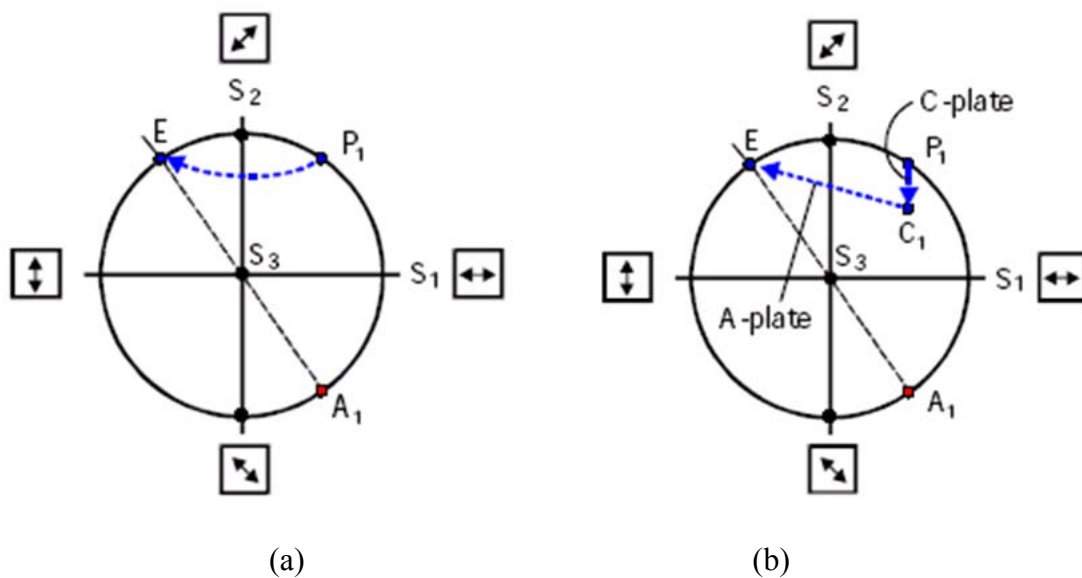


Fig. 2-12 The compensation mechanism with wave-plates. (a) the deviation of crossed polarizers and (b) the mechanism of compensation using A- and C-plates.

2.2.3.2 Optical compensation on liquid crystal

Owing to the viewing angle dependence of phase retardation, the effective phase retardation differs in different viewing directions; therefore, the optical compensation on the LC director is indispensable for achieving high image quality. There are some issues mainly affecting the degradation of the optical contrast apart from the normal observing direction [37]. As shown in Fig. 2-13 (a), the asymmetric orientation of the LC director makes the phase retardations observed from right and left directions different. In addition, the projected phase retardation at small viewing angle is different from that at large viewing angle. This difference results in the grey scale inversion (Fig. 2-13 (b)). These issues can be resolved by a combination of wave-plates. As shown in Fig. 2-14, the compensation films made of hybrid-aligned wave-plate makes the effective phase retardation to be zero at any viewing direction.

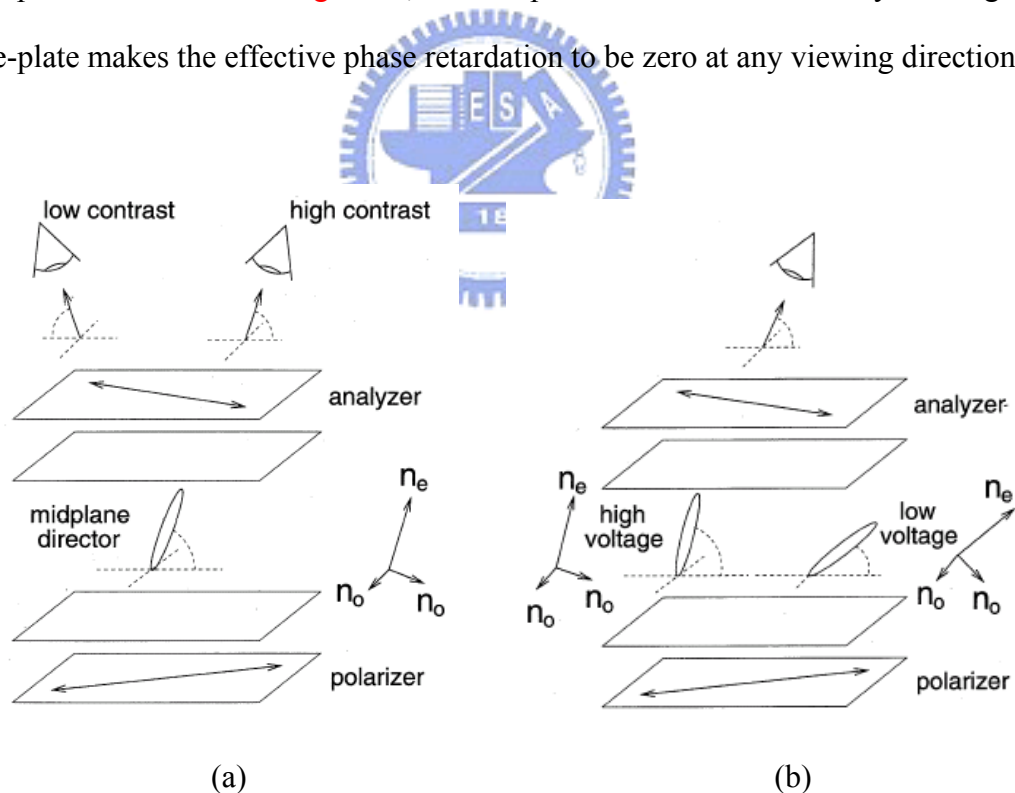


Fig. 2-13 (a) The asymmetric contrast degradation and (b) grey-scale inversion phenomenon [29].

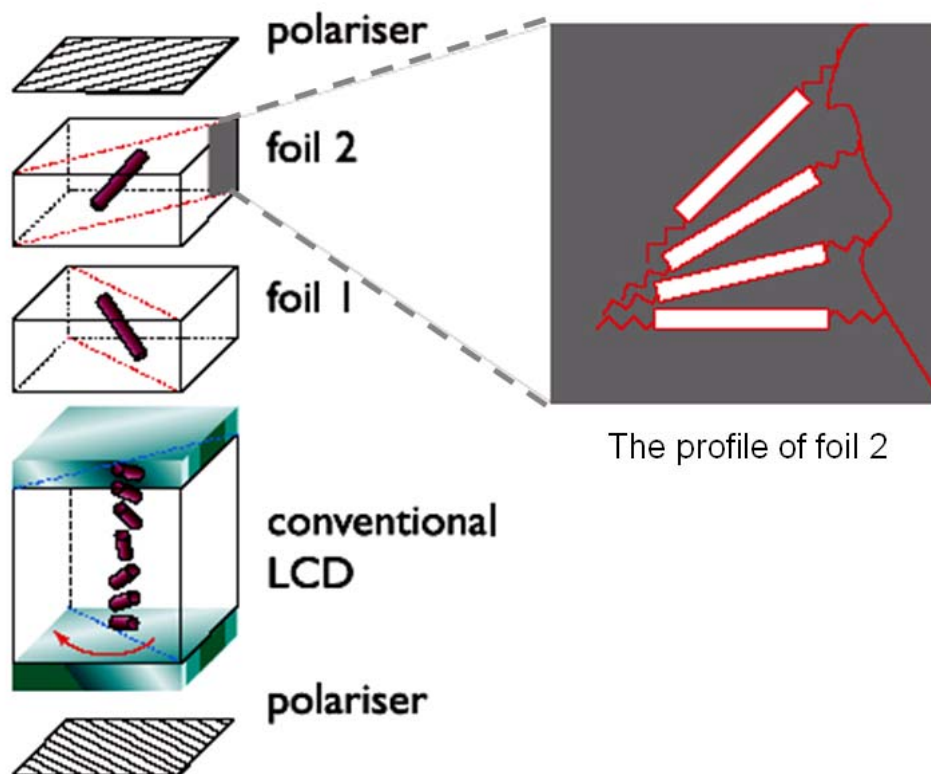
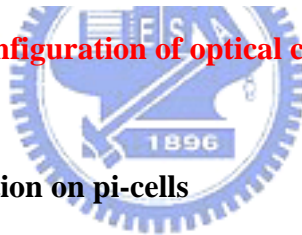


Fig. 2-14 The configuration of optical compensation foils.



2.2.4 Optical compensation on pi-cells

Eliminating the residual phase retardation was proposed to improve the dark-state of pi-cell [38, 39]. As shown in Fig. 2-15, while applying a high voltage, the LC director is aligned along the vertical direction, resulted in a dark state. However, because of the pretilt, the LC director adjacent to the substrates is slightly inclined. This inclination results in the light leakage of dark state. To resolve this issue, Prof. T. Uchida proposed using a combination of wave-plates to compensate the remained phase retardation caused by the LC director adjacent to the substrates, as shown in Fig. 2-16. By using the same concept, we will be able to compensate the relaxed bend state stabilized pi-cell (discussed in chapter 4).

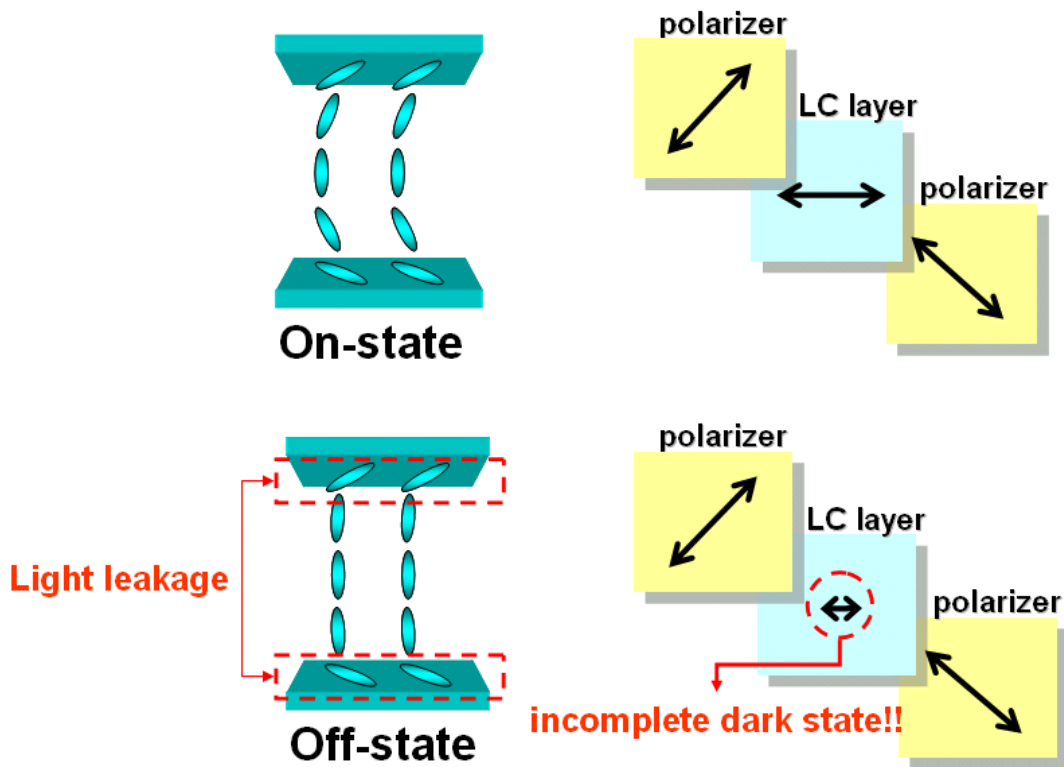


Fig. 2-15 Incomplete dark state under high electrical field in a pi-cell.

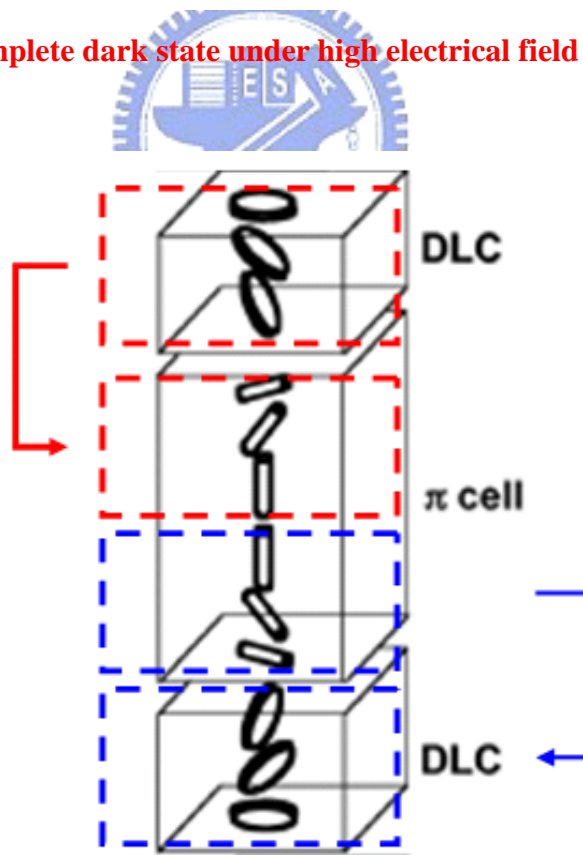


Fig. 2-16 Compensation mechanism of using wave-plates on the pi-cell.

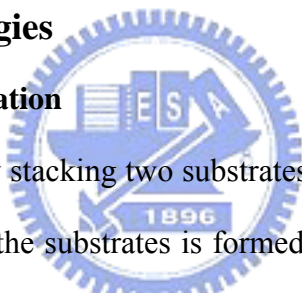
Chapter 3

Device fabrication and measurements

The basic fabrication technologies including LCD and OLED processes are described in this chapter. These fabrications will be used to make our designed devices. After the devices being fabricated, the characterizations of the optical performance, LC director profile, and device cross-section are measured with the conoscopic system, the spectroscopic ellipsometry, and the focus ion beam assisted scanning electron microscopy (FIB/SEM), respectively.

3.1 Fabrication technologies

3.1.1 LCD device fabrication



An LCD device is made by stacking two substrates with intermediate LC material. As shown in Fig. 3-1, one of the substrates is formed with thin-film-transistor (TFT) array, and the other one is coated with color-filter (CF). The array section of the LCD device is made with conventional TFT fabrication. Generally, for amorphous-Si TFT process, there are 5 sequences of masks for lithography. Each sequence includes UV light exposing, developing, removing, etching, depositing, and polishing. The CF section is made with black matrix, color filter resin, and Indium-Tin-Oxide (ITO). After the substrates being prepared, the polyimide (PI) is then coated on the substrates to align the LC molecules. Subsequently, the roller with woolen texture is used to rub on the PI coated substrate. After that, the spacers are sprayed on the substrate to sustain the cell gap, and the top and bottom substrates are assembled. Afterwards, the assembled substrates is filled with LC material and attached with polarizers. Finally, the external circuits are connected to the LCD device [40].

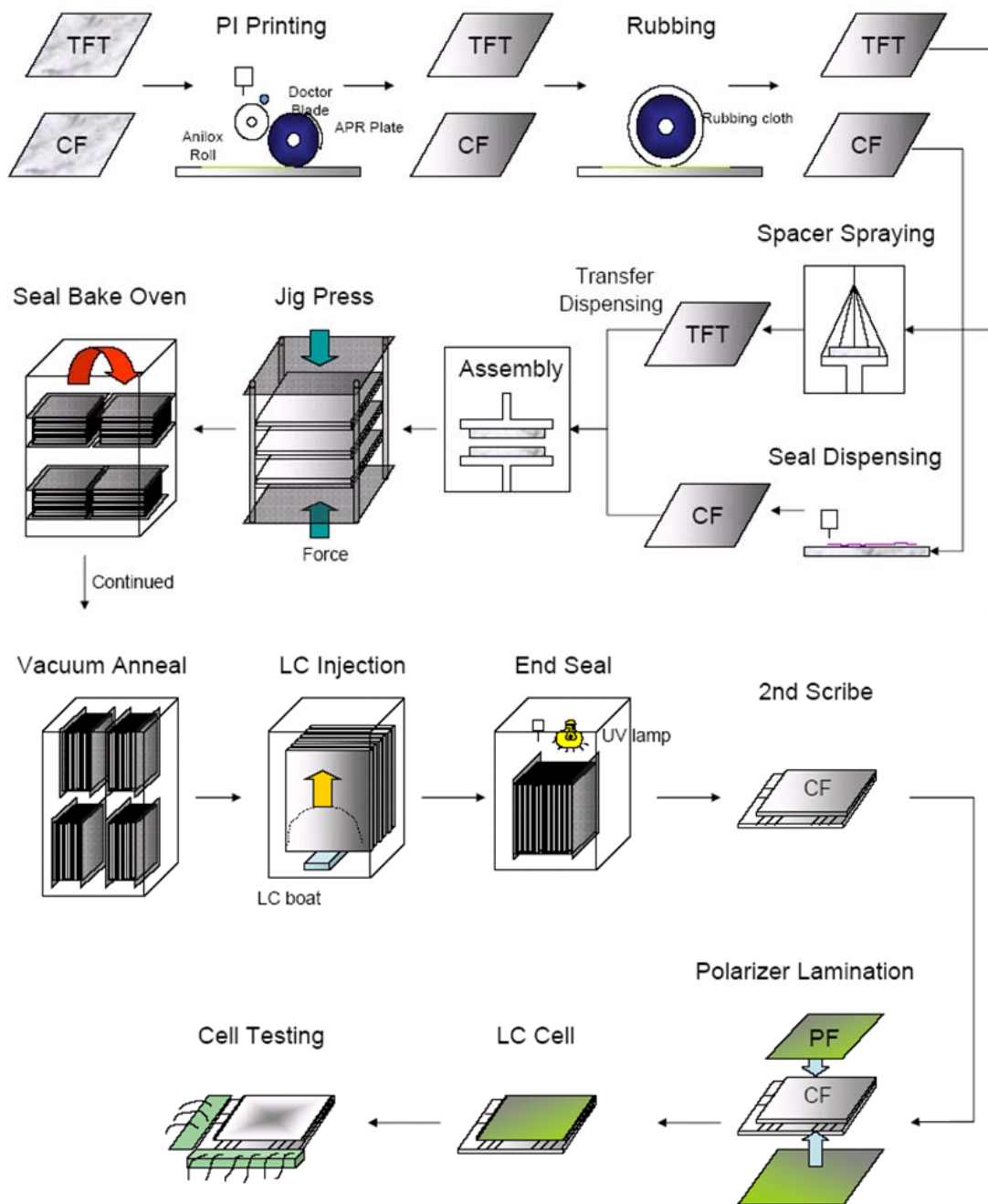


Fig. 3-1 Standard LCD fabrication.

3.1.2 OLED device fabrication

A conventional OLED can be made by stacking the organic semiconductor between an anode and a cathode. This fabrication can be carried out by chemical vapor deposition (CVD) and physical vapor deposition (PVD). As shown in Fig. 3-2, the OLED fabrication process is executed as follows: cleaning the prepared ITO glass,

shaping the ITO anodes, depositing the organic layers, forming the cathodes, and finally encapsulating with a glass lid [41-44].

The performances of an OLED can be improved by modifying the device structure. For example, to increase the light efficiency, the carrier injection and transportation can be optimized by depositing electron injection layer, electron transporting layer, hole transporting layer, and hole injection layer. In addition, to increase the lifetime of OLED, the passivation can be made with multi-layer thin-film-encapsulation [45, 46].

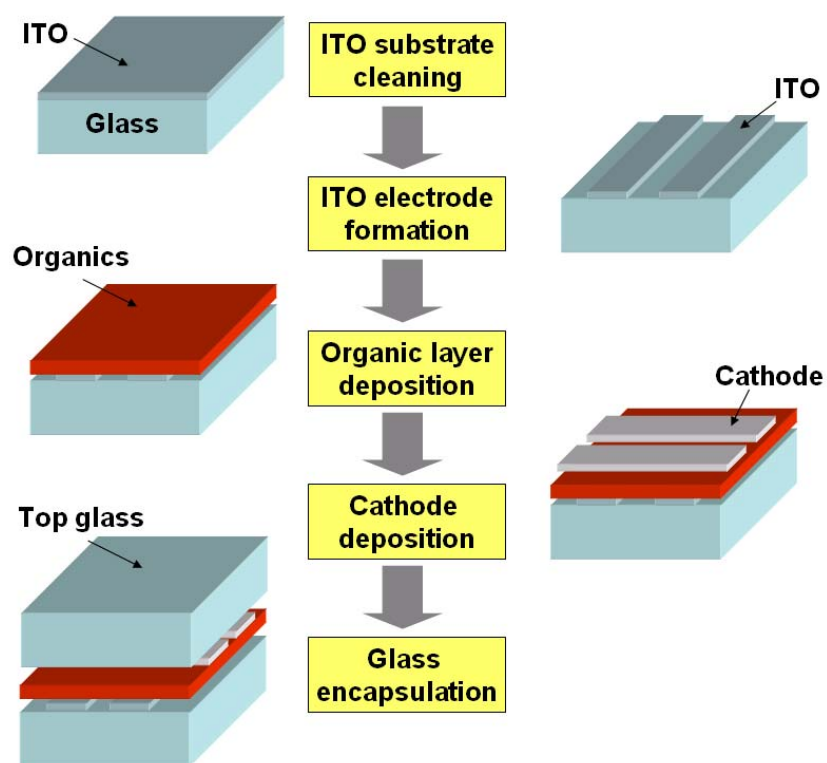


Fig. 3-2 Standard OLED fabrication.

3.2 Measurement instruments

3.2.1 Conoscopic system

The conoscopic instrument is used for measuring the optical properties of brightness and contrast ratio at different angles [47-51]. The conoscopic system has diffusive and collimated illuminations. Also, a plane detector consisting of various directional charge-coupled-device (CCD) sensors is used to detect the transmissive and

reflective lights. This CCD is able to measure the luminance, contrast, and color of the imaging devices simultaneously. The schematic diagram of the measurement setup is shown in Fig. 3-3. Every light beam emitted from the test area with an incident angle θ will be focused on the focal plane at the same azimuth (i.e. the same position on the captured image). The angular characteristics of the sample are thus measured simply and quickly without any mechanical movement.

Experimentally, the measurement of conoscopy is executed as follows: First, the diffusive ambient light source is reflected by the sample. Second, the light with the same inclination propagates in parallel to enter the lens system. Third, the parallel rays are converged to a detector. Finally an iso-contrast contour is formed and stored by a data processor.

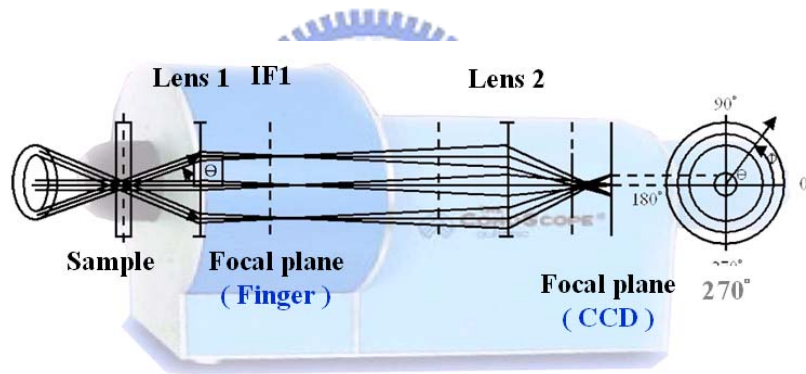


Fig. 3-3 Display measurement setup of Conoscope.

The contrast ratio of an LCD is conventionally defined as the ratio of on-state to off-state luminance, as described by Eq. 3-1. However, this kind of contrast ratio may not be proper for characterizing a reflective type LCD (R-LCD). Thus, Prof. S. T. Wu proposed using ambient-contrast-ratio (ACR) instead. This kind of contrast ratio took the ambient light into consideration, as described in Eq. 3-2 [52].

$$CR = \frac{L_{ON}}{L_{OFF}} \quad (3-1)$$

$$ACR = \frac{L_{ON} + R}{L_{OFF} + R} \quad (3-2)$$

Although this parameter is more suitable than the conventional contrast ratio to describe the performance of R-LCD, it still can not entirely exhibit the image quality of the R-LCD. This issue can be seen by Fig. 3-4, where the glare light does not increase the image quality.

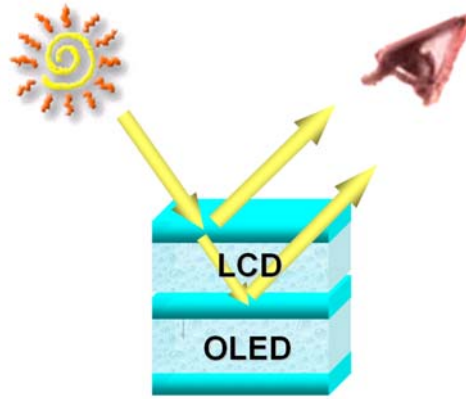


Fig. 3-4 Conventional measurement for R-LCD. Where the glare component does not contribute to the image quality but still be included in the contrast ratio.

Therefore, we further eliminate the glare light by the segment recording function. As shown in Fig. 3-5, this function is executed by using a bar which successively rotates a certain degree and captures the specific light field (where the diffusive light source is mounted on the bar, and the planar detector captures the whole light field except the segment at the glare angle). By integrating all of the captured images, the final image has no glare component.

To simulate the image quality under sunlight ambience in a more pertinent way, we define a glare-free-ambient-contrast-ratio (GFA-CR) as follows:

$$GFA-CR = \frac{L_{ON} + L_{R-ON} - L_{Glare}}{L_{OFF} + L_{R-OFF} - L_{Glare}} \quad (3-3)$$

where L_{ON} is the device luminance of the on-state in OLED mode, L_{OFF} , the

off-state. L_{R-ON} is the reflected ambient light of R-LCD mode in on-state, L_{R-OFF} , off state. L_{Glare} is the light reflected from the glare angle. The GFA-CR is more appropriate than A-CR for investigating the performance of R-LCD since the glare component gives no contribution to the image quality.

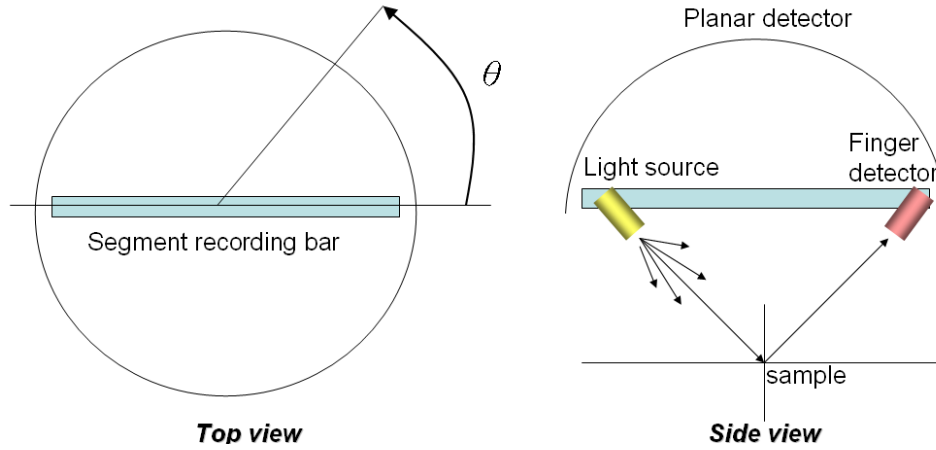


Fig. 3-5 Segment recording function.

3.2.2 Spectroscopic ellipsometry

As discussed in chapter 2, the parameters including the elastic constants, pre-tilts, birefringence, and cell gap affect the performance of an LCD device significantly. To accurately examine these parameters, the spectroscopic ellipsometry is used for this purpose. The measurement setup is shown in Fig. 3-6. The polarization state of incident light is pre-determined by a polarizer. After the light reflected by the sample, the polarization state is altered. The amplitude and phase of the polarization alteration can be measured by the analyzer (occasionally accompanied with a compensator). By varying the angle of incident light, the inclination of sample, and the corresponding orientation of compensator, the following equations can be obtained. [53-55]

$$\tan(\Psi)e^{i\Delta} = \frac{r_{pp}}{r_{ss}},$$

$$\tan(\Psi_{ps})e^{i\Delta_{ps}} = \frac{r_{ps}}{r_{pp}},$$

$$\tan(\Psi_{sp})e^{i\Delta_{sp}} = \frac{r_{sp}}{r_{ss}},$$

where Ψ denotes the amplitude ratio, Δ , the phase change, r , the reflectance under different cases. By these equations, the refractive index (n), extinction coefficient (k), and cell-gap (d) can be determined by numerical fitting.

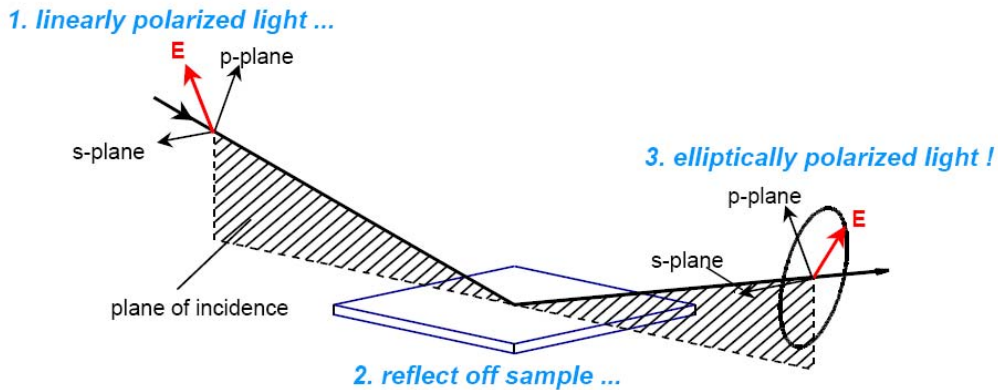


Fig. 3-6 Experimental setup of a spectroscopic ellipsometry.

For the purpose of optical compensation design, we utilize this technique to measure the phase retardation at various viewing angles. As shown in Fig. 3-7, the stage carries a transparent cell, and this cell can be rotated to vary the incident angle (to simulate the case of observing the cell in different viewing angles). This technique will be used to measure the viewing-angle dependent phase retardation and LC director profile in chapter 4.

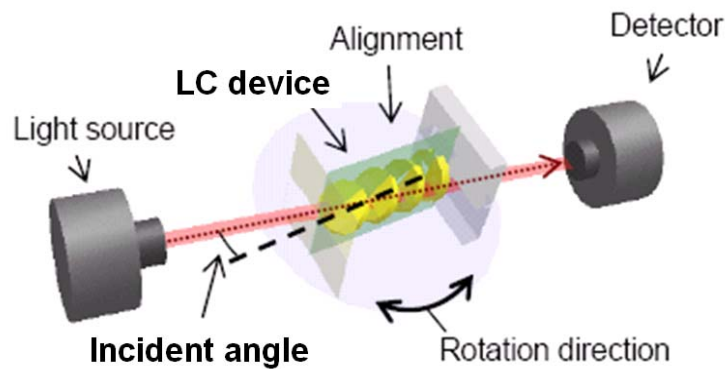


Fig. 3-7 Methodology of using spectroscopic ellipsometry to characterize parameters of an LC cell.

3.2.3 Focused ion beam assisted scanning electron microscopy

The scanning electron microscopy (SEM) is used to observe the nano-structure in our fabricated devices. The operational principle of SEM is to use a high energy beam of electrons to scan the sample surface. By detecting the signals from the back-scattering and secondary electrons, the topography of the sample can thus be obtained. To investigate the cross-section of devices, the focus ion beam (FIB) is used to carve the surface, after that, the SEM is used to capture the image of cross-section, as shown in Fig. 3-8 [7].

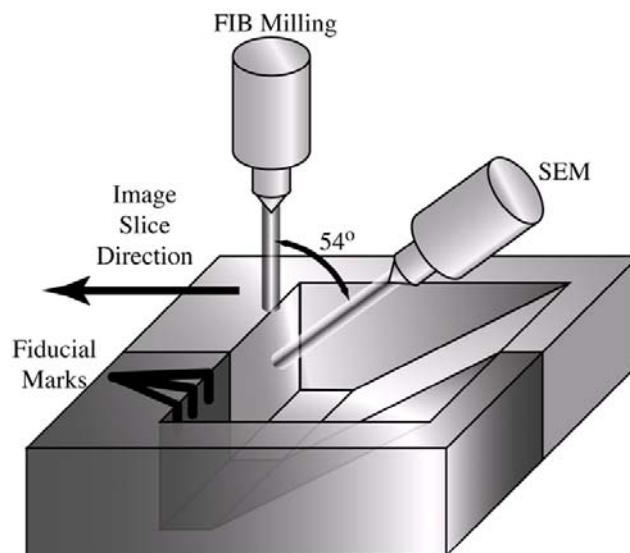


Fig. 3-8 Focused ion beam assisted scanning electron microscopy

Chapter 4

High dynamic range LC mode in a pi-cell

4.1 Introduction

The liquid crystal (LC) pi cell [16], also known as the optically compensated bend (OCB) mode [55-57], is noted for its fast switching rate owing to its symmetric LC profile and parallel backflow. Generally, it is operated in the bend state; however, because of the topological difference between the ground splay state and the bend state, a nucleation transition has to be completed to operate the pi cell in the bend state. As shown in Fig. 4-1, this transition is initiated by applying a critical voltage in advance to prime the cell from the splay states to the bend state, and the voltage has to be kept larger than the critical voltage to sustain the device in the bend state; otherwise, the pi-cell may collapse into the splay or twist states. In TFT-LCD applications, owing to the limits of the driving circuit (giving a maximum applied voltage of 6 V) and the requirement of a sustained voltage to prevent recovery of the splay state, the pi cell is generally driven in the range between 2 V ~ 6 V [58]. Because of this limited range, the contrast ratio of pi cell was not exploited fully.

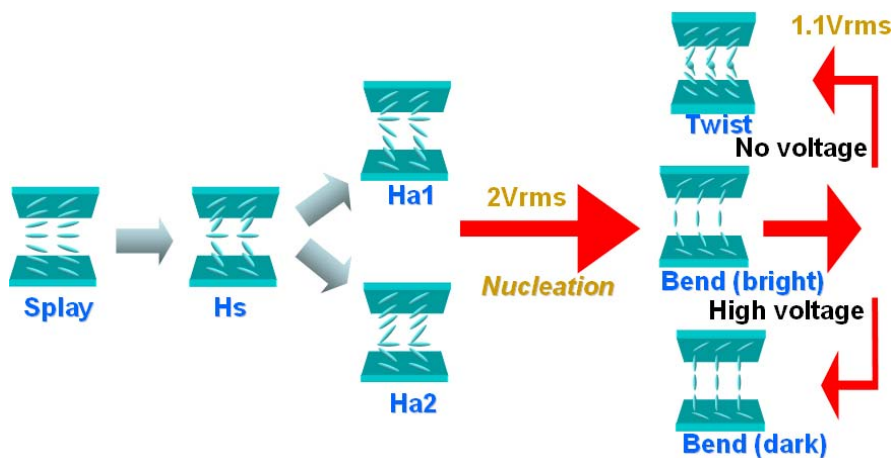


Fig. 4-1 Inter-state transition in a pi-cell.

To prevent the recovery from the bend state to the splay state, several techniques have been proposed [59-65]. These techniques can be classified into two categories: one is to stabilize the twist or bend state so that the bend state can be formed without priming from the splay state [59-64]. The other category is to use intermittent impulse signals to prevent the recovery [65].

In the case of stabilizing the pi-cell in the twist state, because the bend and the twist states need different optical compensations [66], it is difficult to exploit the full optical dynamic range consisting of both states. As for stabilizing the pi-cell in the bend state, the bright state tends to be suppressed to a lower brightness, as shown in Fig. 4-2. Because the polymer wall tends to fix the LC director, the switching freedom of the LC director is reduced.

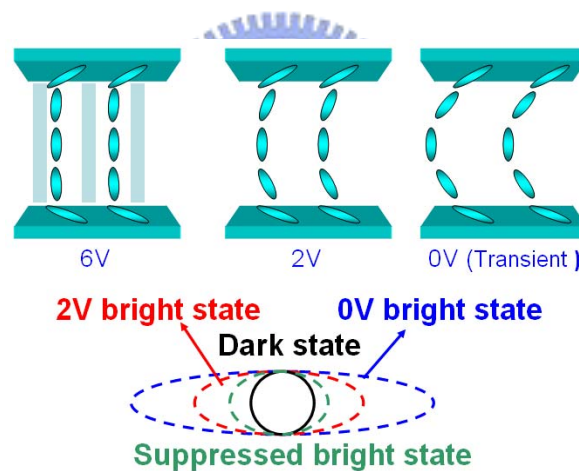


Fig. 4-2 Suppressed bright state after polymer-stabilization.

Using intermittent impulse signals to drive the pi-cell allows the desired voltage to be lower than the critical voltage, and the device can still sustain in the bend state. Because the bend state has no sufficient time to recover into the splay and twist states, the desired level can be sustained for a short period (around several tens ms) [65]. In this method, it has been reported to have a relaxed bend state with the highest phase retardation among the range of the bend states, as shown in Fig.4-2 [65]; however,

even with high voltage impulses, it still has tendency of recovery.

To take the advantages of the methods mentioned above, we propose to combine the concepts of using the impulse driving method and stabilizing the pi-cell with polymerization. This combined method is able to stabilize the non-permanent relaxed bend state, which thus makes the pi-cell have higher brightness and higher switching freedom of the LC director; additionally, this fabricated pi-cell has no risk of recovery into the splay and the twist states.

4.2 Preliminary observation on the relaxed bend state

4.2.1 Observation with the polarizers incorporated optical microscopy

To examine the existence of the relaxed bend state, we make some observations with polarizer assisted optical microscopy. The concept of this experiment is shown in **Fig. 4-3**. We place the rubbing direction of the pi-cell parallel to one of the crossed polarizers. As long as there is extinction of light, the pi-cell stays in the bend state; otherwise, the twist state.

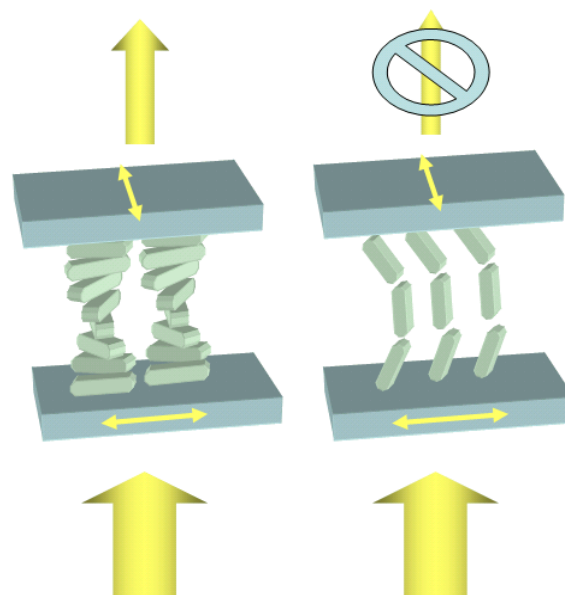


Fig. 4-3 Placing the rubbing direction of the pi-cell parallel to one of the crossed polarizers to examine the occurrence of twist state.

To observe the phase transition of a pi-cell, we place the rubbing direction of the pi-cell parallel to one of the crossed polarizers. The LC cell used here is an E7 (from Merck) filled pi-cell with cell gap of 5.5 μm . A continuous waveform of 10 kHz, 20 V_{pp} , and sine wave is applied to the cell. The mechanism of the relaxation can be clearly defined since the bend state has extinction, whereas the twist state does not. As the optical microscopy results shown in Figs. 4-4 and 4-5, in the first stage, the bend state is totally dark owing to its extinction. And then, with the abruptly releasing of applied voltage, the bend state is relaxed and induced tiny amount of light leakage (there is no texture). After that, the texture forms and intensity increases (i.e. the twist state occurs).

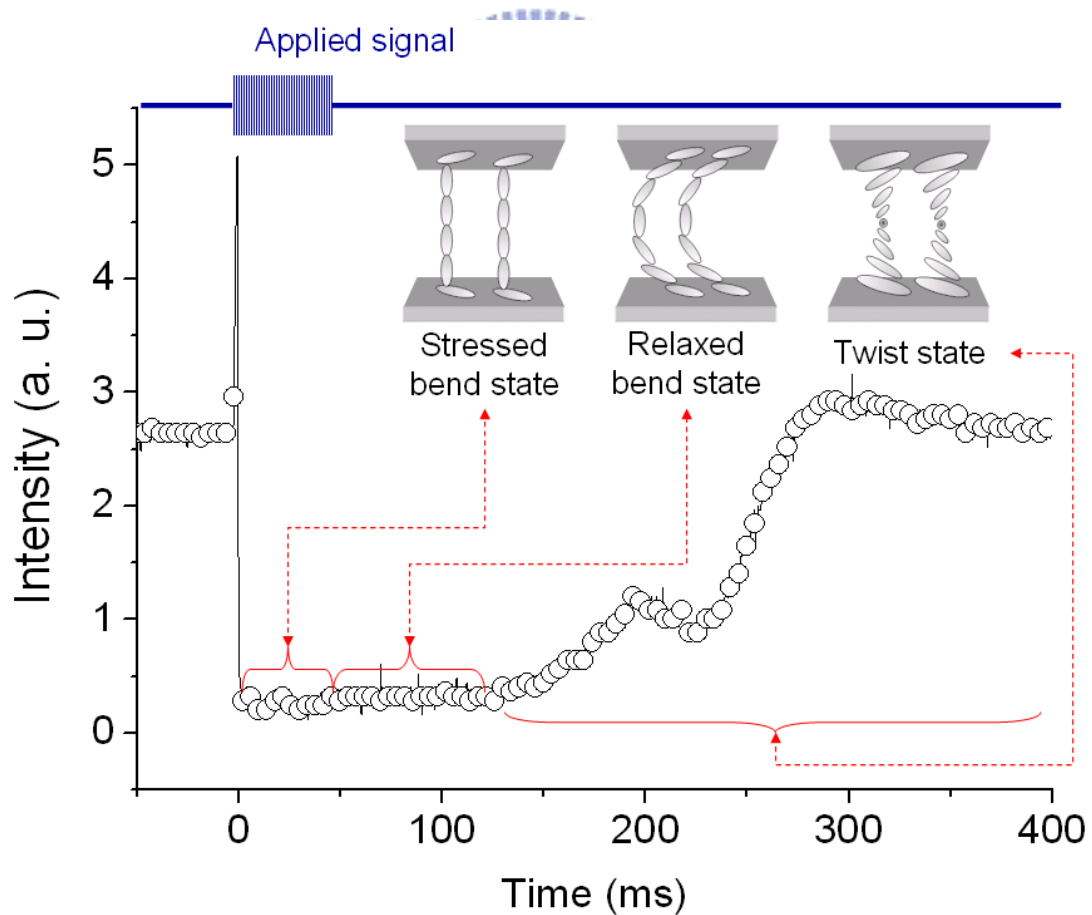


Fig. 4-4 Oscilloscopic image of the bend to twist transition. Note that the rubbing direction of the pi-cell is parallel to one of the crossed polarizers.

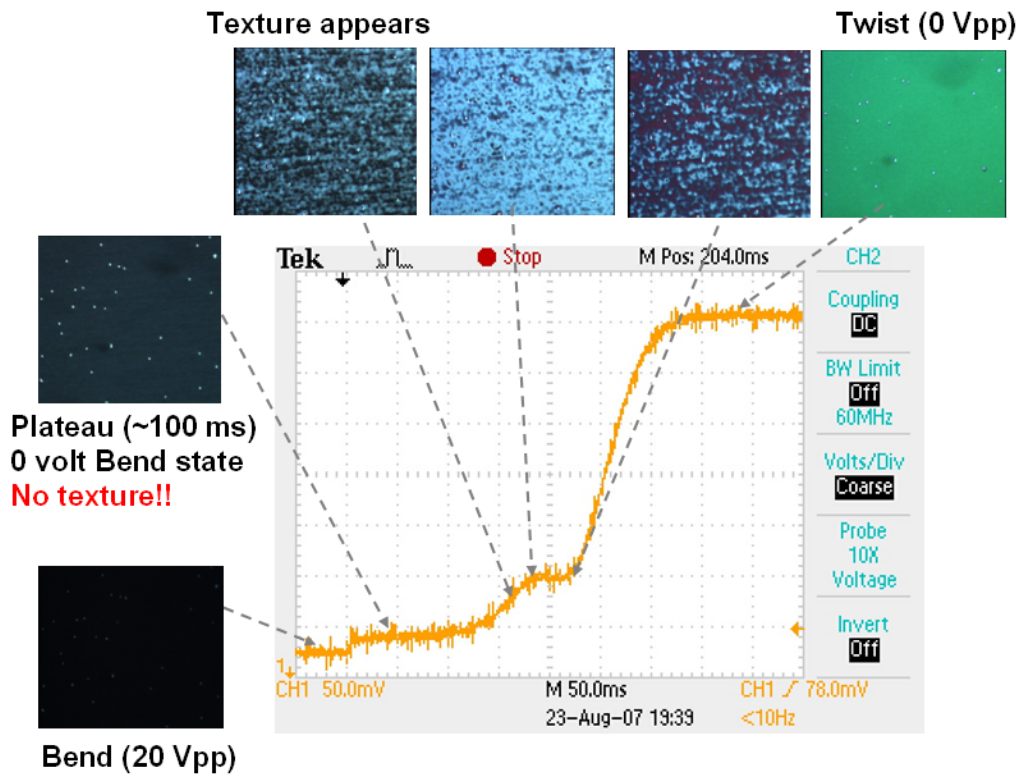


Fig. 4-5 LC texture changing from the bend state to the twist state. Note that the rubbing direction of the pi-cell is parallel to one of the crossed polarizers.

The 0V bend state can be clearly seen by observing its extinction. This result indicates that there is an 80 ms lifetime of the non-permanent relaxed bend state existing right after releasing the voltage impulse.

4.2.2 Observation with the impulse driven pi-cell

To test the driving waveform that we are going to use during the polymerization, we check the impulse waveform with the method described in section 4.2.1. Using the driving waveform as shown in Fig. 4-6, with 40 ms of pulse and 40 ms of rest, the pi-cell sustains in the bend state during the rest (i.e. the relaxed bend state); however, if the impulse is set as 30 ms of pulse and 50 ms of rest, the pi-cell collapses into the twist state.

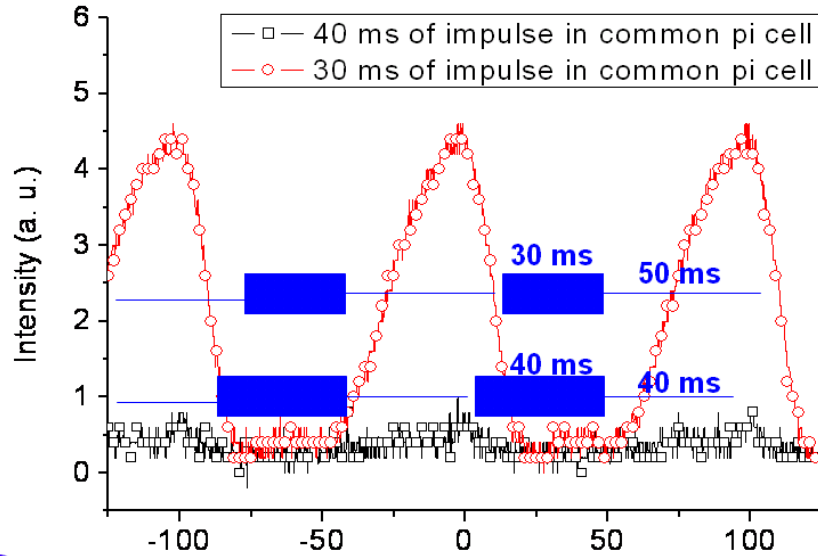


Fig. 4-6 Oscilloscopic traces for demonstrating the impulse driving method.

To view the device appearance during each state upon impulse driving, the photo is taken where the pi-cell's rubbing direction is placed parallel to the crossed polarizers. Fig. 4-7 (a) shows the stressed bend state (complete extinction), Fig. 4-7 (b), the relaxed bend state (extinction with light leakage due to the pre-twist of the pi-cell), and Fig. 4-7 (c), the twist state (full transmission).



Fig. 4-7 Photographs taken while driving the pi-cell with impulse waveform, where (a) stress bend, (b) relaxed bend, and (c) twist states show full extinction, slight light leakage, and full transmission, respectively.

4.3 Fabrication of relaxed bend state stabilized pi-cell

Initially, we pick the empty cells with identical cell gap of $5.5 \mu\text{m}$, and fill them with LC material E7 blended with 4% monomer mixture including 90% reactive

mesogen (RM257 of Merck) and 10% photo-initiator (Irgacure 907 of Ciba Specialty Chemicals). The alignment layers of the pi cell devices are parallel rubbed polyimide.

To stabilize the non-permanent relaxed bend state, we set up a synchronized polymerization system. In this system, as shown in Figs. 4-8 and 4-9, a chopper is used to block the ultraviolet (UV) light and only let the UV light impinge on the pi cell during the desired state, a set of laser diode (LD-1) and photo-diode (PD-1) is used to monitor the transmission of the pi cell device (signal 1), another set of LD-2 and PD-2 is used to monitor the rotational period of the chopper (signal 2), and PD-3 is placed near the pi cell to detect the impingement of the UV light (365 nm) on the pi cell (signal 3).

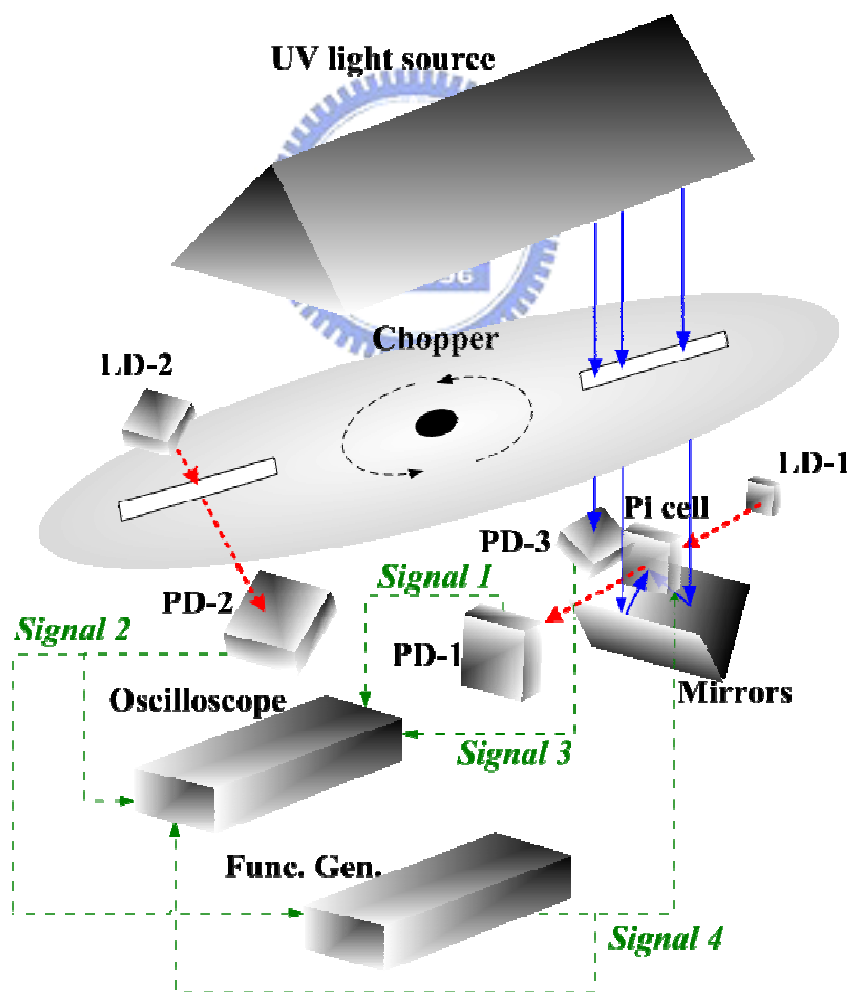


Fig. 4-8 Experimental setup of synchronized polymer-stabilization.

The operational principle of this synchronized polymerization system can be explained by the oscilloscopic traces. As shown in Fig. 4-10, to ensure the signals are synchronized, signal 2 is used to trigger the function generator, thus even the rotational period of the chopper is slightly varied, all of the signals are still phase-locked. The waveform of the function generator is set as burst sine wave with 10KHz, 20 V_{pp} for 50 ms and 0 V_{pp} for 250 ms. This wave form is also recorded by the oscilloscope as signal 4. Moreover, by monitoring signal 3, the desired state to be stabilized can be tuned by varying the delay time (the time between signal 4 applies to the pi cell device and signal 2 triggers the function generator).

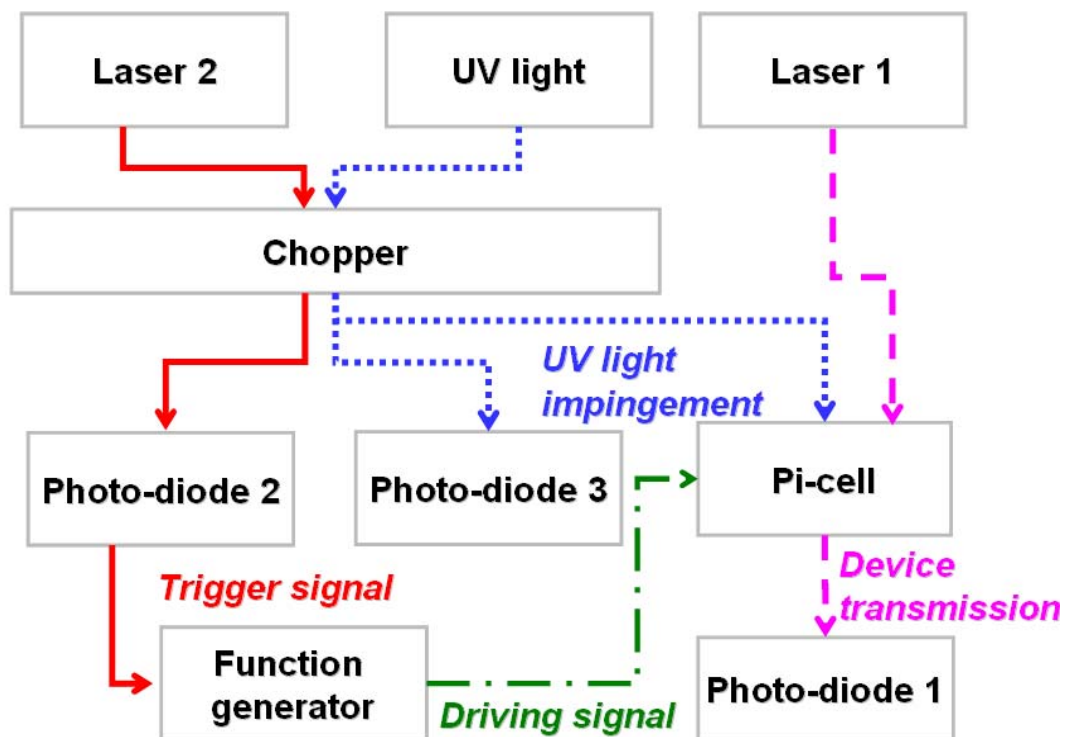


Fig. 4-9 Scheme of synchronized polymer-stabilization.

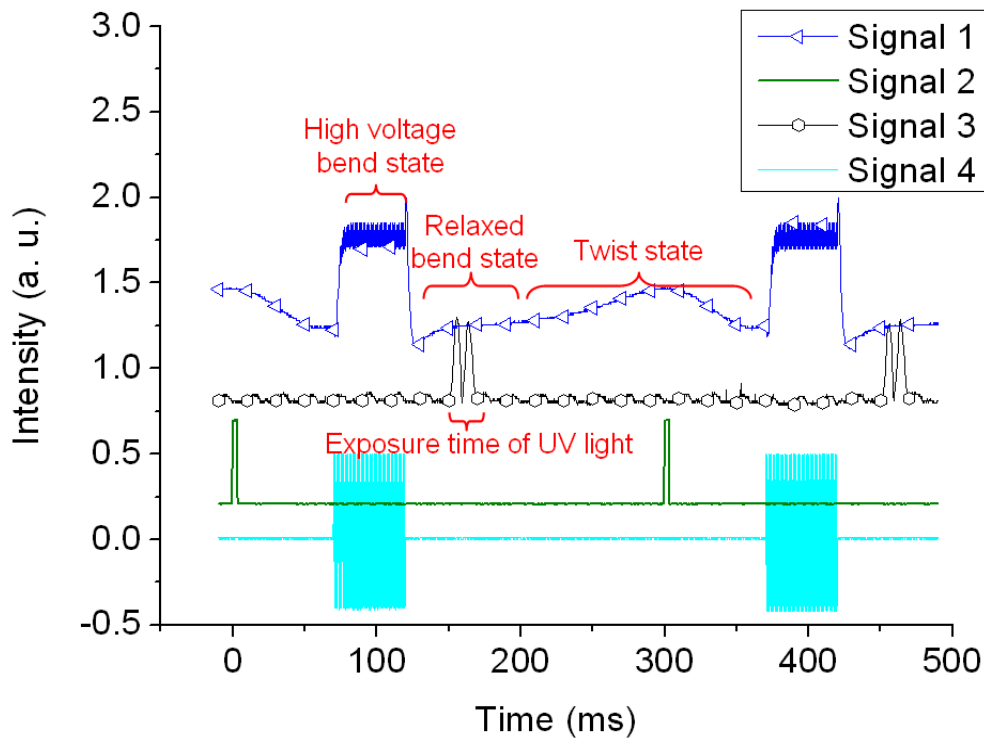


Fig. 4-10 Oscilloscopic traces of synchronized polymer-stabilization.

4.4 Confirmation of LC director profile by spectroscopic ellipsometry

The internal LC alignment distribution (or say the LC director profile) after polymerization is measured by spectroscopic ellipsometry. Measuring the polymer-stabilized pi-cells without applied voltage can verify their equilibrium LC profiles. The LC profiles in the directions of parallel and perpendicular to the rubbing direction are measured as shown in Fig. 4-11.

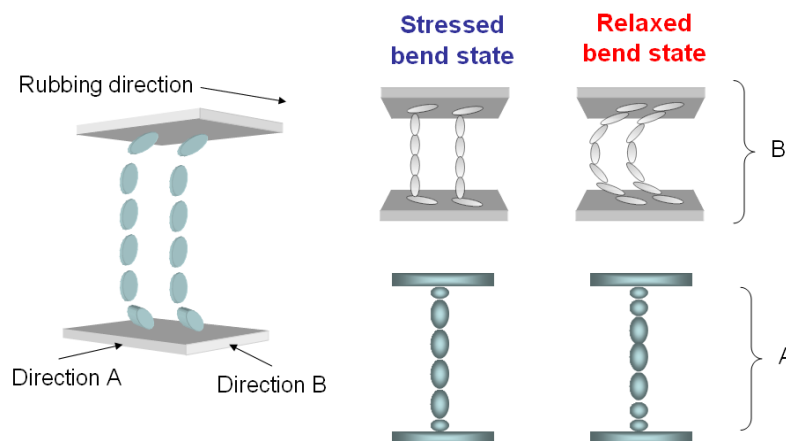
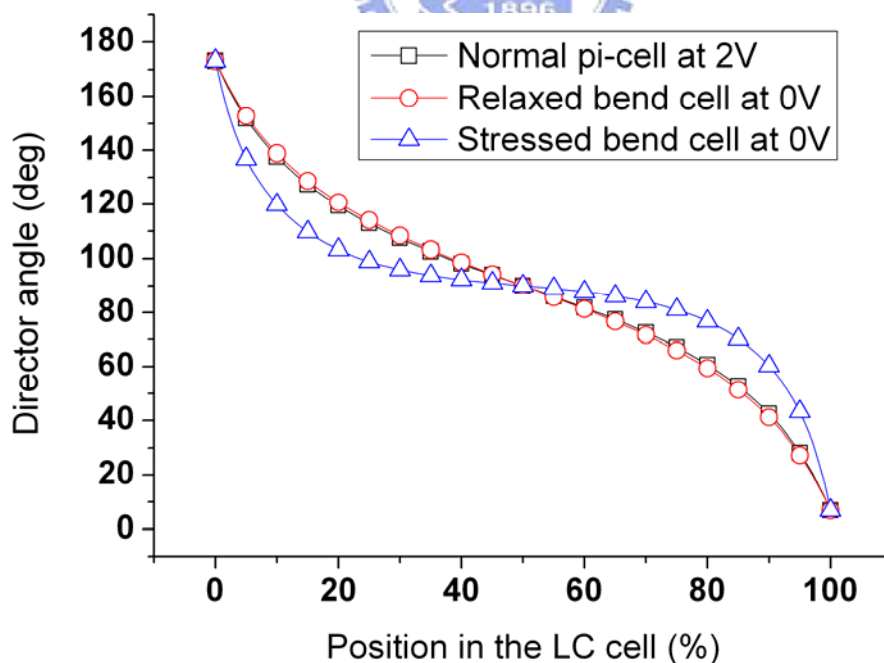
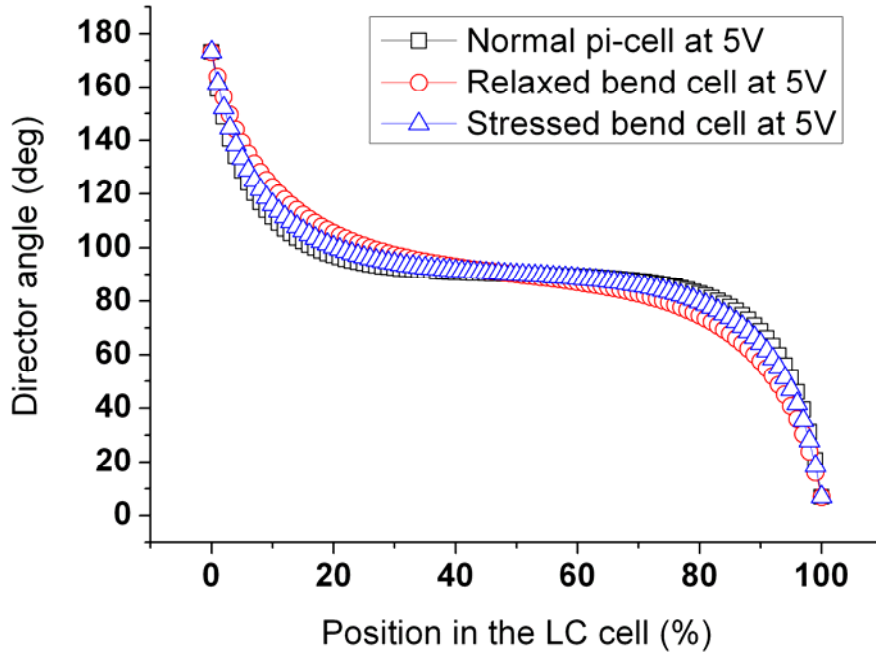


Fig. 4-11 Method used for verifying the LC profile of relaxed bend state.

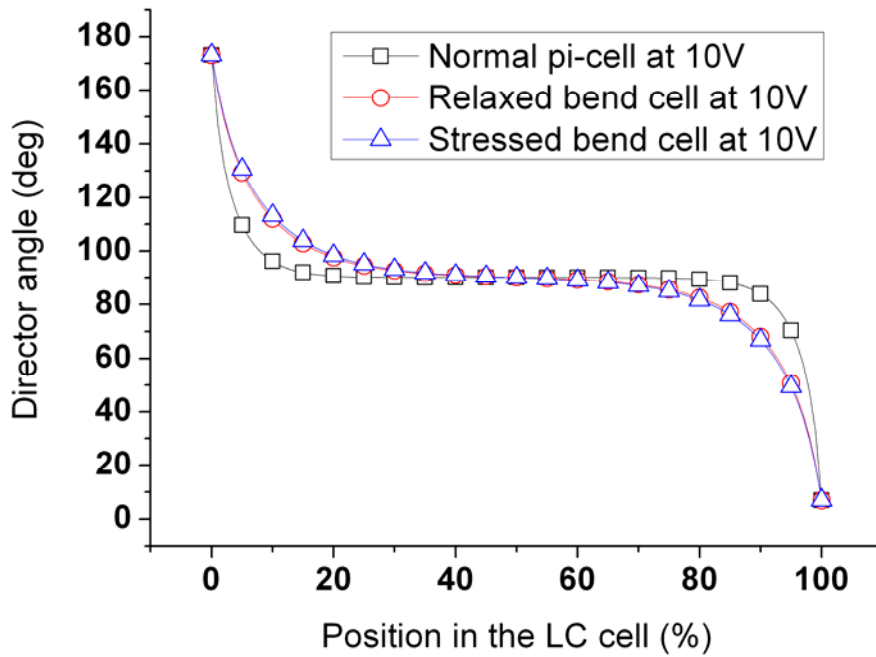
The measurement results verify that the LC profile of relaxed bend state has a comparably lower tilt angle of LC directors at 0V. As shown in Fig. 4-12 (a), the LC profile of relaxed bend state is very similar to the case of normal pi-cell at 2V, which is the lowest bend state among the bend states in a normal pi-cell. This figure also points out another two main phenomenon of our polymerized pi-cells. First, the polymerized cells are stabilized in the bend states, since the central LC director at 0V is measured to have a tilt angle of 90°. Second, the LC director profiles at 10 V in Fig. 4-12 (c) demonstrate that the polymerized pi-cells are not able to achieve entirely vertical alignment, which thus results in an incomplete dark state. However, considering the TFT-LCD application whose range of driving voltage is 0~6V, the characteristics of the relaxed bend state and normal pi-cell are similar (according to Figs. 4-12 (a) and (b)). Additionally, the relaxed bend state stabilized pi-cell has no tendency to recovery, which shows its superiority over the normal pi-cell.



(a)



(b)



(c)

Fig. 4-12 The LC profiles measured by spectroscopic ellipsometry at (a) lowest bend, (b) 5V bend, and (c) 10 V bend states.

4.5 Results

The transmission/voltage behavior of the stabilized pi cells is measured by placing their rubbing direction at 45° to the crossed polarizers. The driving signal is a 10 kHz square wave and gradually increases from 0 V_{rms} to 15 V_{rms}. As shown in Fig. 4-13,

considering the conventional driving range of OCB mode TFT-LCD ($2 V_{\text{rms}} \sim 6 V_{\text{rms}}$, square wave) [58], the intensity operational range (the difference between the highest to the smallest intensity) of the original pi cell is $0.525 (\overline{AB})$. However, the reason that the OCB mode is conventionally operated with voltages larger than $2 V_{\text{rms}}$ is to prevent its transition from the bend state to the twist state. Since the polymerized pi cells have been stabilized in the bend state, the optical compensation can still work even at $0 V_{\text{rms}}$; therefore, the driving range of the polymerized pi cells can be further extended from $2 V_{\text{rms}}$ to $0 V_{\text{rms}}$. In this case, the intensity operational range of the RB state stabilized pi cell is $0.375 (\overline{CD})$ while that of the best case of the conventional polymerization stabilized pi cell is $0.25 (\overline{EF})$.

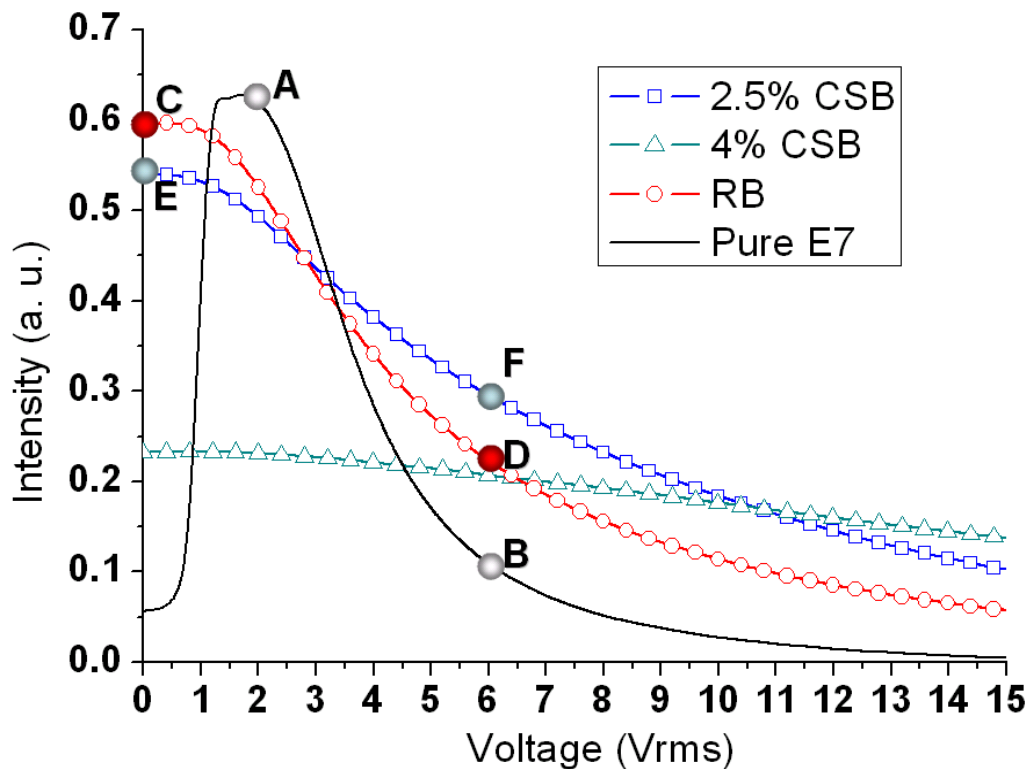


Fig. 4-13 Transmission-voltage relations of pi cells.

To visualize the contrast difference between the pi-cells, the photographs of the pi-cells have been obtained. In Fig. 4-14 (a), photographs on the ON-state of the conventionally-polymerized stressed bend state (CSB), the RB stabilized, and the

normal pi-cells (applying $2V_{rms}$ on the normal pi-cell to prevent the undesirable recovery) are obtained. Fig. 4-14 (b) shows the OFF-state of the CSB, RB, and normal pi-cells. Compared with the CSB pi cell [61], the RB state stabilized pi-cell has no dynamic range suppression.

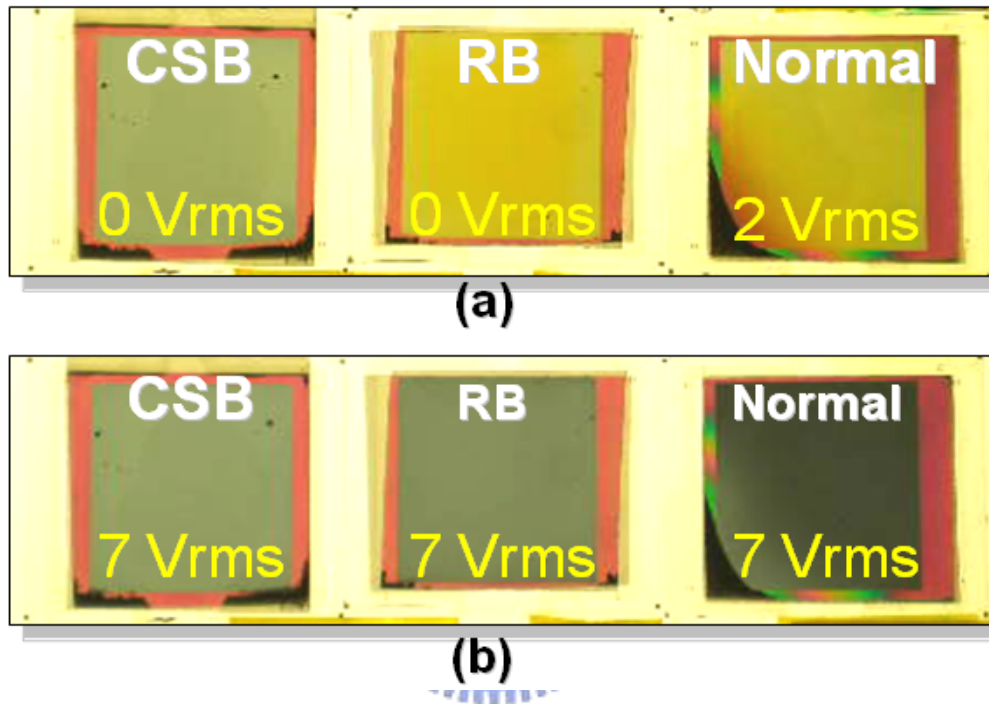


Fig. 4-14 Comparison between the different pi-cells whose rubbing directions are placed at 45° to the crossed polarizers, where the pi-cells are operated in the (a) on-state and (b) off state.

The viewing angle dependence of phase retardation is measured by spectroscopic ellipsometry. As shown in Fig. 4-15, the relaxed bend stabilized pi-cell without applied voltage has similar phase retardation with the case of normal pi-cell at 2V (the lowest bend state). Their contrast ratios can be seen by the difference between the switch-on and switch-off states. The difference in the case of RB state stabilized pi-cell is much higher than that in the case of CSB pi-cell.

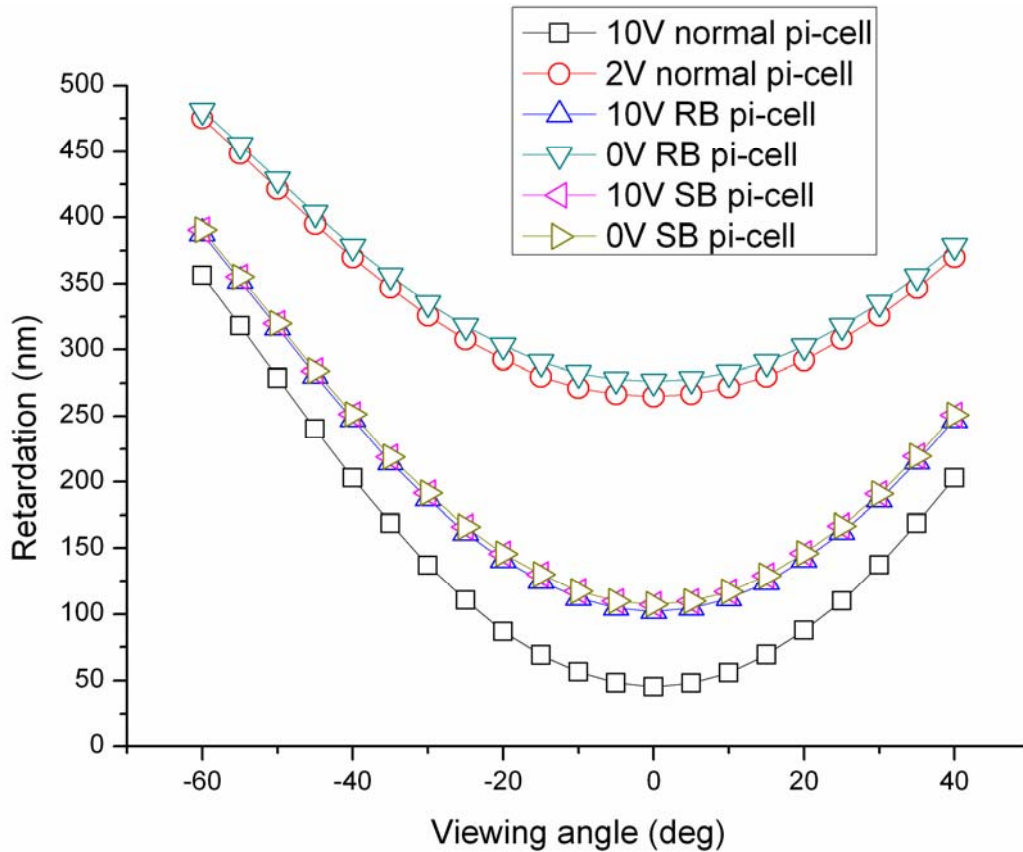


Fig. 4-15 The viewing-angle dependent phase retardation of the pi-cells.



The response times of the stabilized pi cells are also measured with the same experimental arrangement with a driving signal of a 10 kHz, burst square wave (with 15 ms of 15 V_{pp} and 15 ms of 4 V_{pp}). As shown in Fig. 4-16, the switch-on times (90% to 10%) of the pi cells with pure E7, when stabilized in the RB state, and when stabilized with conventional polymerization (the case of 2.5 % mesogen) are 0.73, 2.44, and 2.42 ms, and the switch-off times (10% to 90%) are 4.4, 8.4, and 6.3 ms. The RB stabilized pi cell has slower response, which results from its less rigid (or say less well-constructed) polymer fibril, since the polymerization is executed with dynamic flow.

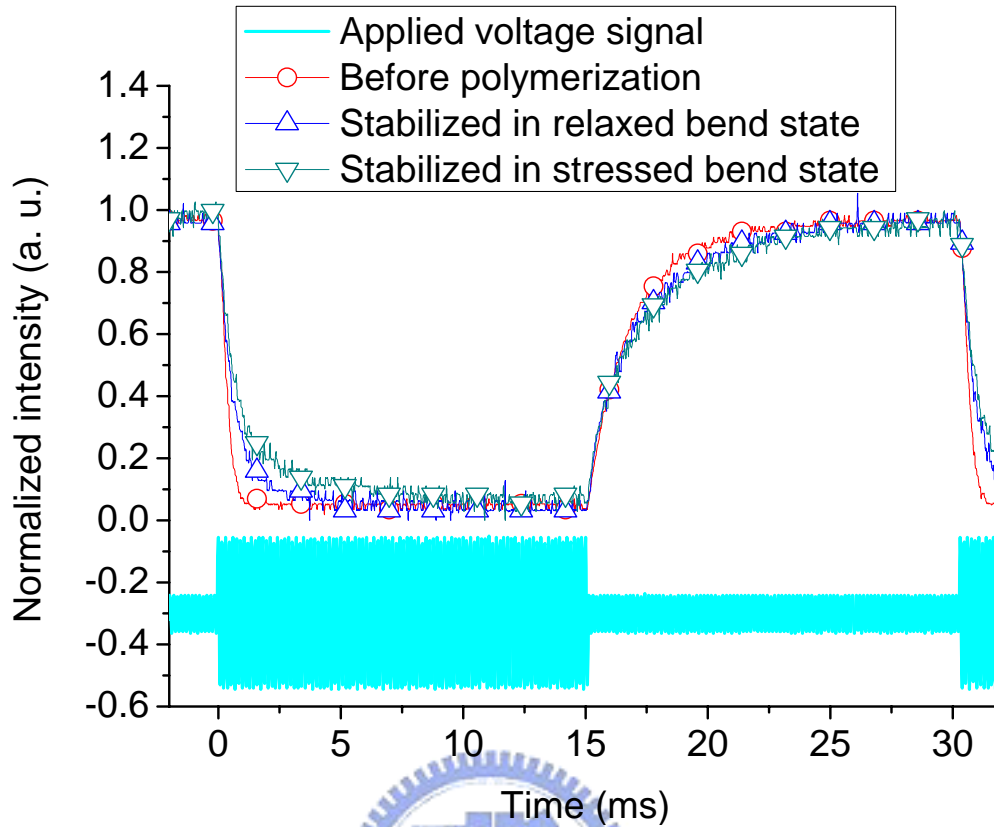


Fig. 4-16 Response times of the pi cells. The pi-cells are positioned at 45° to the crossed polarizers.

4.6 Discussion

Considering the response time of the polymerized pi-cells, although a commercial pi cell is capable of performing with an overall response time of around 3 ms, the LC material we use here is simply E7, so the response time can be further optimized by using low viscosity LC materials. Moreover, we can increase the switching speed of this proposed pi cell by a dual frequency driving method [64, 68, 69].

As for the incomplete dark state under 10V, if we consider the TFT-LCD application whose range of driving voltage is 0~6V, the characteristics of the relaxed bend state and normal pi-cell are quite similar (according to Figs. 4-12 (a) and (b)). Additionally, the relaxed bend state stabilized pi-cell has no tendency to recovery, which shows its superiority over the normal pi-cell.

To compensate the relaxed bend state profile, we calculate the profile of the

compensation film based on the principle described in section 2.2.3. To make the total phase retardation as 0, the discotic LC materials can be oriented as Fig. 4-13 to compensate the corresponding LC directors in the relaxed bend state stabilized pi-cell.

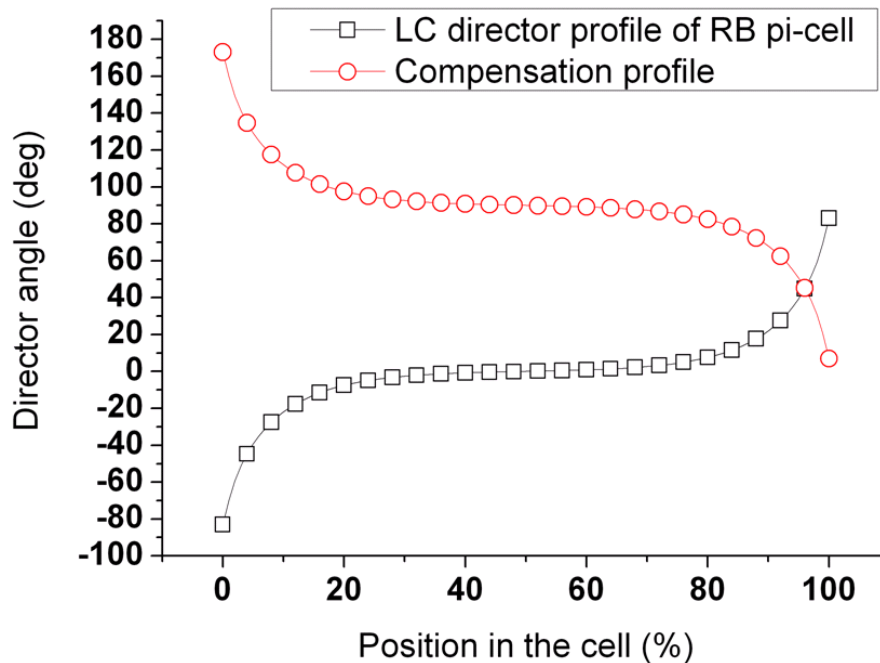


Fig. 4-17 Proposed optical compensation for the relaxed bend state stabilized pi-cell.

4.7 Summary

The difference of the intensity operational range results from the various profiles of LC director after polymerizations. In the case of the pi cell stabilized in the RB state, the LC director throughout the device is stabilized in a more relaxed (i.e. lower tilt) state, which thus has higher freedom of switching compared with the pi cell stabilized with conventional polymerization. To further increase the intensity operational range, we have tried to lower the concentration of the reactive mesogen for synchronized polymerization (it was reported in ref. 62 that using lower concentrations results in higher intensity operational range); however, using concentrations lower than 4% produces only partial stabilization of the bend state.

We have demonstrated a synchronized polymer-stabilization technique which can

be used to stabilize the non-permanent states in LC devices. In this thesis, the non-permanent RB state reported to have high brightness [63] is observed and stabilized by our proposed technique. This pi cell stabilized in the RB state has the attributes of high intensity operational range (an enhancement is obtained by a factor of 1.5 compared with the best case of the conventionally polymerized pi cell) and feasibility for full dynamic range optical compensation (no twist state occurs during the device operation). This proposed pi cell device can be used with a switching backlight technique to achieve a complete dark state and lower the power-consumption [70].



Chapter 5

Investigation of symmetric H state in a pi-cell

5.1 Introduction

As mentioned in chapter 4, the normal pi-cell needs to be primed to the bend state and sustained with a critical voltage to prevent the undesirable recovery into the twist or splay state [16, 32, 57, 58, 71-75]. In contrast, the symmetric H (Hs) state (a transient state obtained by a sudden application of voltage to the ground splay device) needs no priming – i.e. the Hs state is continuous with the ground state. Moreover, the Hs state has been reported to have the merit of very fast switching, on a scale of 1 millisecond (as shown in Fig. 5-1) [14]. Because of these distinguished features, the Hs state has attracted much attention. In this chapter, we will further investigate its possibility for display applications.

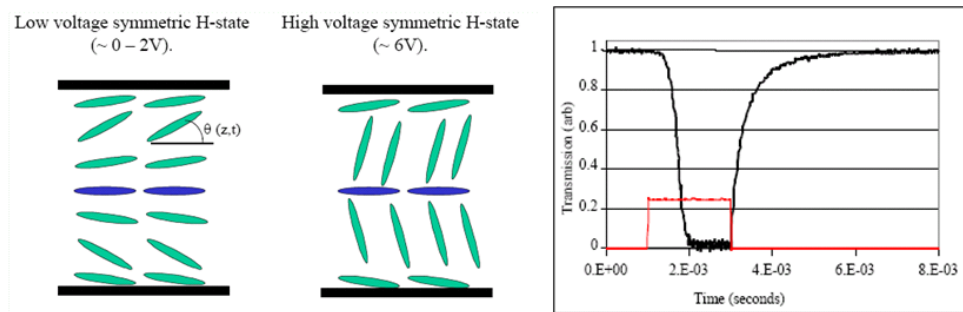


Fig. 5-1 Hs state director profile and its response time [14].

The reason that hinders the Hs state from LCD applications is its short life time (of less than 200 ms, in general). In this chapter, our major objective is to come up with a method for extending its lifetime. Before going to design a structure for this purpose, a direct investigation on the LC profile of the Hs is necessary. So, in the beginning of this chapter, we propose a method for verifying the LC profile of the Hs state, which

was understood only by calculation, but we prove it with direct observation.

After confirming the LC profile of the Hs state, we further propose a method to extend its lifetime. The simulation of this proposed method will be reported, and the fabrication process will also be introduced.

5.2 Investigation of the transient symmetric H state

5.2.1 An introduction of the symmetric H state

In previous work, it was suggested that under field application, the Hs state has an internal director structure in which the director in the centre of the device remains parallel to the surfaces. This “de-couples” the two halves of the pi-cell, thus the cell is effectively divided into two half-thickness Fréedericksz devices, from which the fast switching behavior results. The switching rate enhancement, ignoring the flow effect of the pi-cell, can be explained by

$$\tau \propto \frac{d^2 \gamma}{K_{11} \pi^2} \quad (5-1)$$

where τ represents the relaxation time of the pi-cell, d , the cell-gap, γ , the rotational viscosity, and K_{11} , the splay elastic constant. Thus, the smaller the effective thickness of the switching layer, the faster the device. Some modeling and experimental results have shown the switching rate of Hs state is faster than that of asymmetric H (Ha) state in a pi-cell by a factor of 4, which supports the existence of the central non-switching region, since it de-couples the LC director in the two halves of the cell [14, 76, 77]. This central region and de-coupled switching make the Hs state have a symmetric director profile as shown in Fig. 5-1; however, owing to its short lifetime, no direct evidence has been presented to demonstrate the profile symmetry.

To elucidate the short lifetime issue, a continuous sine waveform is applied to the

pi-cell to observe the phase transition. As shown in Fig. 5-2, when the voltage is applied, the splay (S) state is suddenly switched to the Hs state without nucleation. After that, the asymmetric H (Ha) state forms in the Hs domain and finally engulfs the whole area of Hs state. Meanwhile, the domain wall between the bend state and the Ha state is still moving toward the Ha state side. When the applied voltage is removed, the Ha state turns back to the S state and the bend (V) state turns back to the twist (T) state.

There are two interesting phase transitions observed. One happens during the recovery from V state to T state; the other, Ha state to S state. As the V state recovers to T state, some textures appear along the rubbing direction, as shown in Fig. 5-2. The texture may result from the collision between the LC directors with different laying down directions. These explanations have demonstrated that the bend state is the most stable state among the states in a pi-cell while applying a voltage larger than the critical voltage. Thus, the bend state tends to engulf the Hs state.

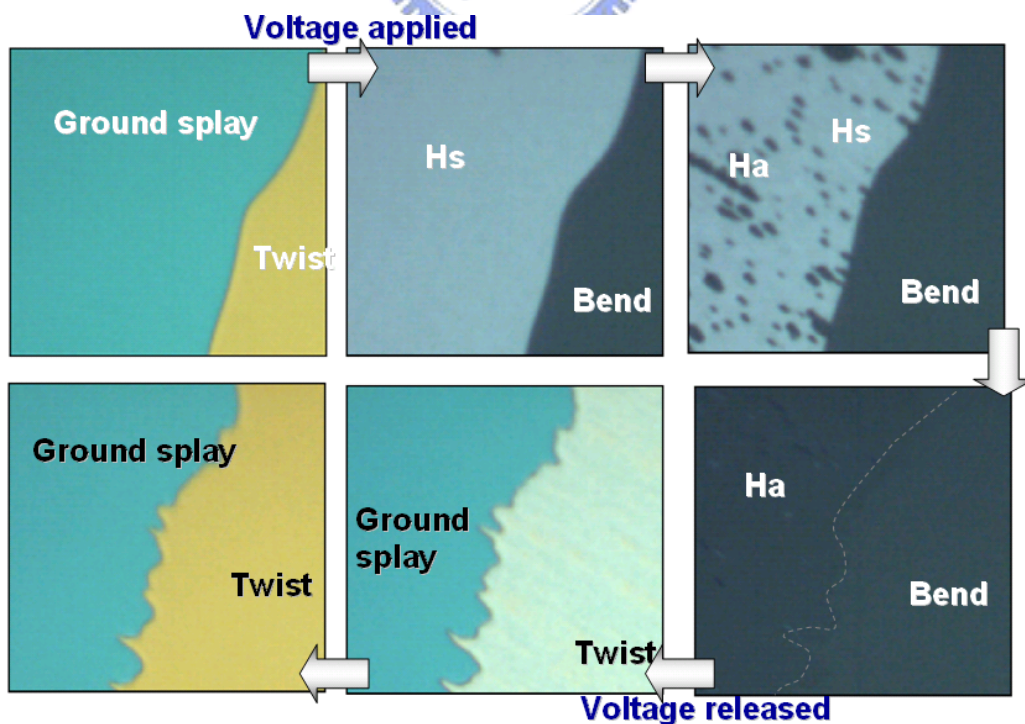


Fig. 5-2 Phase transition by continuous driving waveform.

5.2.2 Preliminary observation on the symmetric H state

To quantify the lifetime of the Hs state and observe the collapsing mechanism, we make the experiment as follows: Initially, a typical pi-cell (with 2.6 μm cell gap, filled with LC material E7 and using parallel rubbed polyimide as the alignment layers) is positioned at 45° between the crossed polarizers and the transmission is measured during signal application. With an impulse voltage signal of $5V_{\text{rms}}$, the intensity variation during the state transitions from the ground splay state, to the Hs and into the Ha states is observed by a photo-detector as shown in Fig. 5-3. The Hs state is observed to have a life-time dependence on the applied voltage. As the applied voltage is increased, generally the life-time of Hs state (in the duration of the Hs plateau in Fig. 5-3) will be longer. However, at higher voltages, the bend state rapidly nucleates and engulfs the whole area of the splay states.

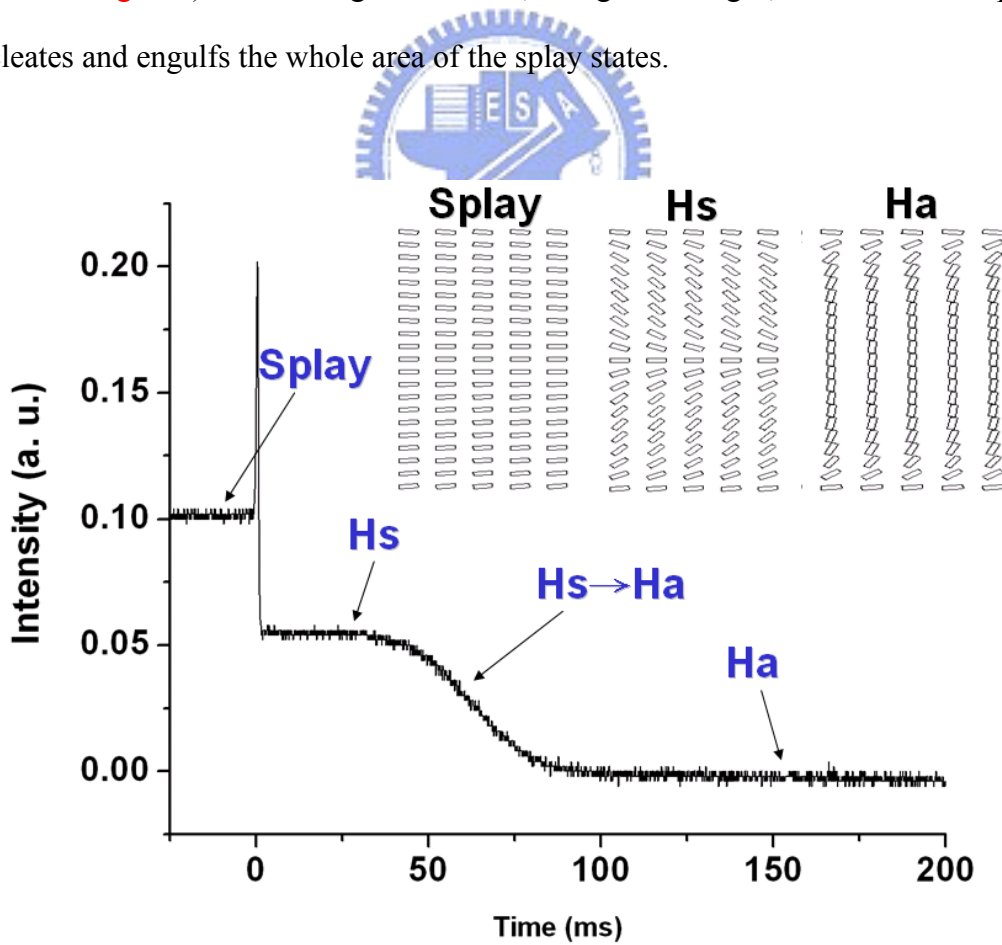


Fig. 5-3 The state transition from splay to Hs to Ha state.

5.2.3 Stroboscopic illumination assisted conoscopy

As the aforementioned descriptions, the difficulty in proving this Hs state LC profile by direct observation was due to the short life-time of Hs state (typically around a few tens ms, although it can be present for hundreds ms in certain circumstances). In this section, we report work where we utilize a burst driving method along with stroboscopic light emitting diode (LED) illumination to capture the conoscopic images for symmetric LC director profile of the Hs state.

It is clear that we can verify the LC profile by comparing the measured conoscopic images with the calculated images. Since the conoscopic contour is affected by LC symmetry, as shown in Fig. 5-4, the contours of Hs state and Ha state are different. The methodology of this verification is shown in Fig. 5-5. However, it was not possible to be carried out because the actual case of measuring conoscopic image takes several minutes, while the lifetime of Hs state is of less than 200 ms. To overcome this issue, we propose to use a stroboscopic illumination along with the conventional conoscope for verifying this transient LC profile.

To observe the conoscopic images of each state during the Hs state collapsing, the device is driven by a burst waveform for Hs state formation and a continuous waveform for Ha state formation. As shown in Fig. 5-6, the burst driving waveform is composed of two parts: an operating time and a delay time. The operating time is determined by the need to switch the device into the Hs state but avoid breaking down into the Ha state(s) (or transitioning into the bend state). The delay time allows recovery of the ground splay state. In this case, the operating time is set as 10 ms, and the delay time is set as 90 ms; meanwhile, the stroboscopic LED illumination is set to delay from the start of the switching signal by 5 ms (to allow the formation of Hs state), then to illuminate for 5 ms and be off for 90 ms (to synchronize with the device switching signal). This synchronized driving scheme ensures that only the Hs state is

captured by the conoscope. To further check the results, the conoscopic images are obtained with two different wavelengths of light source (a blue LED with the wavelength of 436-486 nm and a red LED with the wavelength of 622-654 nm).

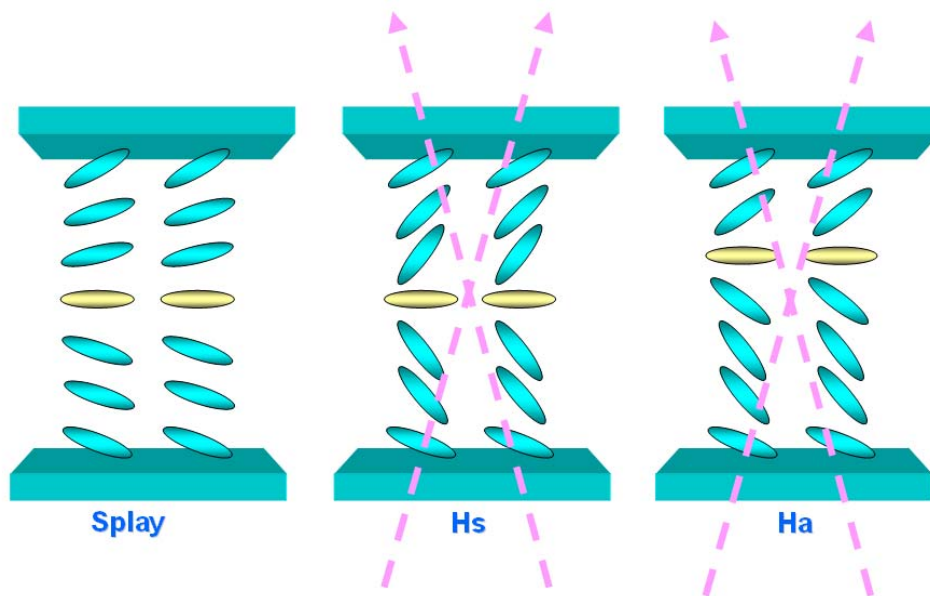


Fig. 5-4 LC director profiles of splay, Hs, and Ha states in a pi-cell.

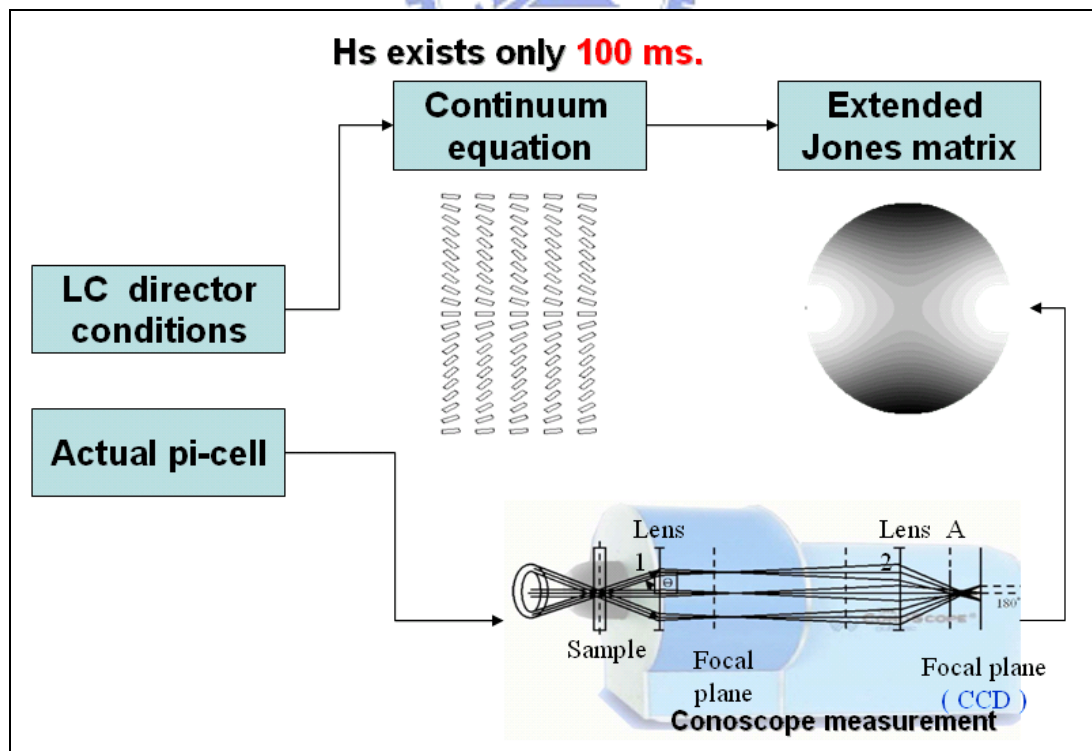


Fig. 5-5 The methodology of measuring the LC director profiles of splay, Hs, and Ha states in a pi-cell.

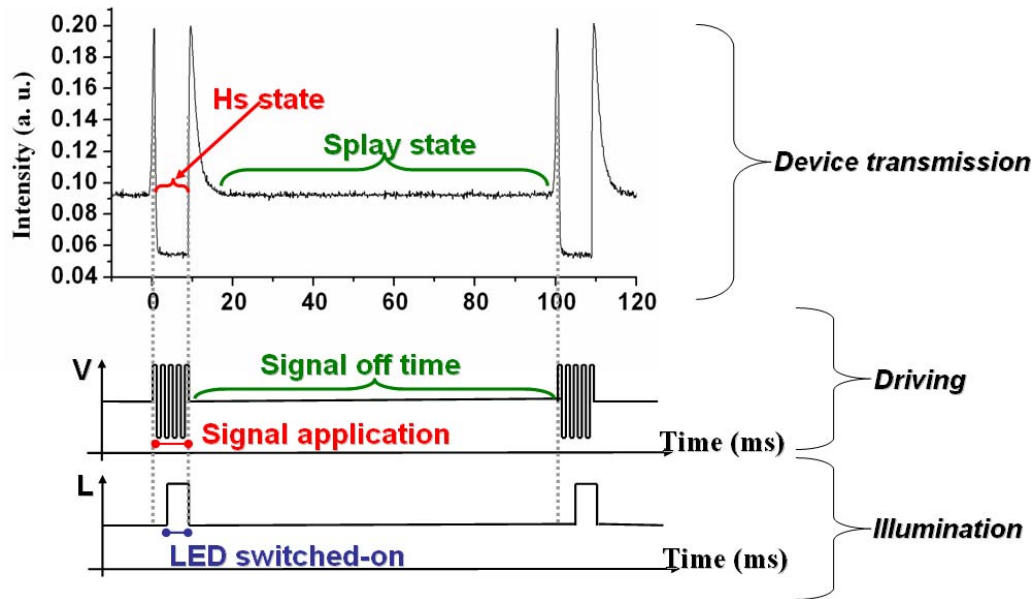


Fig. 5-6 Burst driving waveform for the device and illuminating LED.

5.2.4 Simulation on transient symmetric H state

Based on the Frank-Oseen continuum theory as discussed in chapter 2 [78, 79], the equilibrium director profiles in the LC cell can be calculated. Using typical LC material parameters (those for E7) and initializing from a ground splay state with a slight asymmetry (to allow eventual formation of the Ha state), we can obtain the director profiles of each state as shown in Fig. 5-7. After calculating the director profiles, an extended Jones matrix technique [80] can be used to determine the conoscopic images of each state for wavelengths corresponding to using blue and red LEDs as the light sources (examples of which are shown in Fig. 5-8).

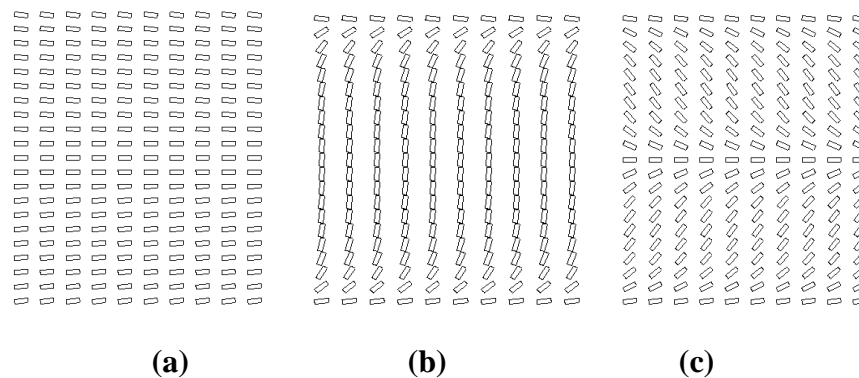


Fig. 5-7 The director configurations of (a) splay, (b) Ha, and (c) Hs states.

5.2.5 Results of the investigation on symmetric H state

The conoscopic measurement results within a viewing cone of around 30° show directly the symmetry of ground splay and transient Hs states, and also the asymmetry of the Ha state. In addition, the modeling based on the theory outlined above is used to determine the conoscopic images within the viewing cone of around 30° . The experimental and theoretical results are shown in Fig. 5-8, the measured conoscopic images (a)~(f) are in good agreement with the modeling results (g)~(l) (at least for the restricted viewing cone of around 30° – it is difficult to obtain good agreement over very wide viewing cone angles due to the illumination system used). The asymmetry in the Hs state is evident in both the experimental results (Fig. 5-8 images (c) and (d)) and the modeled images (Figs. 5-8 (i) and (j)). The symmetry of the ground splay state is as expected (Figs. 5-8 (a), (b), (g) and (h)). More important for this work is the symmetry evidence in Figs. 5-8 (e) and (f) (experimental) and (k) and (l) (theoretical). The good agreement between these data is the evidence that the director profile of the Hs state is indeed as expected, with decoupling of the director in the two halves of the cell. Moreover, according to our modeling, if the center point (zero-tilt) of the director structure is off center by 5% of the thickness of the device, then the conoscopic image is off axis by 15° . Thus, we can be confident that the method used here is very sensitive to asymmetry in the structure.

We have confirmed the existence of the symmetric profile of the LC director in the Hs state by stroboscopic conoscopic imaging. Along with the modeling, the transient non-switching director in the center of the device and the consequent de-coupling of the directors in the two halves of the device have been verified to occur. These de-coupled directors divide the device into two half-thickness Fréedericksz layers which result in the fast-switching behavior.

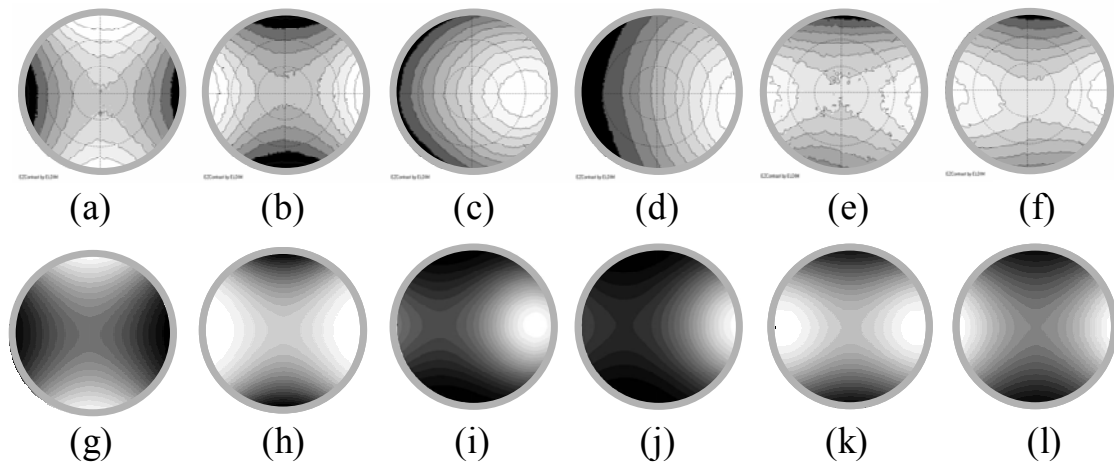


Fig. 5-8 Measured conoscopic images of device: (a) and (b) in splay state; (c) and (d) in Ha state; and (e) and (f) in Hs state. Simulated results: (g) and (h) in splay state; (i) and (j) in Ha state; and (k) and (l) in Hs state. The cases of (a), (c), (e), (g), (i) and (k) are illuminated/modeled with a blue LED, while the cases of (b), (d), (f), (h), (j) and (l) are illuminated/modeled with a red LED. (Each set of data has been normalized to optimize the image and exploit the image's full dynamic range.)

5.3 Design for extending the lifetime of symmetric H state

5.3.1 A proposed structure for fixing the central LC director of Hs state

With the stroboscopic illumination assisted conoscopy, we have verified the LC director profile of the Hs state. The central LC director drifting to one of the substrates results in the collapsing of Hs state. Based on this observation, it is possible to extend the lifetime of Hs state if we can fix the central LC director.

According to the report [81], the LC director tends to follow the polymerized structure in the LC cell. Therefore, if we can form the structure to sustain the Hs state, then its lifetime can be extended. Referring to the method that we used in chapter 4, if we use the synchronized polymerization along with photo-mask, then we will be able to form the structure as shown in Fig. 5-9, which thus fixes the central LC director and further extends the lifetime of Hs state.

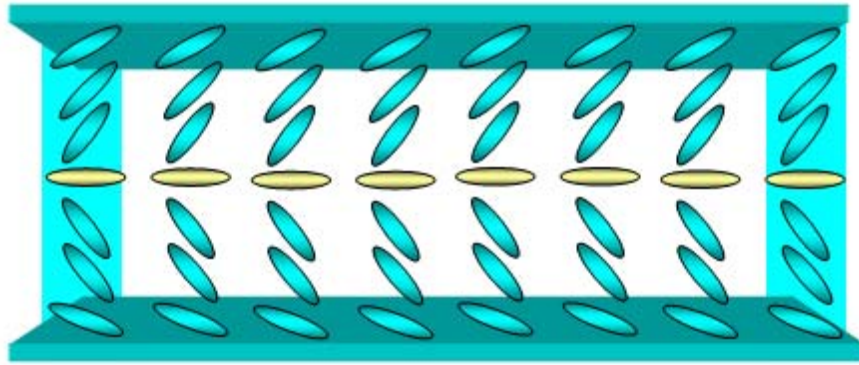


Fig. 5-9 Concept of Hs lifetime extension by polymer stabilization.

5.3.2 Simulation on the lifetime of proposed device structure

Before going for the execution of polymerization, we have also done some preliminary simulations to find out the best parameters for the shape of polymer wall. The simulation of polymer wall can be simplified by using a boundary condition. This concept is shown in Fig. 5-10, where the top and bottom substrates are set as strong anchoring with pretilt of $+2^\circ$ and -2° . Besides, the polymer walls in the middle of the cell are also set as strong anchoring with pretilt of 90° (perpendicular to the polymer wall). In this simulation, the pixel size (length A), cell gap (length B), and with or without polymer walls are altered to figure out the relation between the lifetime of Hs state and these factors.

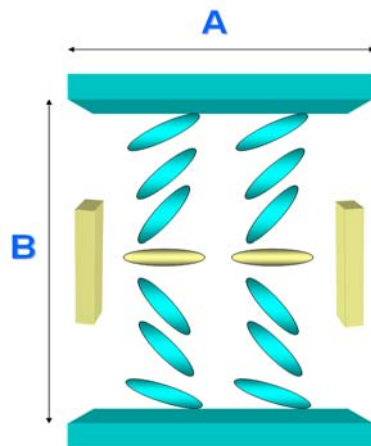


Fig. 5-10 Structure used for simulating the Hs lifetime extension.

The simulation results show the possibility of realizing the Hs state lifetime extension. Initially, the LC director profile is set as splay state as shown in Fig. 5-11 (a). During the following 10 ms, the LC director profile is then gradually shaping into the Hs state as shown in Fig. 5-11 (b). After the Hs state formed, the LC directors then collapse via two paths: one is via twist motion as shown in Fig. 5-12 (a); the other is via central director drifting as shown in Fig. 5-12 (b). To model the actual pi cell as a reference case, a 20 μm pixel size and 4 μm cell gap without polymer wall is simulated, and the electric field is set as 1.25 V/ μm . This referenced case collapses into twist motion within 40 ms and its central directors are drifted to the substrate within 150 ms.

Moreover, we model several cases of the LC cell, and the results are listed in table 5-1. The factors of pixel size, cell gap, with or without polymer wall, and the applied electric field are varied. These cases have indicated some interesting results: Cases A and B show that the pixel larger than 10 μm has no difference. Cases D and E show that the polymer wall effect is very significant on extending the lifetime of Hs state. Cases E, F, and G along with cases J and K show the cell gap effect on the lifetime. Cases H and I show the effect of applied field. Cases C and E show the effect of pixel size.

In the case of 9 μm pixel size, 4 μm cell gap, 1.25 V/ μm electric field, and with strong anchoring polymer wall, the director profile is sustained in the state of Hs even after 2000 ms as shown in Fig. 5-13. Thus we can say that the lifetime is extended to more than 2000 ms (larger than the referenced case by a factor of more than 10), which means our actual cell with lifetime of 100 ms will be possible to extend its lifetime to 1sec (it is long enough for display applications).

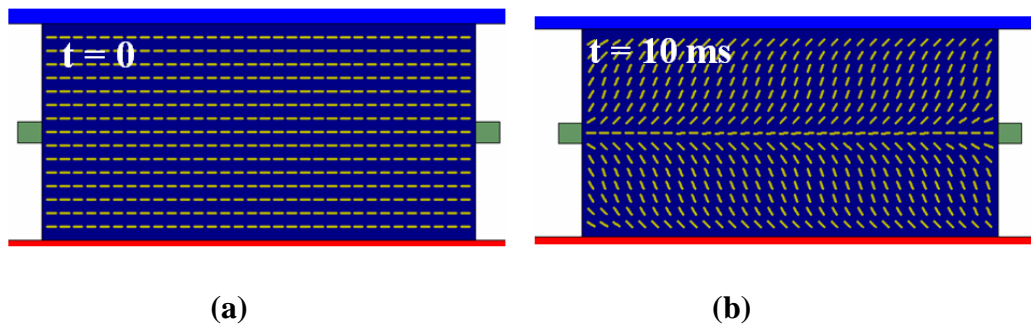


Fig. 5-11 Initial stage of simulation setup, where (a) represents the splay state at $t=0$ and (b) represents the Hs state at $t=10 \text{ ms}$.

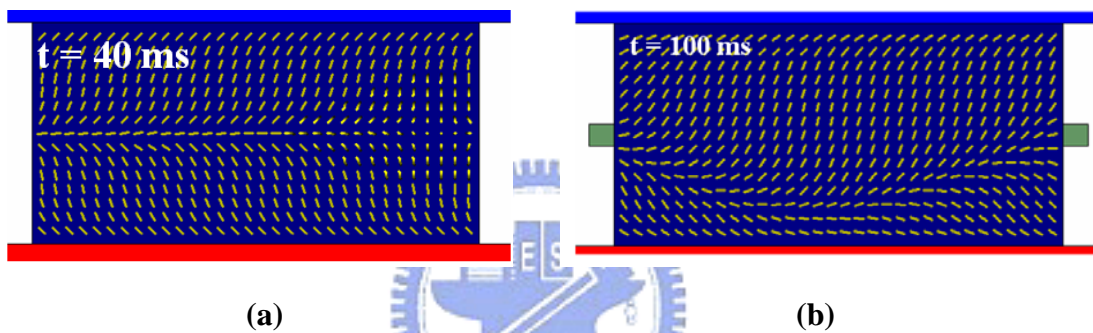


Fig. 5-12 Two cases of Hs state collapsing via (a) twist and (b) Ha state formations.

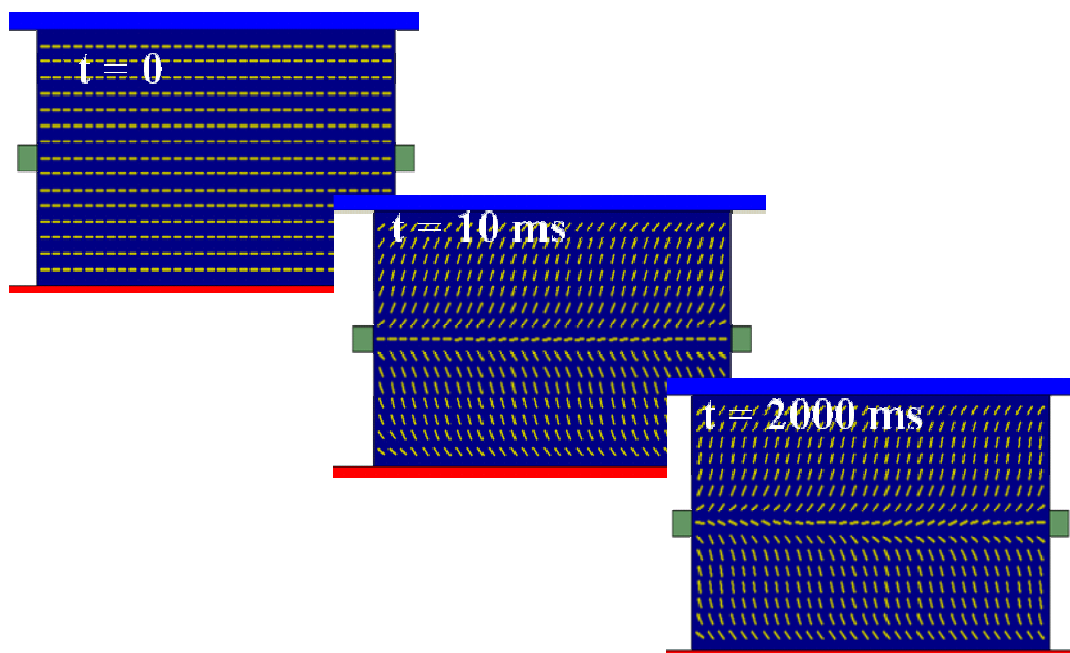


Fig. 5-13 LC director profile after 2000 ms in the best case of Hs state lifetime.

Table 5-1 Simulation results of Hs state lifetime extension with polymer wall.

	Pixel size (μm)	Cell gap (μm)	polymer wall	Vertical field (V/ μm)	Hs→Ha (ms)
A	20	4	Without	1.25	150
B	10	4	Without	1.25	150
C	10	4	With	1.25	140
D	9	4	Without	1.25	100
E	9	4	With	1.25	>2000
F	9	5	With	1.25	>500
G	9	3	With	1.25	45
H	9	4	With	1	100
I	9	4	With	0.75	60
J	10	4	With	1.5	>1000
K	10	5	With	1	300

5.3.3 Polymer-stabilization without incorporating a photomask

The concept of the synchronized system is that the mesogen in a pi-cell is only exposed under UV light at the Hs state. Thus, the polymer network will be formed to maintain the transient configuration of Hs state; this means that the Hs state is less likely to collapse into the Ha state, as a result, the lifetime of Hs state will be extended. This idea can be carried out by inserting a chopper between the UV light source and the pi-cell. When the UV light pass through the chopper, a photo-detector is used to detect the UV light and trigger the pi-cell to be turned on to the Hs state, by which the optical signal coming from UV light and the voltage signal applied to pi-cell will be synchronized, as shown in Fig. 5-14, which has been reported to be able to stabilize the non-permanent states [82].

The oscilloscopic image is captured to explain the idea of synchronized polymerization. As shown in Fig. 5-15, curve 2 is the UV light signal detected by a photo-detector used to trigger the pi-cell. Curve 1 is the light signal from the pi-cell,

and the driving waveform on this pi-cell is set to be $4 V_{rms}$ sine-wave operating for a period of 50 ms and then rest for a period of 200 ms to ensure that only Hs state is formed during the operation time. Then, another photo-detector is used to monitor the UV light signal (signal 3) to ensure only Hs state is formed under the UV light exposure. From this data, we can be confident of the accuracy of synchronized polymerization where the pi-cell is only exposed under UV light at the Hs state.

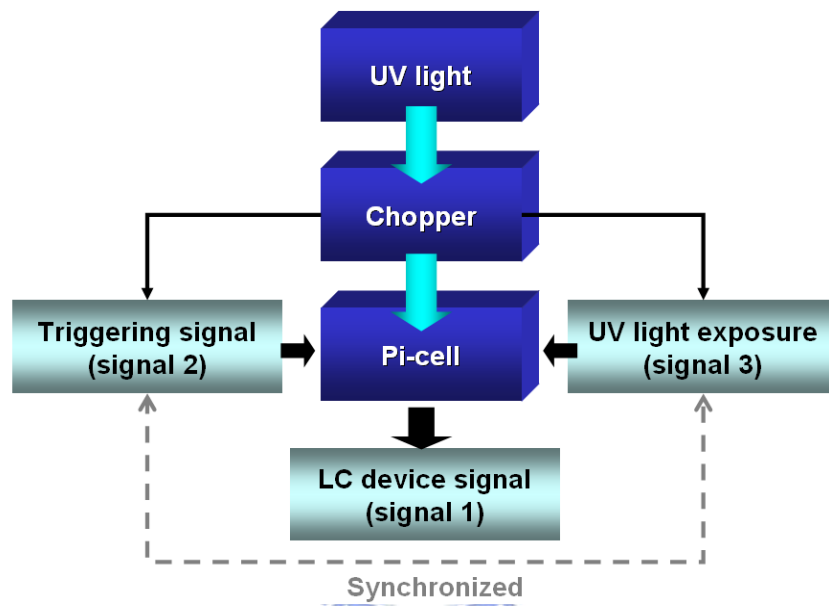


Fig. 5-14 Concept of synchronized polymerization.

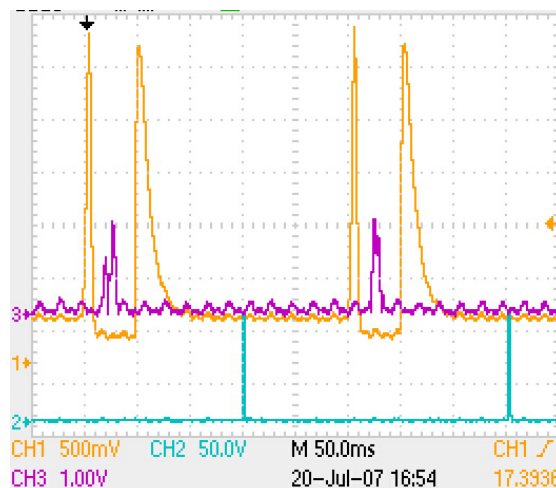


Fig. 5-15 Oscilloscopic image of synchronized signals, where curve 1 represents the optical signal of LC device, curve 2, triggering signal, and curve 3, monitored UV light signal.

We have tried several testing runs of different conditions for extending the lifetime of Hs state in a pi-cell. The results are summarized in table 5-2. We find that while using UV absorbing LC material such as E7, owing to the non-symmetric exposure of two sides of the pi-cell device, it is likely to form an only one Ha state pi-cell after polymerization, whereas in the case of non-UV-absorbing LC material such as ML1001, the device is very likely to form 2 Ha states with spatially homogeneous distribution.

Varying concentration does not bring any systematical results. In the case of 0.5 wt%, the device before being exposed under UV light get slight lifetime extension of Hs state which may result from the change of elastic properties. As for the case of 2.8 wt%, the state is stabilized in the Ha state within 2 minutes. While in the case of 1.5 wt%, we record the variation during the polymerization and found that the intensity is suppressed gradually as shown in Fig. 5-16. This verifies that the LC directors near the substrates are stabilized; however, the lifetime of Hs is still shortened and the optical contrast is lowered. In the end, as shown in Fig. 5-17, the phase-suppressed pi-cell turn out to be very low contrast but very fast switching. The switching time in this case is of less than 1 millisecond; however, owing to its low phase retardation, this device is not suitable for display application, unless thicker cell-gap will be used instead.

Table 5-2 Summary of conditions and results of tested pi-cell.

Condition	Result
UV absorbing LC	One Ha state
Non-UV absorbing LC	Two Ha states (homogeneously distributed)
0.5 wt%	Hs sometimes got extended lifetime
2.8 wt%	Stabilized in Ha within 2 min
1.5 wt%	Hs lifetime degraded (Hs still exists)
Staled LC/mesogen mixture	Suppressed Ha (though very fast switching)

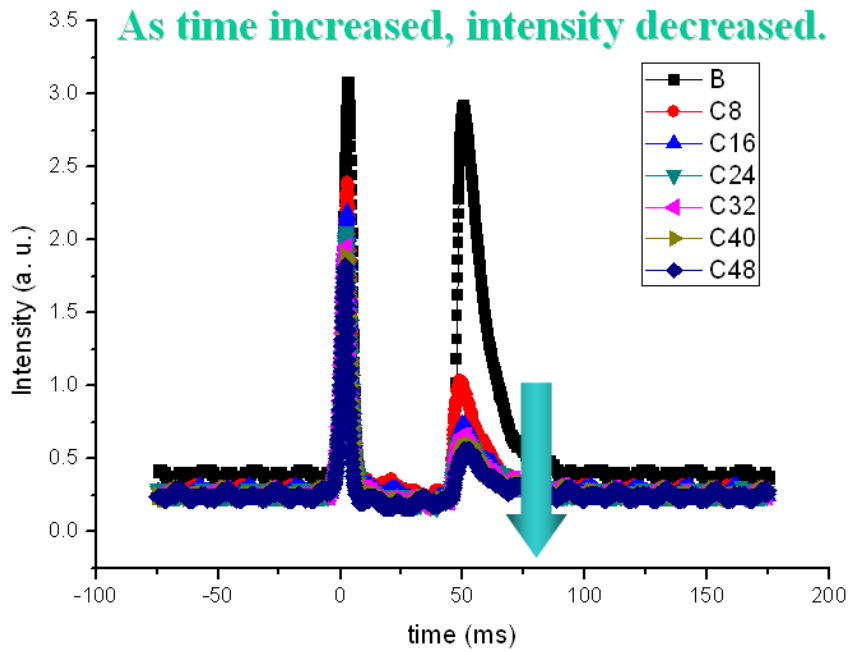


Fig. 5-16 Oscilloscopic image of the dynamics during the synchronized polymerization on the Hs state.

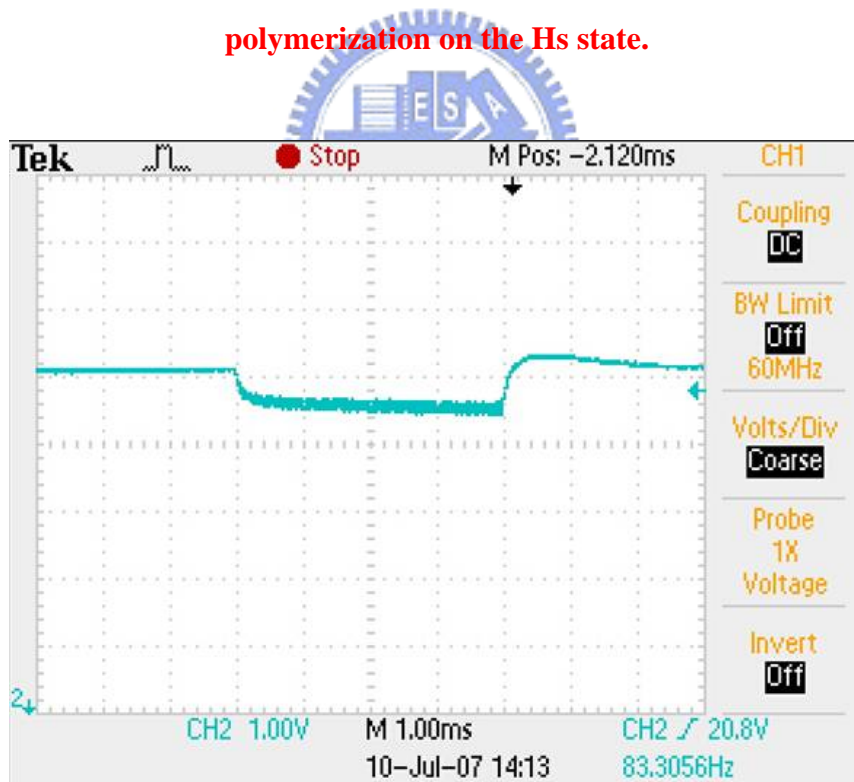


Fig. 5-17 Oscilloscopic image of phase-suppressed pi-cell.

After doing several careful experiments on the “synchronized polymerization,” we finally realized that the idea for extending the lifetime of symmetric H state is not

easy though we thought it was simple. We have tried using different LC materials such as E7 (an UV-absorbing material) and ML1001 (a non-UV-absorbing material), but each of them can not show the lifetime extension after accurate exposure during symmetric H state. The possible reasons that we can not get lifetime extension are: first, the mixture of mesogen and LC material is not thoroughly mixed on the scale of molecular level; second, the central LC (zero-tilt) directors are very sensitive to the deviation from symmetry and tended to collapse into asymmetry; third, it is impossible to form a symmetric polymer structure on both sides of the cell artificially. To resolve this issue, adopting a photo-mask to form the wall structure instead of the whole-area-polymerization may be a plausible method.

5.3.4 Photomask assisted polymer-stabilization

Executing synchronized polymerization with a photo-mask may be able to prevent the phase suppression issue. Because only part of the region is polymerized, other region can still be operated freely after polymerization; meanwhile, this un-polymerized region still can be affected by the polymerized region, which means the central LC director in this region still tends to follow that in the polymerized area.

The sample is prepared as follows: a typical pi-cell is prepared by stacking two parallel rubbed substrates with cell gap of $5.5 \mu\text{m}$, filled with LC material, E7, and mixed with 3% mesogen (RM257, blended with 10% photo-initiator, Irgacure 907). The polymer wall is then formed by exposing the pi-cell to a UV-LED, 30 mW, shadowed by a photo-mask.

The polymerization setup is arranged by imaging a photo-mask onto the LC pi-cell. As shown in Fig. 5-18, UV light is illuminated from the UV-LED, passing through the photo-mask, converged by objective 1 onto the pi-cell to form the specific pattern of the polymer wall. To ensure the image is formed in the LC layer accurately, a charge

coupled device (CCD) is used to focus the spacers in the pi-cell with the aid of objective 2. As long as the images of spacers and the pattern of the photo-mask coincidentally focused on CCD, the shape of the polymer wall can be well-defined as the pattern of the photo-mask.

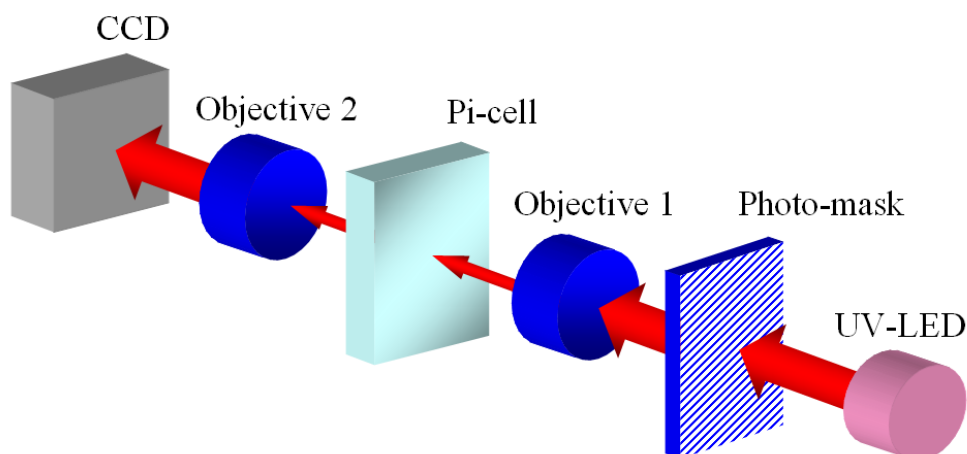


Fig. 5-18 The optical setup of polymerization with a photo-mask.

The simulation results indicate that the case with pixel size of $9 \mu\text{m}$ and cell gap of $4 \mu\text{m}$ shows the best condition of lifetime extension; therefore, to make a high accuracy polymerizing pattern is demanding. The current results that we have achieved are shown in Fig. 5-19. The picture is taken with placing the rubbing direction of the pi-cell parallel at 45° to one of the crossed polarizers. The black area is stabilized in the bend state, whereas the purple region represents the twist state. The finest pattern can be around $10 \mu\text{m}$ and pixel size can be around $70 \mu\text{m}$. Although it is the best case we can have at present, it is not enough for stabilizing the Hs state according to our simulation result. However, this technique is still suitable for investigating the flow effect on the Hs stabilization, which also affects the synchronized polymerization significantly.

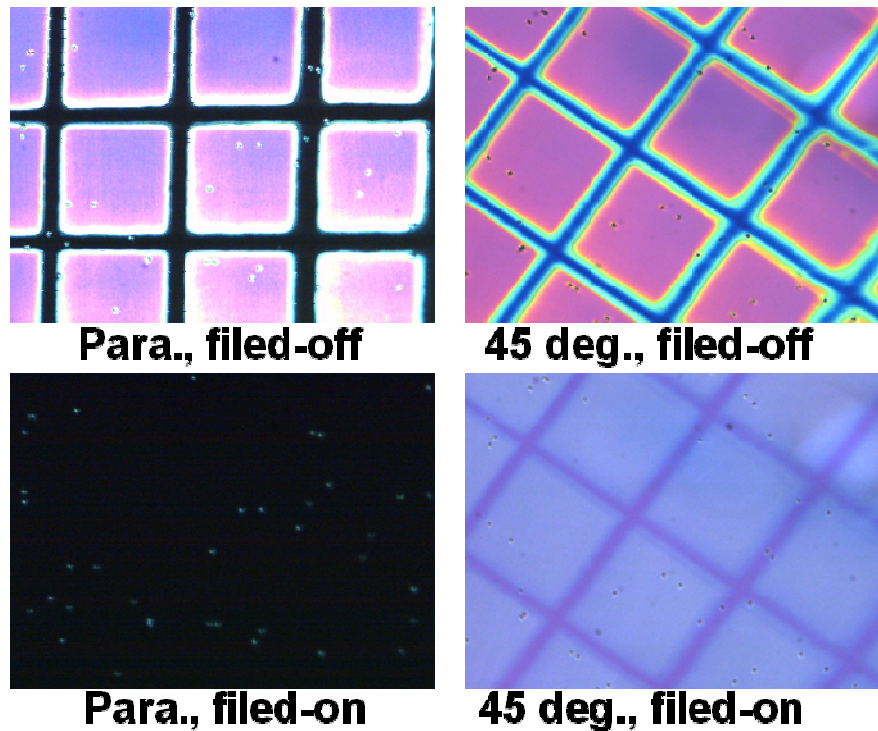


Fig. 5-19 Optical microscopic images of polymerized pi-cell with photomask.

To vary the flow conditions for investigating the different kinds of effect on the polymerization, two kinds of driving schemes (without applied voltage and burst driving) are used during the UV light exposure. Additionally, the orientation of the photo-mask is also varied as parallel or perpendicular to the rubbing direction. These orientations determine the trend of flow along or against the polymer wall. The flow conditions are summarized in Table 5-3.

Table 5-3 The different flow conditions of the pi-cell.

	PW orientation to the rubbing direction	Driving scheme	Flow direction to PW
Sample 1	Along	No applied voltage	No flow
Sample 2	Against	No applied voltage	No flow
Sample 3	Along	Burst	Along
Sample 4	Against	Burst	Against

The pi-cells whose polymer walls are parallel to the flow trend (or without flow) have well-defined shape corresponding to the photo-mask; whereas the one (sample 4) against the flow trend cannot stabilize the LC state properly. This result can be clearly seen from Fig. 5-20. The Figs. 5-20 (a), (c), (e), and (g) represent the off-state of the samples of 1, 2, 3, and 4, respectively. The Figs. 5-20 (b), (d), (f), and (h) represent the on-state ($3.5V_{\text{rms}}$ continuous sine wave) of samples 1, 2, 3, and 4, respectively. The rubbing direction of these pi-cells is 45° from right-top side to left-bottom side. In the cases of samples 1-3, the polymer walls can clearly be seen, whereas sample 4 has no clear shape of polymer wall. After applying 3.5V sine wave to the samples, the texture of Ha is formed, and its orientation is parallel to the rubbing direction. Note that the polymer wall of sample 4 now can be seen, but the polymer wall has no strong anchoring force to stabilize the state, which makes the domain of Ha cross the polymer wall. This result indicates the polymer wall cured against the flow cannot form solid wall structure.

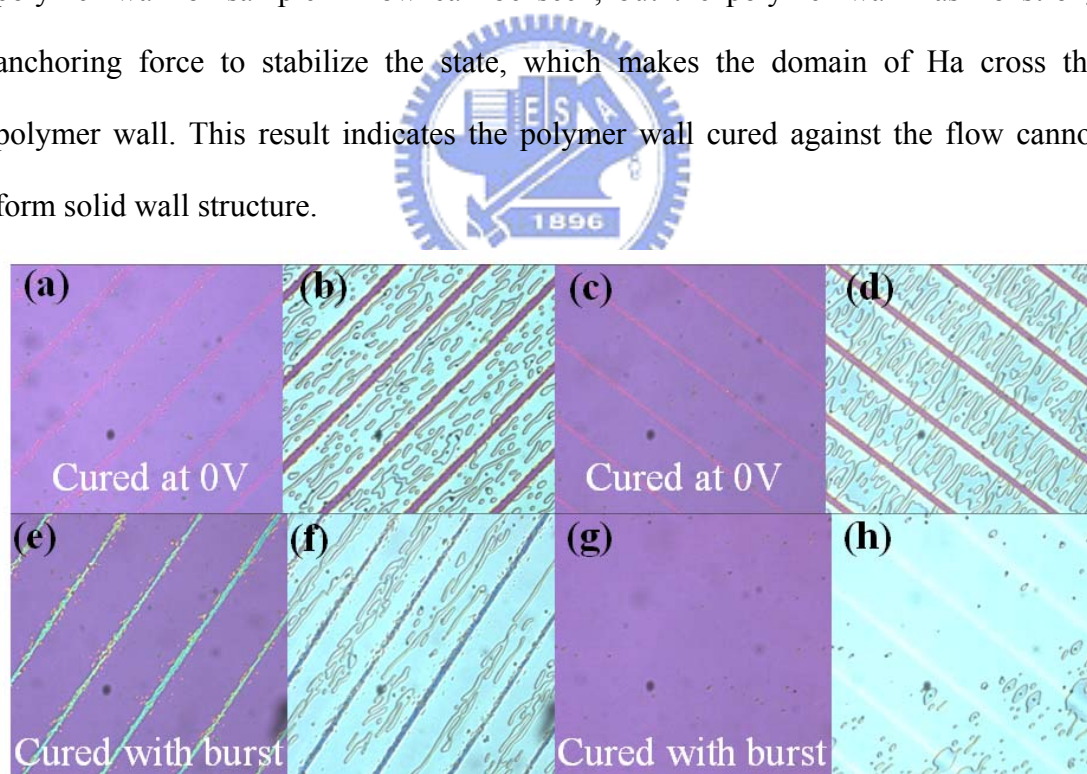


Fig. 5-20 The microscopic images of four different flow conditions. (a), (c), (e), and (g) represent the off-state of the samples of 1, 2, 3, and 4, respectively. (b), (d), (f), and (h) represent the on-state ($3.5V_{\text{rms}}$ continuous sine wave) of the samples of 1, 2, 3, and 4, respectively.

To demonstrate the effect of polymer wall collapsing, we prime the pi cells to the bend state (Fig. 5-21 (a)) and relaxing them back to the splay state (Fig. 5-21 (b)). The polymer wall in this case shows the disability of stabilizing the state properly, since the polymer wall region should be stabilized in the splay state with well-defined shape. Another example of the pi cell under the same curing condition is observed as Figs. 5-21 (c) (primed in the bend state) and Fig. 5-21 (d) (relaxing from the bend state to the twist and splay states). Owing to the collapsing of the polymer wall, the splay state is stabilized out of the area of polymer wall. On the contrary, the device with the curing condition of sample 3 still have well-defined shape of polymer wall, as shown in Figs. 5-22 (a) (primed in the bend state) and 5-22 (b) (relaxing to the splay and the twist states).

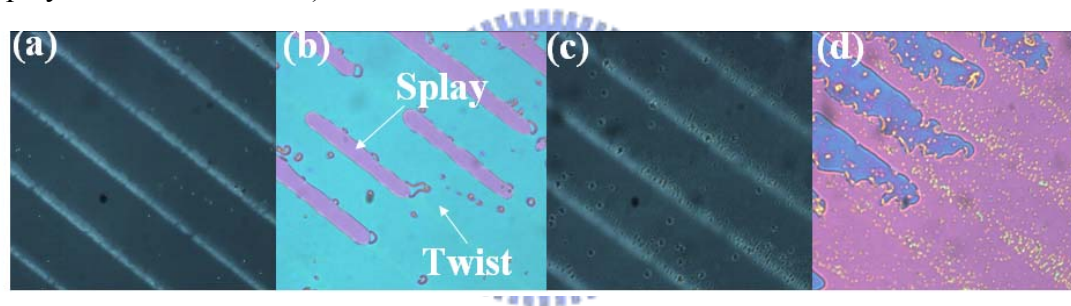


Fig. 5-21 The microscopic images of the pi-cells. The polymer walls are against the flow during the polymerization (sample 4), where (a) and (c) are in the off-state, (b) and (d) are in the on-state.

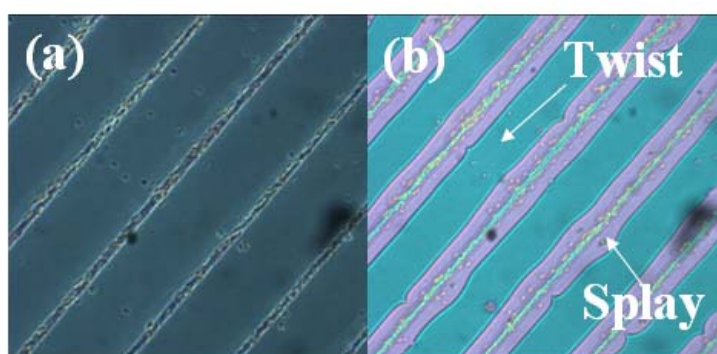


Fig. 5-22 The microscopic images of the pi-cells whose polymer walls are along the flow during the polymerization (sample 3), where (a) is in the off-state, (b) is in the on-state.

We have proven that the flow induced by burst driving in an LC cell can affect the formation of the polymer wall. The rubbing direction in a pi-cell can be used to represent the flow direction, and the orientation of the photo-mask can be used to determine the orientation of the polymer wall. By varying the orientation of the photo-mask and the rubbing direction, we have demonstrated that the flow is capable of collapsing the polymer wall when its trend is against the wall orientation. These flow effects thus influence the stabilization of the Hs state.

5.4 Summary

In this chapter, we have reported to you a stroboscopic illumination method for capturing the transient profile in an LC cell. This powerful technique opens a new era for scientists to investigate the non-permanent states which could be only simulated. In addition, a transient state in a pi-cell, symmetric H state, has been verified to have a symmetric LC profile. According to this fact, we have designed and simulated a polymeric structure to sustain the central LC director, which has been proven by simulation to have a lifetime enhancement by a factor of 10. On the other hand, to realize the proposed polymer structure, we set up a lens system to project the pattern of photomask onto the pi-cell to form the desired structure. However, the current result shows that the spacing between the polymer walls is too large and the flow effect tends to collapse the wall structure.

Chapter 6

Embedding the OLED backlight into an LC cell

6.1 Introduction

A transfective LCD which takes both advantages of the transmissive and reflective LCDs (T- and R-LCDs) has been well-adopted in the mobile display applications. Under the sunlight ambience, the transfective LCD is operated in the reflective mode. In this mode, the device exploits the ambient light as the light source to increase the contrast ratio and save the power consumption. While in the dark or dim ambience, the transfective LCD is operated in the transmissive mode, utilizing the backlight as the light source. According to the operational principle, the conventional transfective LCD needs a backlight, which thus hinders the further reduction of form factor.

Embedding an OLED device into an LCD device to function as the backlight module is a plausible method to further reduce the form factor of a transfective LCD. The combination of an OLED and an R-LCD was first proposed by E. Lueder in 2000 [83]. Afterwards, the hybrid device structures [84-88], the pixel and the driving circuit design [89], and the optical performance [90] were reported. These proposed stacked devices, as shown in Fig. 6-1 (b), can exhibit high-quality image at most of the light ambiences. Furthermore, the stacked devices have much lighter weight, smaller form factor, and higher aperture ratio compared with those of the conventional transfective LCDs. However, the OLED and the R-LCD were stacked rather than integrated, which made the air gap come into being. The air gap reduced the contrast ratio of the OLED and the R-LCD. To further resolve this issue, we propose to integrate the

OLED and the R-LCD in a sequential process (i.e. directly building an LC cell on the OLED).

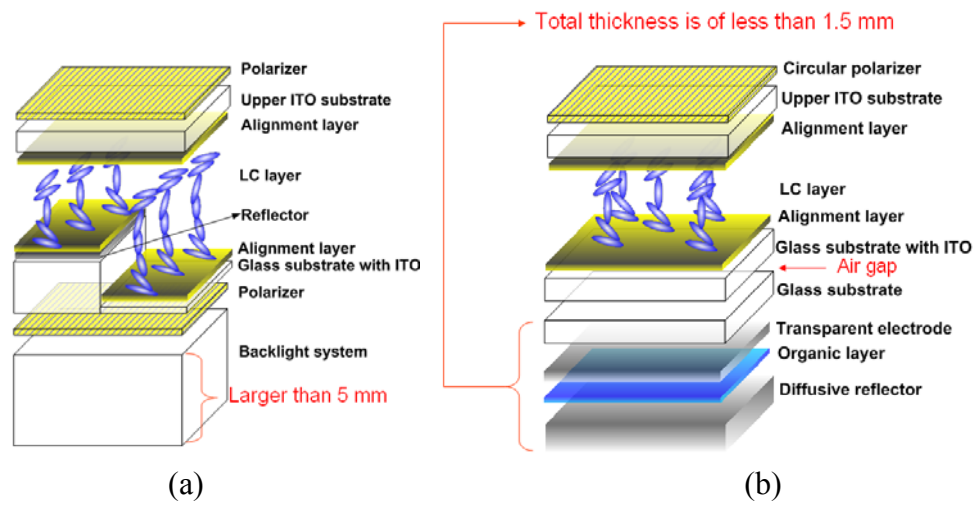


Fig. 6-1 The configurations of (a) conventional transfective and (b) stacked OLED/LCD displays.

This proposed structure can not only decrease the form factor of an LCD but also increase the fabrication yield of an OLED. As shown in Fig. 6-2 (a), originally the OLED was regarded as a display. In this case, if there are some defects in the panel, this panel is not qualified for sale. However, as long as the OLED is used as a regionally dimming backlight, the small defects can be averaged by adjacent areas (Fig. 6-2(b)).

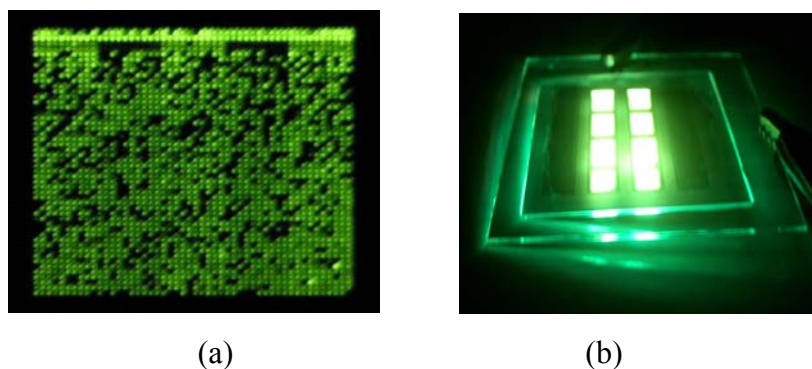


Fig. 6-2 OLED devices with (a) high and (b) low resolutions.

This thesis neologizes the integrated structure as an “emi-flective” display because the device is composed of the “emissive” OLED and the “reflective” R-LCD, which follows the example of transflective display with the combination of the transmissive and the reflective LCDs. However, the emi-flective LCD further adopts the flashing backlight concept, which means the OLED can be regionally turned on and off to complete the darkness for increasing the contrast ratio and lowering the power consumption simultaneously.

6.2 Design and operational principles of emi-flective LCD

6.2.1 Device and fabrication designs

The proposed emi-flective display configuration comprises a reflective electrode, the organic layers, a transparent electrode, a thin-film encapsulation (TFE) layer, a lower electrode of LCD, a lower alignment layer, an LC layer, an upper alignment layer, an upper electrode of the LCD on the top glass, and a circular polarizer, as shown in Fig. 6-3 (a). Note that the proposed emi-flective display device has only two substrates; besides, there is no air gap inside the cell. The fabrication process of the integrated device can be carried out by passivating the OLED with the TFE, and then depositing the ITO and polyimide on the TFE layer, followed by sandwiching the prepared top-substrate, and finally injecting LC.

To drive the R-LCD and OLED sections of the integrated display respectively, we designed an active matrix driving circuit, as shown in Fig. 6-3 (b) [6-3]. The TFT backplane is positioned at the lower substrate of OLED. The point A in Fig. 6-3 (b) is connected from the lower electrode of the LCD to the backplane through the pre-formed contact hole as shown in Fig. 6-4. As the switch (SW) is open, the circuit operates as a conventional LCD driving circuit; when SW is closed, the LCD is set to be “normally white state,” and the OLED is operated.

One of the major issues of integrating the OLED and R-LCD is the passivation of the OLED. In order to protect the OLED from the thermal damage during the fabrication, the polyimide shall be processed in low temperature ($<120^{\circ}\text{C}$). Besides, the OLED shall be well-protected from the intrusion of polyimide.

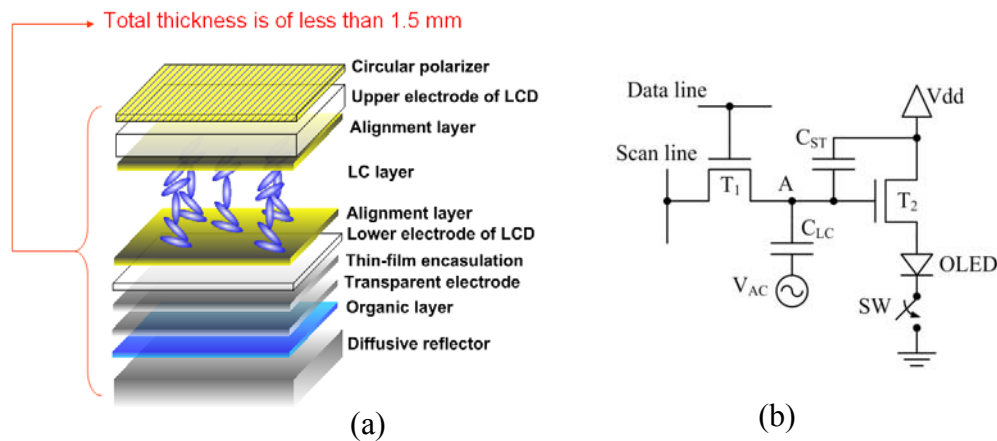


Fig. 6-3 (a) Configuration and (b) driving circuit of emi-flective LCD.

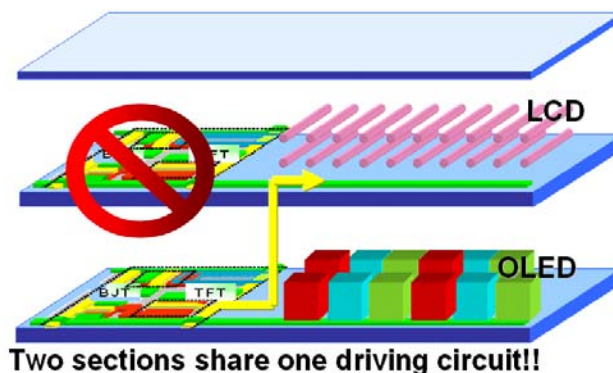


Fig. 6-4 Proposed stacking structure of OLED/LCD.

6.2.2 Preliminary test of optical performance

To make a preliminary test on the optical performance of the emi-flective display, we simplify the fabrication by replacing the proposed TFE with a glass lid passivation which can also provide an air-gap-free integrated device (the R-LCD and OLED share the central substrate, so there is no air-gap in the intermediate region).

To examine the optical performance with different arrangements of R-LCD and OLED, we make two kinds of three-glass emi-flective display device for experiments.

Since these devices are constructed without an intermediate air-gap, they possess better optical performance compared to the aforementioned prior works [83, 84]. As shown in Fig. 6-5, in structure 1, the OLED is placed below the R-LCD where the circular polarizer can be used not only for the LCD but also for the OLED as an ambient light blocker. As a result, under the light ambience of 30 nits, contrast ratio of the OLED is enhanced by a factor of 8. In structure 2, the OLED is configured above the R-LCD where the OLED is transparent and the R-LCD can further adopt the textured reflectors. In this case, we adopt the diffusive micro scattering reflector (DMSR) to enhance the contrast ratio (in reflective mode) to 100:1 at the viewing cone of 20° . Moreover, because the light emitted from the OLED is not affected by the R-LCD, the contrast ratio in emissive mode is further enhanced to 60000:1 (this fact is reasonable, since utilizing the regionally flashing backlight concept can largely increase the contrast ratio).

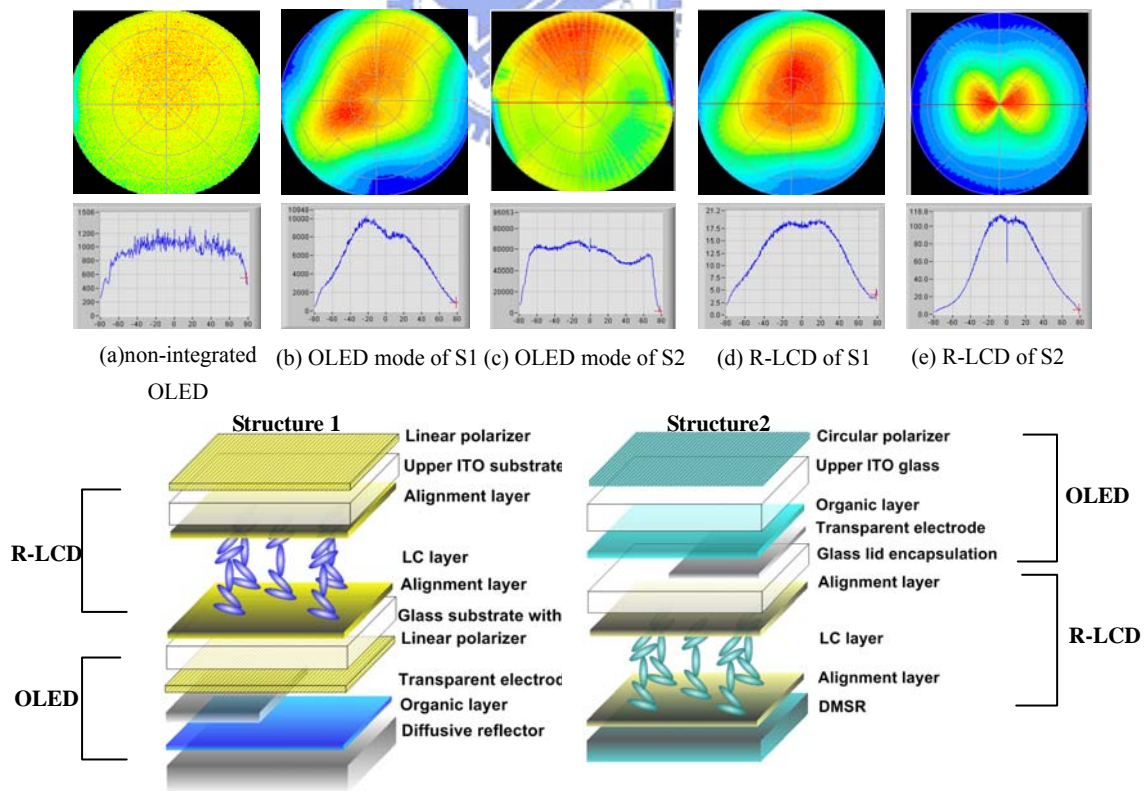


Fig. 6-5 Iso-contrast contours of two emi-flective LCD configurations.

6.3 Fabrication process for embedding the OLED into an LC cell

6.3.1 Low temperature process for LC alignment

The alignment process is generally executed under high temperature to activate the reaction for orienting the LC director. This high temperature process can damage the OLED section of the integrated device. As a result, we propose three kinds of method to prevent the OLED section from the suffering of high temperature process. The first one is to use nano-particles to align the LC director. Because of the surface energy from the nano-particle film, the LC director tends to align vertically without the assistance of high temperature process. The second method is to use alignment-free LC materials such as cholesteric LC or polymer dispersed LC. The third method is to use low temperature alignment material (baking temperature around 100°C) such as dimethyloctadecyl[3-(trimethoxysilyl)-propyl]ammonium chloride (DMOAP) or low temperature processed polyimide (provided by industrial technology and research institute, ITRI).



6.3.2 Thin film encapsulation for OLED device

A conventional OLED can be made by deposition of multi-layer structure. The deposition can be carried out by chemical vapor deposition (CVD) and physical vapor deposition (PVD). This kind of process is mainly for small molecular materials, and this kind of device is generally called OLED. While the process involving with spin coating, stamping, or ink-jet printing is suitable for polymeric materials, and this kind of device is called polymer light emitting diode (PLED). As mentioned in section 2-3, the multi-layer structure basically composes a cathode, an electron injection layer, an electron transporting layer, a recombination zone, a hole-transporting layer, a hole-injection layer, and an anode.

To increase the lifetime of OLED, the most vulnerable layer, cathode, is protected

with sealed glass lid which prevents the intrusion of oxygen and oxide. In addition to glass sealing, TFE has drawn much attention for its feasibility to integrate with a flexible OLED. As shown in Fig. 6-6, this TFE is composed of several buffering layers for protecting the mechanical damage and several silicon nitride/oxide stacking layers for preventing the penetration of oxide (total thickness is of less than $1 \mu\text{m}$). In this thesis, we adopt this technique to replace the intermediate glass lid [91-96].

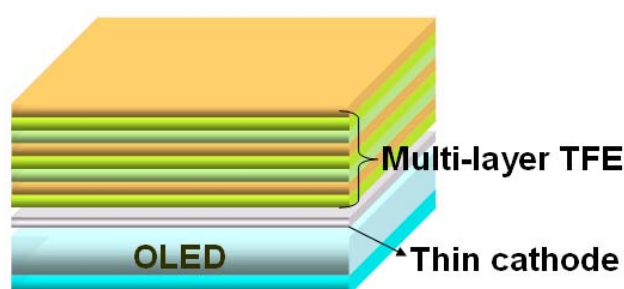


Fig. 6-6 Schematic diagram of TFE structure.

6.3.3 Directly building the LCD on the OLED

The emi-flective display device is carried out by building an LCD on the top-emission OLED. To prevent putting the OLEDs in the high temperature process, we use a low temperature alignment material for the LCD section. In addition, we choose the LC material as vertical aligned type, the hole injection material as CF_x , the hole transporting material as N,N' -bis-(1-naphthyl)- N,N' -diphenyl-1,1'-biphenl-4,4'-diamine (NPB), the emitting material as tris(8-hydroxyquinoline) aluminum complex (Alq_3), the electron injection material as LiF, and the transparent metal as aluminum. The OLED device structure is: ITO/NPB (20 nm)/ Alq_3 (150 nm)/LiF (1 nm)/Al (15 nm). As shown in Fig. 6-7: first, the ITO substrate is patterned and cleaned. Second, the organic material for OLED section is then deposited sequentially. Third, the TFE layer consisting of SiN_x /organics/ SiON is formed on the top of the OLED. Fourth, the ITO electrode for

the LCD section is then formed on the TFE layer. Fifth, the top substrate with photo-spacers is capped. Finally, the LC material is then injected into the device. This device integrates the OLED and LCD without intermediate glass lid.

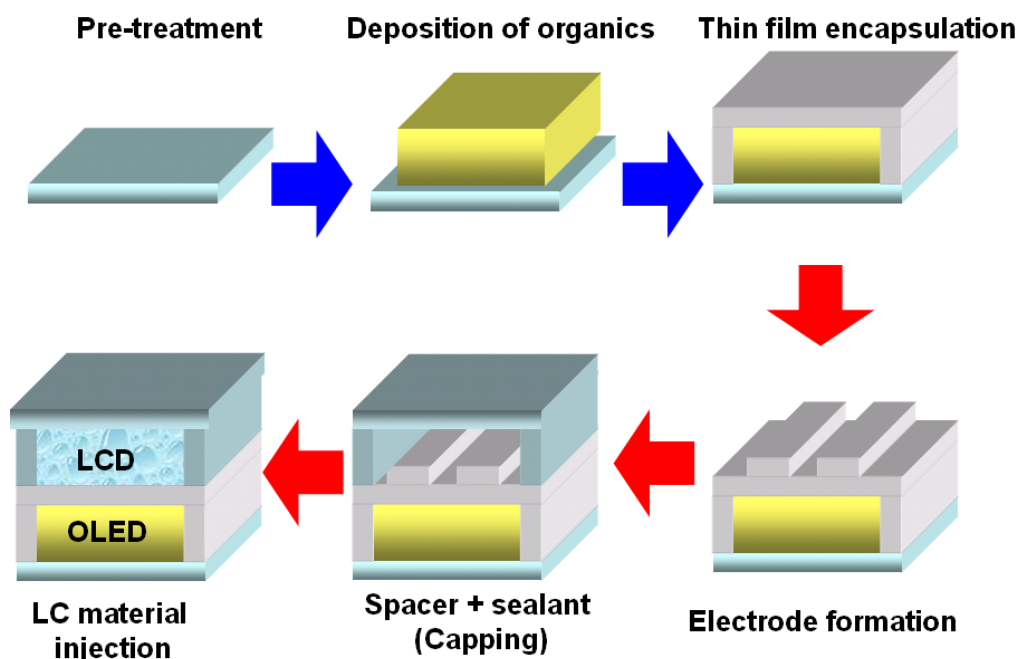


Fig. 6-7 Fabrication scheme of building LCD on an OLED device.

6.4 Results of integrated emi-flective LCD device

6.4.1 Lifetime of the integrated device

If there were no TFE on the OLED, the LCD process would deteriorate the fragile cathode of the OLED immediately. As a result, the TFE is a very critical process for increasing the lifetime of the OLED section. The SEM image of TFE is shown in Fig. 6-8 (a), with the protection of this TFE, the OLED after integration can still work with lifetime of 100 hr (the extrapolation is shown in Fig. 6-8 (b)). Two kinds of integration are made, one is to use non-aligned cholesteric LC (Fig. 6-9 (a)), and the other is to use DMOAP for VA mode LC (Fig. 6-9 (b)).

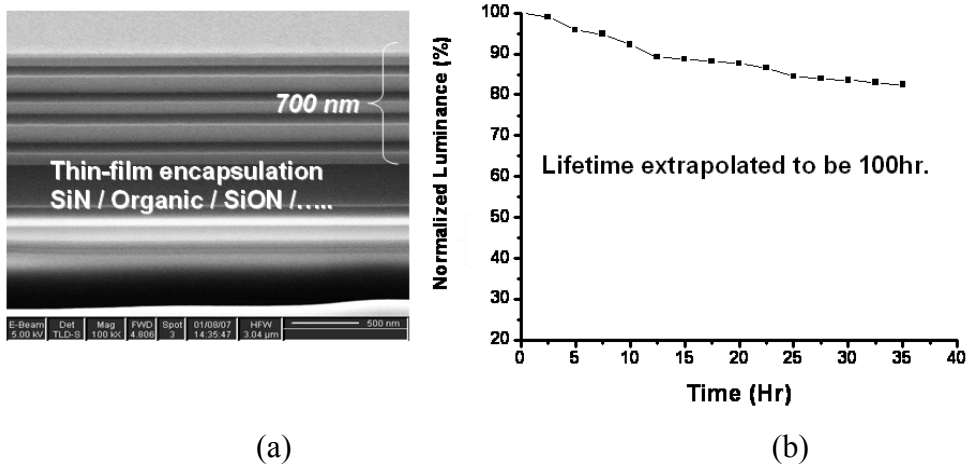


Fig. 6-8 (a) The SEM image of TFE and (b) the lifetime of OLED after integration.

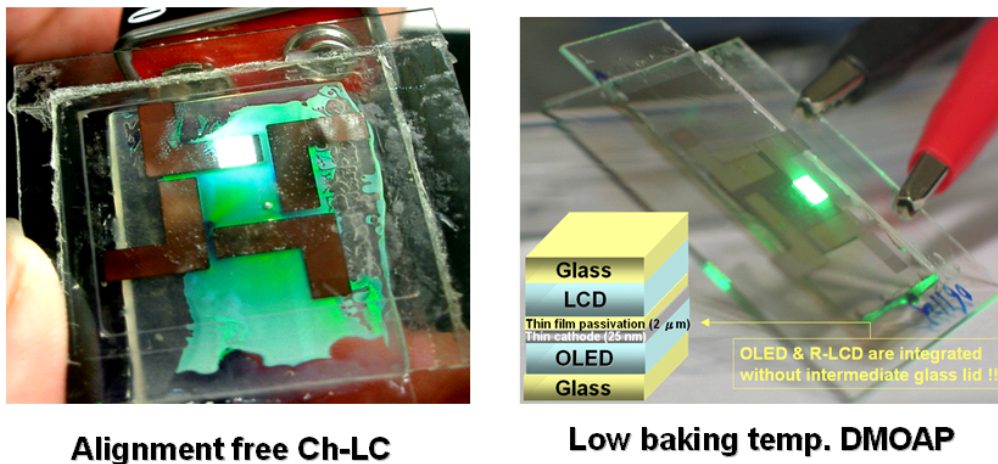


Fig. 6-9 Photographs of the functioning of integrated OLED and R-LCD.

6.4.2 Optical contrast of the emi-flective LCD

The optical performance of this integrated device is then measured with conoscope. As shown in Fig. 6-10, the OLED mode shows contrast ratio of 10000:1 in the normal direction, whereas the R-LCD mode shows only 6:1. Therefore, to increase the contrast ratio in R-LCD mode, we propose to use a VSL to increase the sunlight visibility, and also increase the light-out coupling efficiency of the OLED section simultaneously.

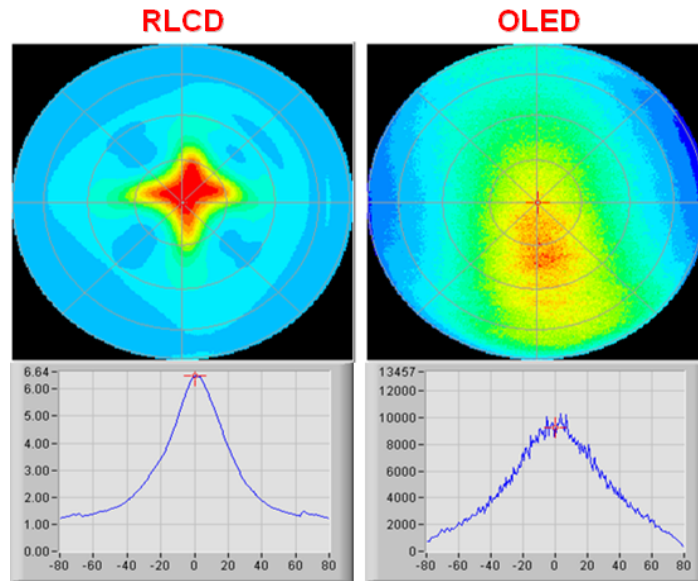


Fig. 6-10 Conoscopic images of the integrated device in OLED and R-LCD modes.

6.5 Optimization on the optical contrast in reflective mode

6.5.1 Contrast ratio enhancement with volumetric scattering layer

The VSL can simultaneously act as a scattering reflector for the R-LCD and a light extracting layer for the OLED. The operation of our proposed emi-reflective display is depicted in Fig. 6-11. In the bright ambience, the device is operated in the reflective mode as follows: the ambient light impinges on the LCD section, reflected by the cathode of the OLED section and then scattered by the particles. While in the dark ambience, the device is operated in emissive mode as follows: The light generated by the OLED section passes through a thin cathode, a passivation layer, a dielectric film (PMMA, $n=1.48$) and is thus scattered by the particles. In this structure, the VSL acts as a scattering center for the reflective mode to avoid the glare effect; besides, due to the compatibility between the refractive indices of the passivation layer and PMMA, it is also used to enhance the extraction efficiency of the OLED. Moreover, the scattering center also helps to eliminate the waveguide structure and the total internal

reflection of OLED, as shown in Fig. 6-12.

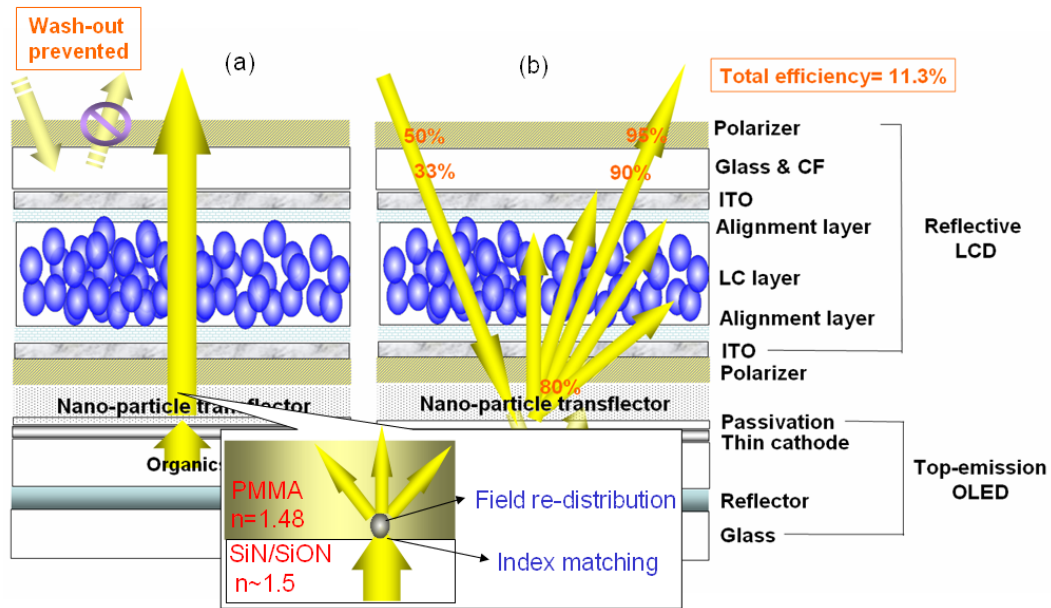


Fig. 6-11 Operational principle in (a) emissive and (b) reflective modes.

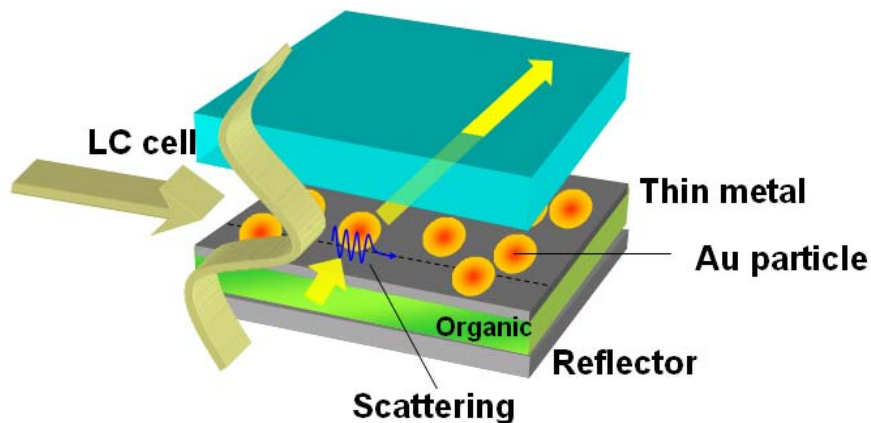


Fig. 6-12 Mechanism of light-out-coupling enhancement by VSL.

6.5.2 Simulation results

To optimize the condition of VSL, we simulate the parameters for sunlight visibility with a commercial simulator - LightTool™ whose algorithm is based on the ray optics along with the Fresnel equation. The VSL structure used for the simulation is shown in Fig. 6-13, which is comprised of a reflective illuminator, a VSL with varied conditions, and the outer ambience. In order to compare the optical

performance of VSL with a freestanding mirror and a Lambertian reflector, the simulation structure is further categorized into 3 cases. Moreover, to acquire the reflection profile, the light beam is projected at an incident angle of 30° and reflected to a semi-sphere detector.

To evaluate the RLCD image quality, a haze component enhancement is defined as equation (6-1) [96-98], where the benchmark is set as the intensity of the light reflected by Lambertian reflector (ideal diffusive reflector) at normal direction (90°).

$$\text{Haze component enhancement} = \frac{I_{\theta}}{I_{\text{Lambt},90^{\circ}}} \quad (6-1)$$

The haze component enhancement results from the shifting of the glare light to the other angles. This phenomenon can be explained by the simulation results shown in Fig. 6-14. The original glare light is too strong and concentrated to be observed by human eyes. While the glare light scattered by the VSL, the image can be observed at an angle of 10° away from the glare angle. Thus the haze component at this angle gets a significant enhancement which is even larger than the light reflected by Lambertian reflector at the normal direction by a factor of 2.5.

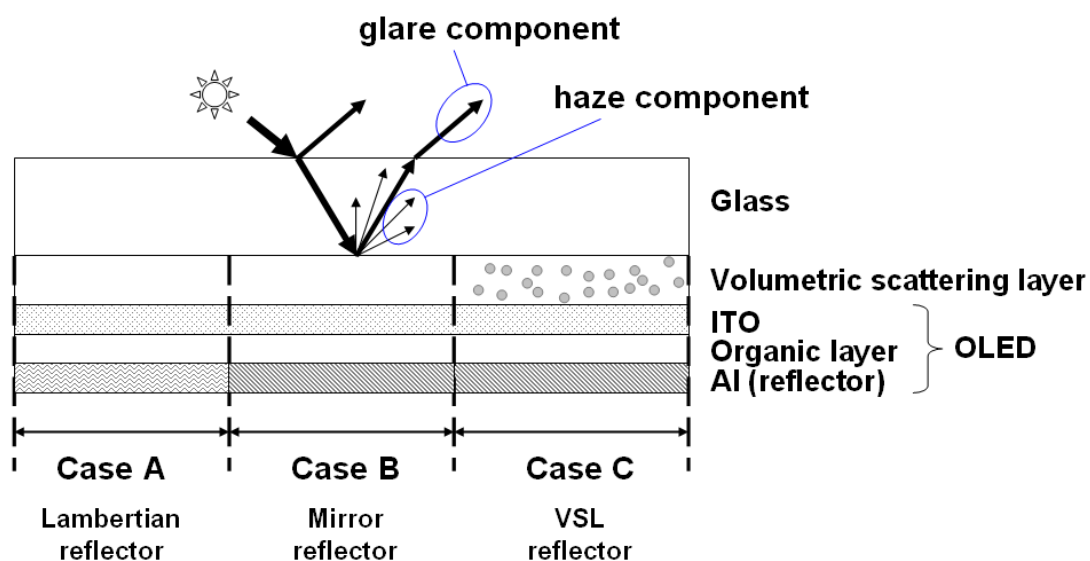


Fig. 6-13 Three conditions for comparing the haze component.

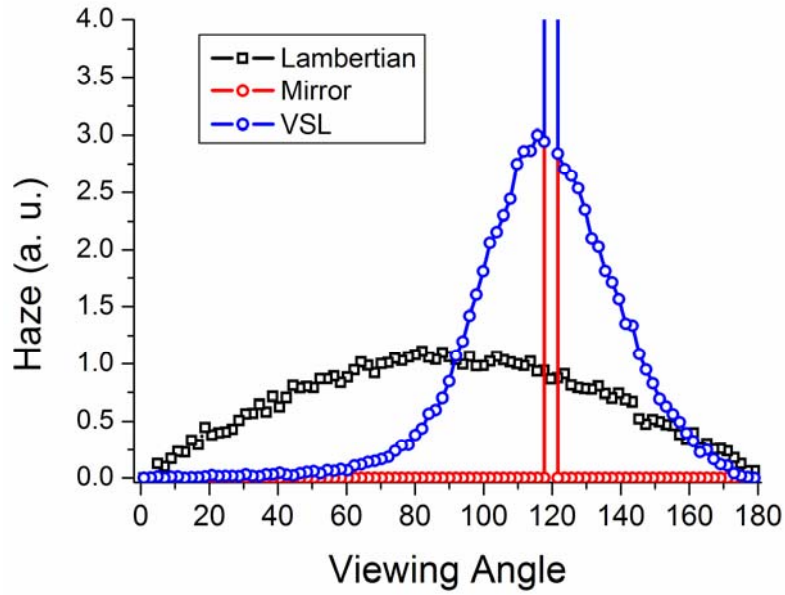


Fig. 6-14 Simulated haze component in Lambertian, mirror, and the VSL cases.

6.5.3 Experimental results

To verify that the VSL is constructed as what we expected, we photographed the surface and cross section with focus ion beam assisted scanning electron microscopy (FIB/SEM). The results are shown in Fig. 6-15, where the surface has bumpy structure for scattering the ambient light in reflective mode, and the cross-section has volumetric scattering centers to extract the wandering light in the OLED section.

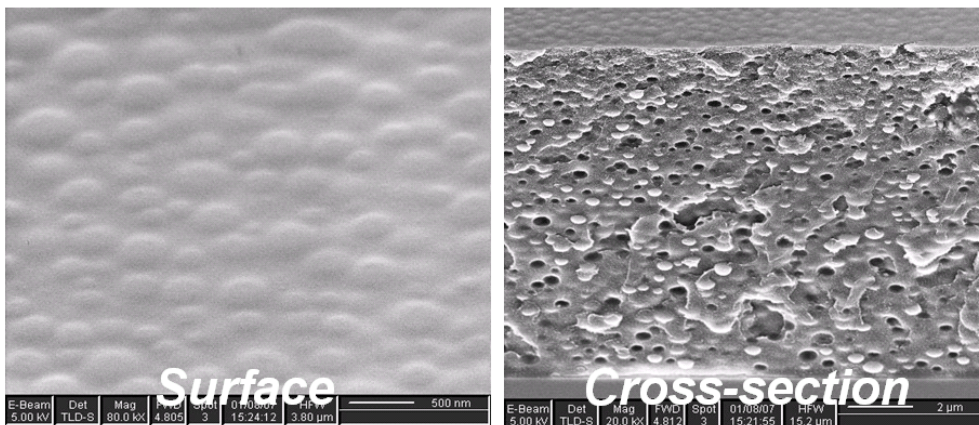


Fig. 6-15 SEM images of VSL at the surface and cross-section.

With the VSL, the R-LCD shows a contrast ratio enhancement by a factor of 12. To visualize the haze component enhancement, we photograph an R-LCD incorporating with a freestanding mirror and a VSL at a non-glare angle as shown in Fig. 6-16. The image reflected by the VSL is much brighter than that reflected by a freestanding mirror.

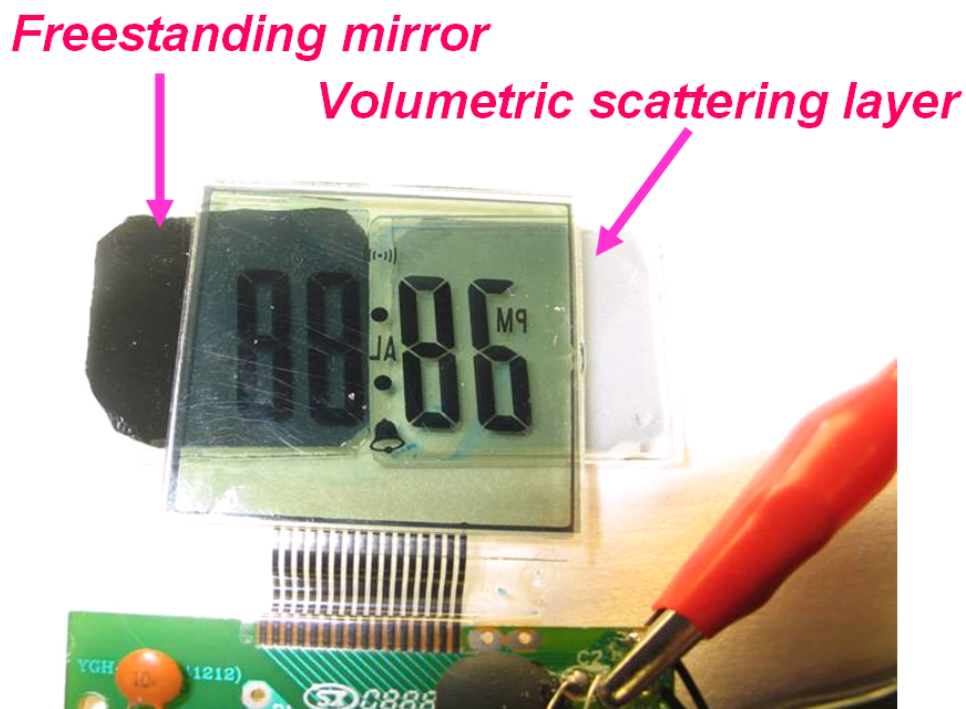


Fig. 6-16 Photograph of LCD with and without adopting VSL.

To examine the influence of VSL in the transmission mode, we further adopt it onto the commercial cell-phone panel. As shown in Fig. 6-17, the white dashed square is the area where the VSL is placed, there is not significant difference in terms of contrast ratio after placing the VSL on the cell-phone panel (no matter in the sparse or dense case). We further measure the contrast ratio as shown in table 6-1. The results show that though the brightness of bright state is lowered, the dark state is lowered as well, which results in no significant deceasing of contrast ratio.

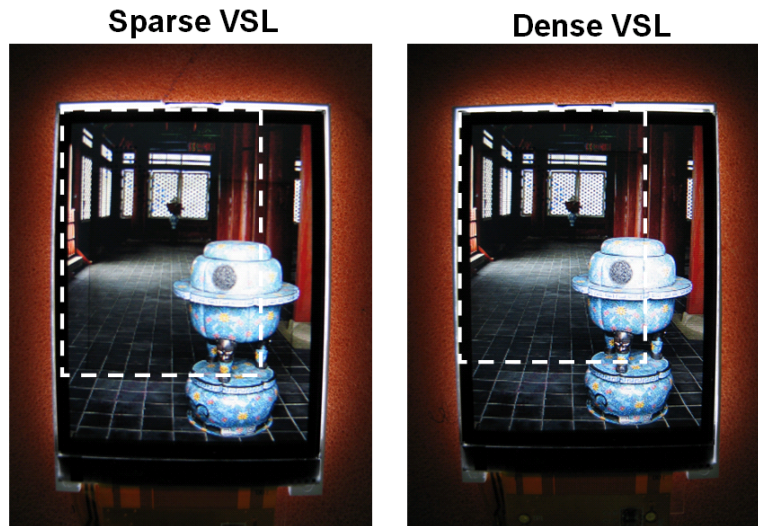


Fig. 6-17 The transmission mode of adopting sparse and dense type VSLs. The dash line indicates the area of VSL.

Table 6-1 The transmission mode without and with different cases of VSL

	W/O VSL	With VSL (dense)	With VSL (sparse)
Bright state	273	223	260
Dark state	1.55	1.348	1.56
Contrast ratio	176	165	167
Gain factor	1	0.94	0.95

6.6 Summary

In this experiment, the integration of OLED and RLCD without intermediate glass lid is successfully realized. This device provides more possibility for display applications, which is because the OLED can be used as a backlight or a display. If the OLED is used as a display (or a regional backlight), each illuminating area can be turned off to show the complete dark state. This function greatly increases the contrast ratio and decreases the power consumption.

We have used the VSL as a translector in the display device, which can enhance not only the output-coupling-efficiency but also the visibility under the sunlight

ambience. To achieve a higher visibility under the sunlight ambience, the optical compatibility between the particle size, particle concentration, and the medium refractive index shall be further optimized.



Chapter 7

Conclusion and future work

7.1 Conclusions

To explore the ultimate features in LCD devices, we have reported three main topics on the scales of LC cell and backlight device, including the fast-switching symmetric H state in a pi-cell, the high-brightness relaxed bend state in the OCB-LCD, and the slim-form-factor emi-flective LCD with embedded OLED backlight. All of them are in the theme of advanced LCD technology for future display applications, as summarized in Fig. 7-1.

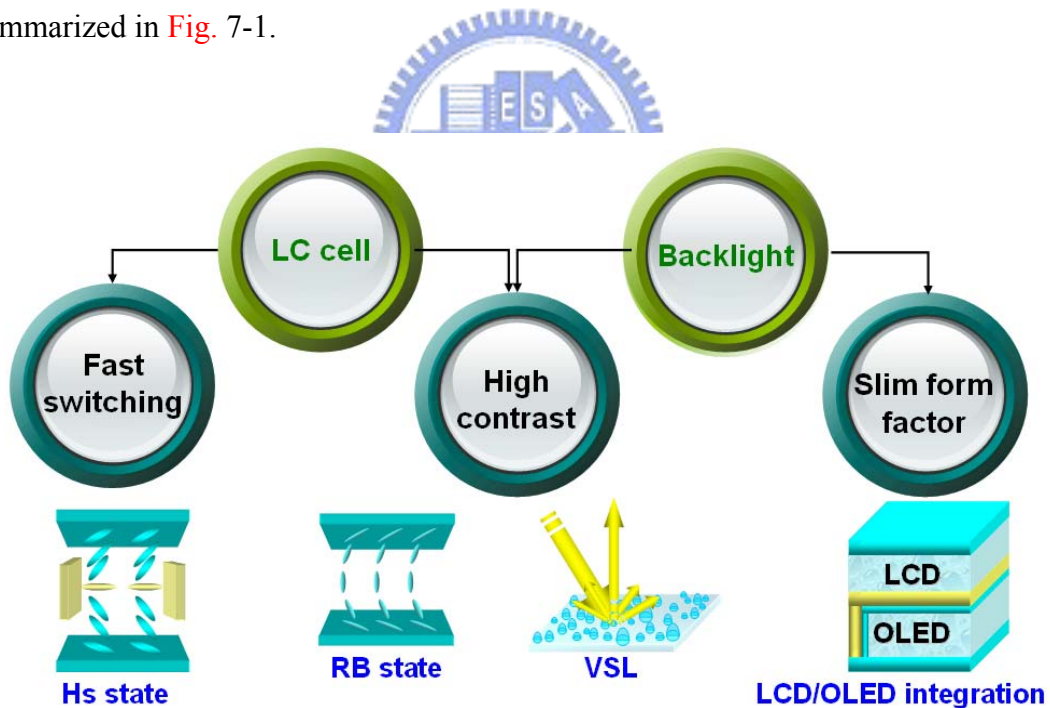


Fig. 7-1 The research topics explored and concluded in this thesis.

7.1.1 Investigating the fast-switching symmetric H state

The Hs state has been reported to have sub-millisecond response times; however, no direct evidence has been obtained to show the profile symmetry. The difficulty in

proving this symmetric structure results from the short lifetime of the Hs state (typically around a few tens ms). In the work reported here, we utilize a burst driving method along with stroboscopic illumination from blue and red LEDs to capture conoscopic images for the Hs director profile; these data agree with our modeling. As summarized in Fig. 7-2, this result is a breakthrough in observing the transient states in an LCD device directly.

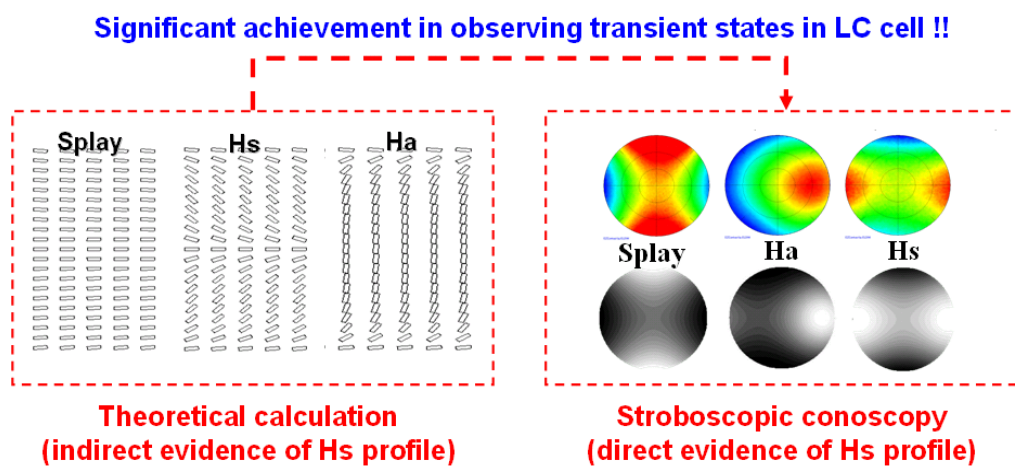


Fig. 7-2 Stroboscopic conoscopy is the first method verifying the transient profile of Hs state.

This observation has confirmed the symmetric profile of the Hs state. With this result, we further propose to use polymer wall to stabilize the central LC director. As shown in Fig. 7-3, we design the polymer structure and simulate the lifetime extension of the Hs state. The result shows that the lifetime can be extended by a factor of more than 10. Subsequently, we set up a UV-LED projection system to form the polymer wall structure. Although the lifetime extension has not been realized at present, the flow effect, collapsing mechanism, and prototype of polymer wall assisted pi-cell have been presented in this thesis. These results will be very helpful for the following experiments.

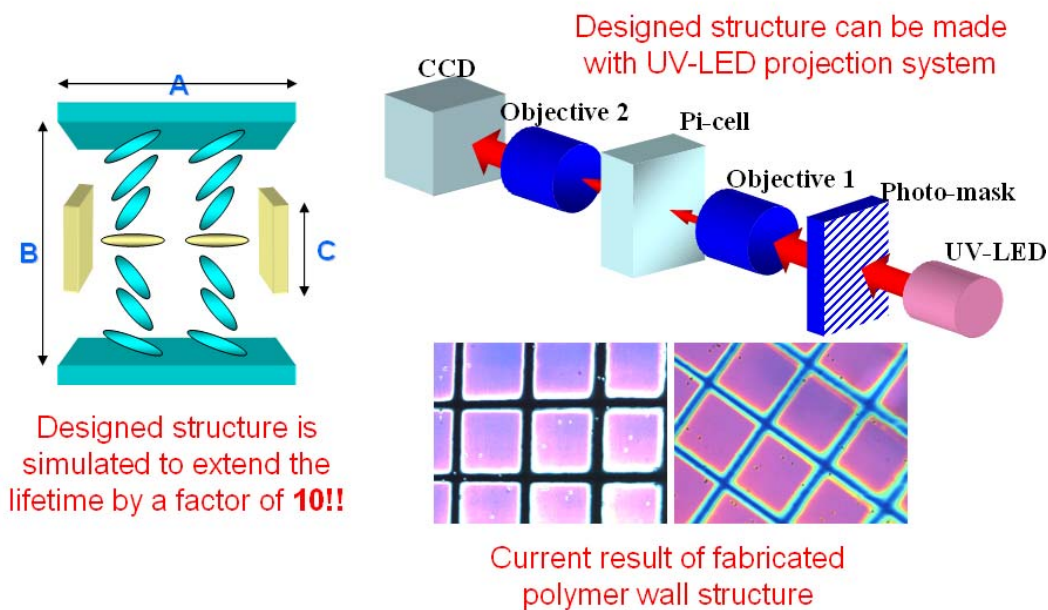


Fig. 7-3 The polymer wall structure designed for extending the Hs lifetime has been simulated and fabricated.

7.1.2 Stabilizing the high-brightness relaxed bend state

We have demonstrated a synchronized polymer-stabilization technique, which can be used to stabilize the non-permanent states in LC devices. In Fig. 7-4, the non-permanent relaxed bend state has the highest brightness among the bend states, and it is observed and stabilized by our proposed technique. This fabricated pi cell has the attributes of high intensity operational range (an enhancement is obtained by a factor of 1.5 compared with the best case of the conventionally polymerized pi cell) and feasibility for full dynamic range optical compensation.

The conventional polymerization was used to fix the LC director to prevent the recovery; however, the switching freedom of the director is also decreased (i.e. the contrast ratio is lowered). The initially-twisted pi-cell avoided the reduction of switching freedom, yet the pi-cell related to the twist motion made the response time increased. In addition, the optical compensation used for the bend state is different from that for the twist state; therefore, the compensation design for the

initially-twisted pi-cell is not effective for its full operational range. On the contrary, as compared in [table 7-1](#), the relaxed bend stabilized pi-cell does not have these issues. Because this pi-cell is stabilized in a “relaxed bend” profile, there is no twist state or switching freedom suppression. Namely, in the relaxed bend stabilized pi-cell, there is no recovery issue, and the optical compensation is valid for full operational range; moreover, the contrast ratio is not degraded.

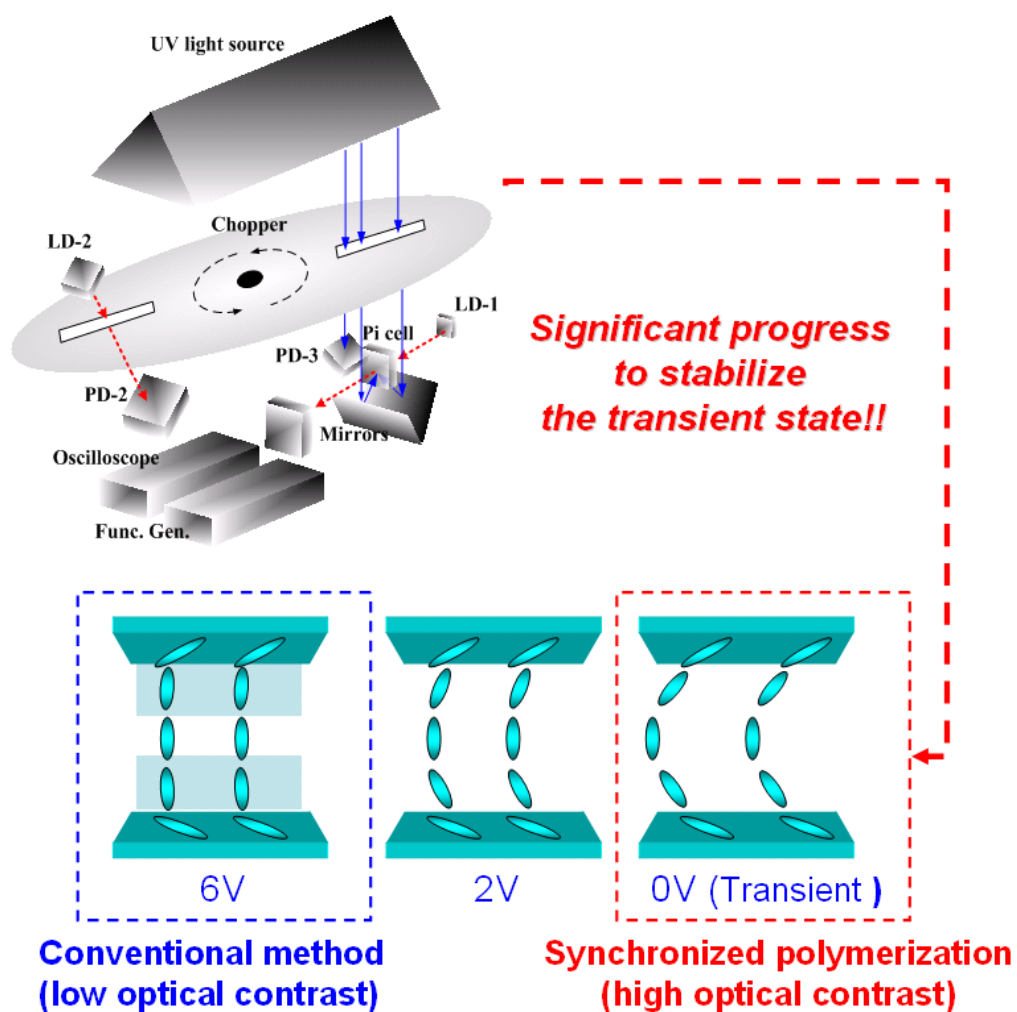


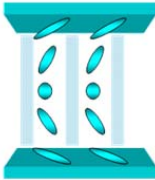
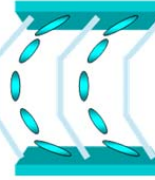


Fig. 7-4 The high-brightness relaxed bend state has been stabilized by our proposed synchronized polymerization.

Table 7-1 Comparison of different pi-cells.

Pi-cells	Normal	Conventionally Polymerized	Initially-twisted	RB stabilized
LC profile				
Inventor	P. J. Bos & T. Uchida	L. C. Chien	J. C. Kim (Pusan)	NCTU/Oxford
Recovery	With	Without	Without	Without
Response	⊙	○	X	○
Contrast ratio	○	X	○	○
Fabrication	⊙	○	△	○
Optical compensation	△	⊙	△	⊙

⊙ : Excellent ○ : Good △ : Acceptable X : Poor

7.1.3 Embedding the OLED backlight into an LCD cell

Directly embedding an OLED into an LC cell has been carried out in this thesis. This is the first result integrating the OLED and LCD without intermediate glass lid, as shown in Fig. 7-5. By adopting the thin-film-encapsulation in OLED, the low-temperature-alignment process in LCD, and the photo-spacer at the intermediate junction, the integrated OLED is fully operational, and the contrast ratio of 5000:1 at the viewing cone of 50° can be achieved in the emissive mode.

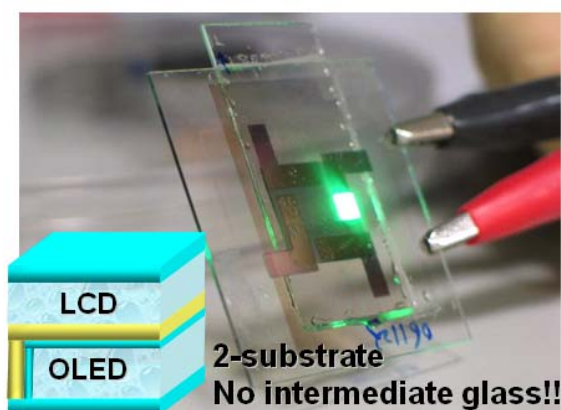


Fig. 7-5 The OLED and LCD have been successfully integrated.

To enhance the image quality of both R-LCD and OLED sections, we propose to lay a volumetric scattering layer (VSL) in the intermediate section of the hybrid device. As shown in Fig. 7-6, the VSL is demonstrated to enhance the contrast ratio in reflective mode by a factor of 12 compared with the freestanding mirror; in addition, the contrast in the transmissive mode is not degraded.

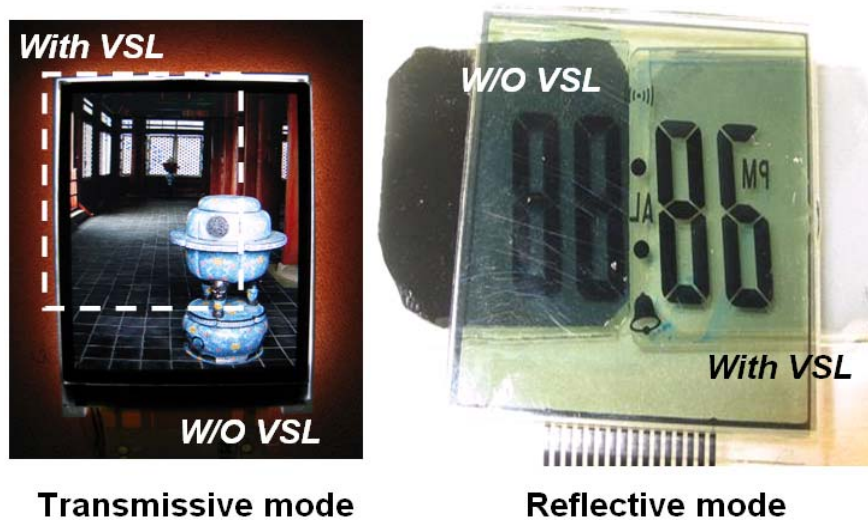
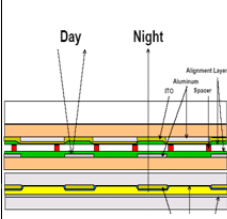
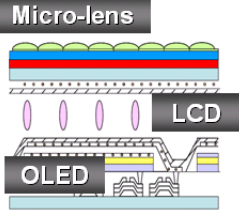
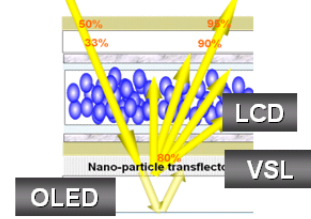


Fig. 7-6 The VSL demonstration in the transmissive and reflective modes.

Compared with the other proposed structures of OLED/LCD integrated device, the emi-flective device has much superiority. As summarized in table 7-2, in the structure of tandem and emi-flective LCD/OLED devices, because the LCD and OLED are integrated rather than stacked, they need only 2 substrates and 1 TFT driving plane. This structure makes the OLED as a locally dimming backlight to increase the contrast ratio and decrease the power consumption. In addition, by adopting the VSL, the emi-flective device can simultaneously increase the light-out- coupling efficiency of OLED section and the sunlight visibility of reflective LCD section. Because the VSL is transparent, the aperture ratio can be kept to 100% in both reflective and emissive modes, whereas the reflector in conventional transflective device blocks the transmissive light and decreases the aperture ratio. Moreover, the VSL is dispersive;

therefore, its viewing angle is superior to that of the tandem LCD/OLED (the application of micro-lens makes the viewing angle narrowed).

Table 7-2 Comparison of proposed OLED/LCD device structures.

items	Transflective LCD/OLED	Tandem LCD/OLED	Emi-flective LCD/OLED
Structure			
Inventor	E. Lueder	S. T. Wu	NCTU
substrates	4	2	2
TFT planes	2	1	1
Aperture ratio	50%	100%	100%
Contrast ratio	X	○	◎
Power consumption	○	◎	◎
Viewing angle	△	△	○

◎ : Excellent ○ : Good △ : Acceptable X : Poor

7.2 Future works

The future work is proposed on four aspects, including the follow-up implementation of relaxed bend state for manufacturing, incorporation of the symmetric H state for dynamic backlight display application, fabrication of the thoroughly flexible emi-flective LCD, and integration of all the results that we obtained in this thesis to make a slim-form-factor and low-power-consumption LCD.

7.2.1 Implementing the synchronized polymerization into actual LCD

The synchronized polymerization for stabilizing the relaxed bend state in a pi-cell can be adopted into the actual LCD manufacturing process. The only difference of the

cell preparation between the general process (as shown in Fig. 7-7, the standard process provided by AUO) and the new process is that the LC material shall mix with reactive mesogen, and the LC cell shall be exposed under the UV light with simultaneous impulse driving. The material used in the step of “LC filling” shall be replaced with monomer mixed LC, and the step of “assembly” shall include the UV expose to polymerize the monomer inside the LC cell. With these two extra steps, the relaxed bend state stabilized pi-cell can be adopted into the mass production process.

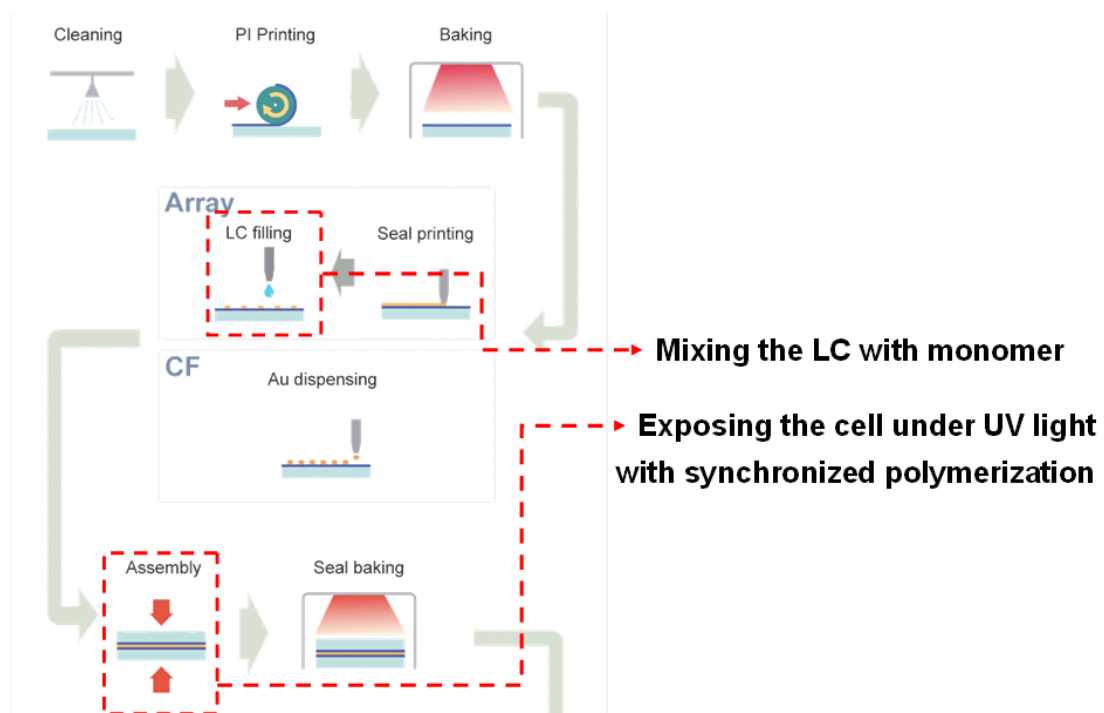


Fig. 7-7 The implementation of RB stabilization into actual LCD processes.

7.2.2 Incorporating symmetric H state with flashing backlight

To utilize the Hs state into the current display applications, locally dimming backlight can be an option to avoid its short lifetime issue. As shown in Fig. 7-8, the LC cell can be turned on synchronously with the flashing backlight. This proposed method is well-adopted in high-dynamic-range backlight applications, and it can also prevent the Hs state from collapsing into Ha state.

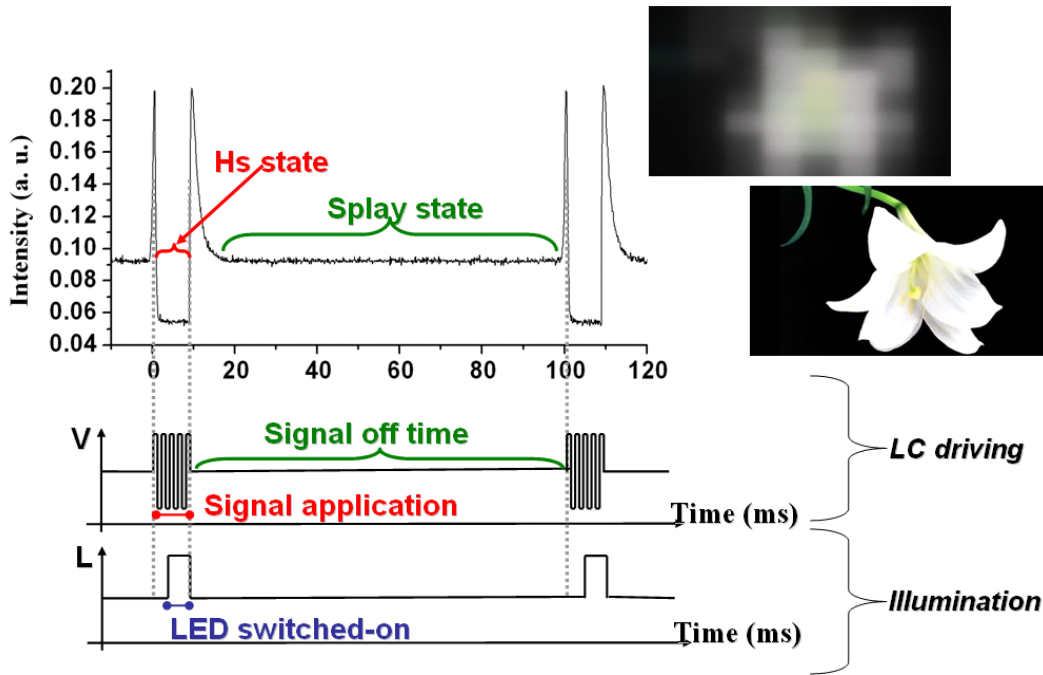


Fig. 7-8 Utilizing the flashing backlight technique along with the burst driving method to realize the application of the Hs state pi-cell.

7.2.3 Fabricating the thoroughly flexible emi-flective LCD

To realize a flexible transfective display, all components have to be flexible including the backlight as well. By replacing the backlight module with the OLED, we have demonstrated the feasibility of a high performance and potentially flexible emi-flective display. Moreover, the VSL that we have proposed in this thesis is also capable of being flexible; hence, with the integration of flexible LCD, flexible OLED, and flexible VSL, we can make a thoroughly flexible emi-flective LCD, as depicted in Fig. 7-9.

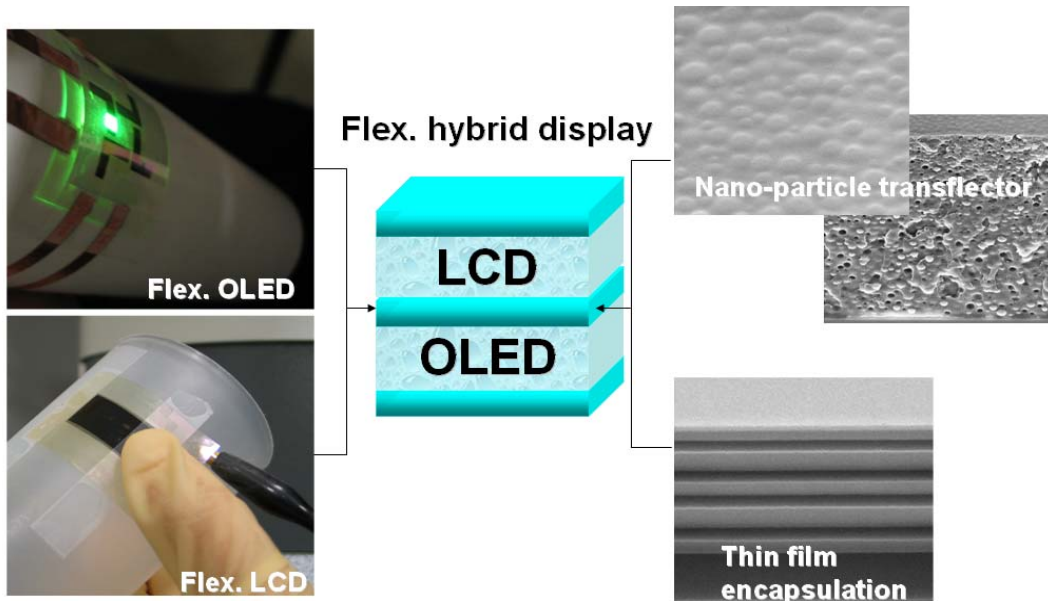


Fig. 7-9The proposed structure of entirely flexible emi-reflective LCD.

7.2.4 Integration of fast switching OCB-LCD with embedded OLED

By integrating all of the results that we have obtained in this thesis including the fast-switching OCB-LCD (using relaxed bend state or symmetric H state), the volumetric scattering layer, and the embedded OLED, we will be able to fabricate a high performance device. As shown in Fig. 7-10, because of the utilization of embedded backlight, the form factor of the device can be significantly reduced; besides, the embedded OLED can also be used as a regionally flashing backlight; the contrast ratio can thus be largely increased. With the adoption of fast-switching LC mode, the field-sequential-color LCD technology can be incorporated, which is plausible to increase the device power efficiency by a factor of 3. With the further adoption of VSL, the sunlight visibility and light-out-coupling efficiency can be improved concurrently. Moreover, all of the components mentioned here are capable of being flexible; therefore, combing all of the results that we have obtained in this thesis, we will be able to make a flexible LCD with the attributes of high image quality, low power consumption, and slim form factor.

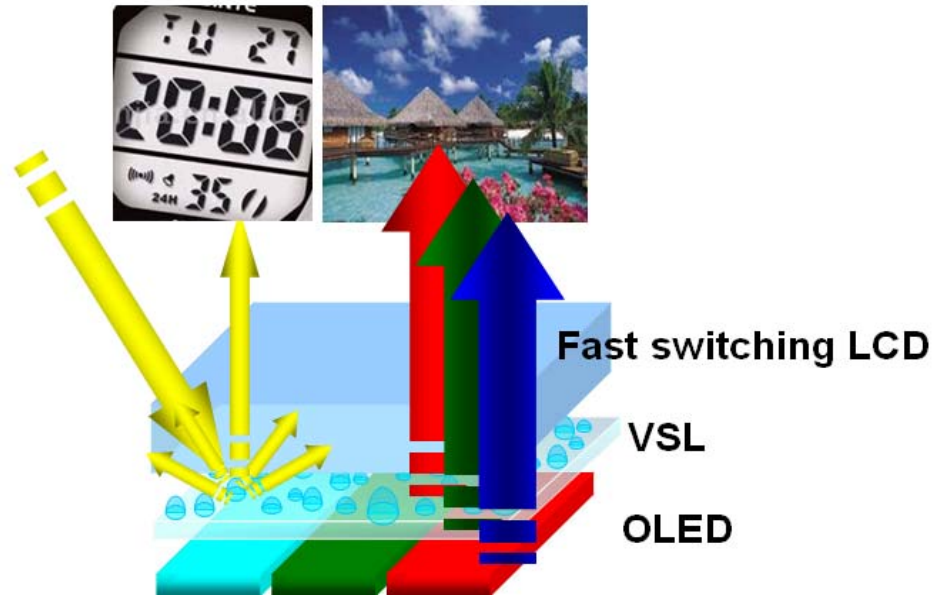


Fig. 7-10 The proposed device structure adopting all of the results obtained in this thesis.



References

1. L. F. Weber, SID Symposium Digest **31**, 402 (2000).
2. W. D. Kesling and C. E. Hunt , J. Vac. Sci. Technol. B **11**, 518 (1993).
3. C. W. Tang, M. K. Hatalis, M. J. Stewart, and J. Burtis. , Proc. SPIE **3057**, 277 (1997).
4. G. Gu, D. Z. Garbuzov, P. E. Burrows, S. Venkatesh, S. R. Forrest, and M. E. Thompson , Opt. Lett. **22**, 396 (1997).
5. M.V.C. Stroomer, M.J. Powell, B.C. Easton, and J.A. Chapman, Electron. Lett. **18**, 858 (1982).
6. K. Katoh, M. Yasui, S. Kuniyasu, and H Watanabe, Electron. Lett. **19**, 506 (1983).
7. Figures retrieved from website of Wikipedia, CMO, CPT, and AUO companies.
8. V.r K. Nilsen, C. O. Miremont, and I. Underwood, Proc. SPIE **4435**, 167 (2001).
9. S. Vetrov, G. M. Zharkova, V. M. Khachatryan, A. Korets, A. Sadreev, and V. F. Shabanov, Proc. SPIE **2731**, 183 (1996).
10. A. Khan, T. Schneider, E. Montbach, D. J. Davis, N. Miller, D. Marhefka, T. Ernst, and J. W. Doane, J. Soc. Inf. Display **16**, 245 (2008).
11. C.-H. Lin, Appl. Phys. Lett. **90**, 151112 (2007).
12. Tahata, A. Tsumura, M. Mizunuma, A. Tamatani, Y. Morii, M. Fujii, and F. Matsukawa, Proc. SPIE **3015**, 134 (1997).
13. T. Ishinabe, T. Miyashita, and T. Uchida, J. Soc. Inf. Display **6**, 243 (1998).
14. M. J. Towler and E. P. Raynes, Proceedings of the 22nd International Display Research Conference (Eurodisplay '02), Nice, France, **2**, 877 (2002).
15. Website of SHARP Company.
16. P. J. Bos and K. R. Koehler-Beran, Mol. Cryst. Liq. Cryst. **113**, 329 (1984).
17. F.C. Lin, C.Y. Liao, L.Y. Liao, Y.P. Huang, and H.P. D. Shieh, Proceedings of the Digest of Technical paper of SID International Symposium **38**, 1343 (2007).
18. H. Nakamura, K. Miwa, M. Noguchi, Y. Watanabe, J. Mamiya, J. Watanabe, Y. Nishiura, and Y. Shinagawa, Proceedings of the Digest of Technical paper of SID International Symposium **29**, 143 (1998).
19. K. H. Choi, T.-H. Jung, D. W. Choi, J. E. Park, T. S. Kim, and K. D. Kim, Proceedings of the Digest of Technical paper of SID International Symposium **37**,

- 713 (2006).
20. F. C. Frank, *Discuss. Faraday Soc.* **25**, 19 (1958).
 21. H. C. Tseng, Dayton L. Silver, and Bruce A. Finlayson, *Phys. Fluids* **15**, 1213 (1972).
 22. D. W. Berreman, *J. Chem. Phys.* **62**, 776 (1975).
 23. E. Lueder, "Liquid Crystal Displays," published by Wiley LTD (2001).
 24. A. Muravsky, A. Murauski, V. Mazaeva, and V. Belyaev, *J. Soc. Infor. Disp.* **13**, 349 (2005).
 25. H. Gruler and L. Cheung, *J. Appl. Phys.* **46**, 5097 (1975).
 26. J. Nehring, A. R. Kmetz, and T. J. Scheffer, *J. Appl. Phys.* **47**, 850 (1976).
 27. N. Nagae, T. Miyashita, T. Uchida, *SID Symposium Digest* **31**, 26 (2000).
 28. X. D. Mi, M. Xu, D.-K. Yang, and P. J. Bos, *SID Symposium Digest* **30**, 24 (1999).
 29. H. Kikuchi, H. Yamamoto, H. Sato, M. Kawakita, K. Takizawa, and H. Fujikake, *Jpn. J. Appl. Phys., Part 1* **44**, 981 (2005).
 30. P. Yeh, *J. Opt. Soc. Am.* **72**, 507 (1982).
 31. A. Lien, *Appl. Phys. Lett.* **57**, 2767 (1990).
 32. H. Mori and P. J. Bos, *Jpn. J. Appl. Phys., Part 1* **38**, 2837 (1999).
 33. H. Mori and P. J. Bos: *SID Symposium Digest* **29**, 830 (1998).
 34. J. Chen, K.-H. Kim, J.-J. Jyu, J. H. Souk, J. R. Kelly and P. J. Bos: *SID Symposium Digest* **29**, 315 (1998).
 35. T. Uchida and T. Ishinabe, *J. Soc. Inf. Display* **12**, 309 (2004).
 36. T. Ishinabe, T. Miyashita, and T. Uchida, *SID Symposium Digest* **31**, 1094 (2000).
 37. P. van de Witte, S. Stallinga and J. A. M. M. van Haaren, *Jpn. J. Appl. Phys.* **39** 101 (2000).
 38. T. Ishinabe, T. Miyashita, and T. Uchida, *SID Symposium Digest* **29**, 774 (1998).
 39. T. Ishinabe, T. Miyashita, and T. Uchida, *J. Soc. Inf. Display* **6**, 243 (1998).
 40. Prof. Y. P. Huang's lecture note in Display Institute, National Chiao tung University, Taiwan.
 41. P. E. Burrows, V. Bulovic, V. G. Kozlov, Z. Shen, S. R. Forrest, and M. E.

- Thompson, Proc. SPIE **3148**, 252 (1997).
42. J. K. Mahon, T. X. Zhou, P. E. Burrows, S. R. Forrest, and M. E. Thompson, Proc. SPIE **3279**, 87 (1998).
43. M. K. Hatalis, M. J. Stewart, C. W. Tang, and J. Burtis, Proc. SPIE **3057**, 277 (1997).
44. Z. Xie, C. Qiu, H. Chen, B. Tang, M. Wong, and H.-S. Kwok, SID Symposium Digest **34**, 512 (2003).
45. G. Nisato, M. Kuilder, P. Bouten, L. Moro, O. Philips, and N. Rutherford, SID Symposium Digest **34**, 550 (2003).
46. C. H. Yi, Y. K. Lee, S. M. Lee, S. H. Ju, E. J. Lee, Y. M. Choo, K. C. Park, and J. Jang, SID Symposium Digest **35**, 715 (2004).
47. B. B. Kosmowski, M. E. Becker, and J. Neumeier, Proc. SPIE **145**, 448 (1993).
48. M. E. Becker, J. Soc. Inf. Display **5**, 283 (1997).
49. M. E. Becker, Proc. SPIE **3636**, 170 (1999).
50. M. E. Becker, J. Laur, and J. Neumeier, SID Symposium Digest **32**, 322 (2001).
51. H. Woehler and M. E. Becker, Proc. SPIE **4759**, 359 (2002).
52. J. H. Lee, X. Zhu, Y. H. Lin, W. K. Choi, T. C. Lin, S. C. Hsu, H. Y. Lin, and S. T. Wu, Opt. Express **13**, 9431 (2005).
53. Information from J.A. Woollam Ellipsometers company.
54. Y. Ohno, T. Ishinabe, T. Miyashita, and T. Uchida: SID Int. Symp. Dig. Tech. Pap. **36**, 784 (2005).
55. Y. Ohno, T. Ishinabe, T. Miyashita, and T. Uchida, Jpn. J. Appl. Phys. **47**, 969 (2008).
56. S. T. Wu and A. M. Lackner, Appl. Phys. Lett. **64**, 2047 (1994).
57. C. L. Kuo, T. Miyashita, M. Suzuki, and T. Uchida, Appl. Phys. Lett. **68**, 1461 (1996).
58. E. J. Acosta, M. J. Towler, and M. D. Tillin, J. Appl. Phys. **97**, 093106 (2005).
59. S. H. Lee, S. H. Hong, J. D. Noh, H. Y. Kim, and D.S. Seo, Jpn. J. Appl. Phys. **40**, L389 (2001).
60. M. J. Towler and E. P. Raynes, Proceedings of the 22nd International Display Research Conference (Eurodisplay '02), Nice, France, **2**, 877 (2002).
61. S. H. Kim and L.C. Chien, Jpn. J. Appl. Phys. **43**, 7643 (2004).

62. F. S. Yeung and H.-S. Kwok, Appl. Phys. Lett. **88**, 063505 (2006).
63. K. H. Choi, T.-H. Jung, D. W. Choi, J. E. Park, T. S. Kim, and K. D. Kim, Proceedings of the Digest of Technical paper of SID International Symposium **37**, 713 (2006).
64. Y. Sun, H. Ma, Z. Li, Z. Zhang, and R. Guan, Appl. Phys. Lett. **90**, 091103 (2007).
65. S. R. Lee, J.H. Shin, J.I. Baek, M.C. Oh, T.H. Yoon, and J. C. Kim, Appl. Phys. Lett. **90**, 163513 (2007).
66. C.Y. Huang, R.X. Fung, Y.G. Lin, and C.T. Hsieh, Appl. Phys. Lett. **90**, 171918 (2007).
67. H. Mori, IEEE/OSA Journal of Display Technology **1**, 179 (2005).
68. P. D. Brimicombe, L. A. Parry-Jones, S. J. Elston, and E. P. Raynes, J. Appl. Phys. **98**, 104104 (2005).
69. P. Brimicombe, S. J. Elston, and E. P. Raynes, Liquid Crystals **34**, 641 (2007).
70. F.C. Lin, C.Y. Liao, L.Y. Liao, Y.P. Huang, and H.P. D. Shieh, Proceedings of the Digest of Technical paper of SID International Symposium **38**, 1343 (2007).
71. H. G. Walton and M. J. Towler, Liq. Cryst. **27**, 1329 (2000).
72. C. Y. Huang, R. X. Fung, Y. G. Lin and C. T. Hsieh, Appl. Phys. Lett. **90**, 171918 (2007).
73. M. D. Tillin, E. P. Raynes and M. J. Towler, U.S. Patent No. 6,222,605
74. F. S. Yeung, Y. W. Li and H.-S. Kwok, Appl. Phys. Lett. **88**, 041108 (2006).
75. F. S. Yeung and H.-S. Kwok, Appl. Phys. Lett. **88**, 063505 (2006).
76. P. D. Brimicombe and E. P. Raynes, Appl. Phys. Lett. **89**, 031121 (2006).
77. P. D. Brimicombe and E. P. Raynes, Liq. Cryst. **32**, 1273 (2005).
78. W. C. Oseen, Trans. Faraday Soc. **29**, 883 (1933).
79. F. C. Frank, Discuss. Faraday Soc. **25**, 19 (1958).
80. C. Gu and P. Yeh, DISPLAYS **20**, 237 (1999).
81. Y. Kim, and J. L. West, Appl. Phys. Lett. **72**, 2253 (1998).
82. B. R. Yang, S. J. Elston, P. Raynes, H. P. D. Shieh, Appl. Phys. Lett., **92**, 221109 (2008).
83. E. Lueder, M. Randler, H. Schenk, and E. Kluge. SID Int. Symp. Dig. Tech. Pap.

- 2 (2000), p. 1025.
84. A. Mosley, J. Burrage, N. Conway, M. Halim, S. Latham, J. Pommerehne, and P. Rundle. SID Int. Symp. Dig. Tech. Pap. **1** (2001), p.298.
85. H. P. D. Shieh. Proc. IEEE Conf. Laser and Electro-Optics Society 650 (2005).
86. J. H. Lee, X. Zhu, Y. H. Lin, W. K. Choi, T. C. Lin, S. C. Hsu, H. Y. Lin, and S. T. Wu. Opt. Express **13** (2005), p. 9431.
87. M. Kimura: U.S. Patent Application 20020196387 (2002).
88. Fujieda: U.S. Patent Application 20030201960 (2003).
89. Y. J. Tung: U.S. Patent 6900458 (2005).
90. B. R. Yang, K. H. Liu, and H. P. D. Shieh. Jpn. J. Appl. Phys. **46** 182 (2007).
91. G. Nisato, M. Kuilder, P. Bouten, L. Moro, O. Philips, and N. Rutherford, SID Symposium Digest **34**, 550 (2003).
92. L. L. Moro, T. A. Krajewski, N. M. Rutherford, O. Philips, R. J. Visser, M. E. Gross, W. D. Bennett, and G. L. Graff, Proc. SPIE **5214**, 83 (2004).
93. C. H. Yi, Y. K. Lee, S. M. Lee, S. H. Ju, E. J. Lee, Y. M. Choo, K. C. Park, and J. Jang, SID Symposium Digest **35**, 715 (2004).
94. F. J. H. van Assche, R. T. Vangheluwe, J. W. C. Maes, W. S. Mischke, M. D. Bijker, F. C. Dings, M. F. J. Evers, W. M. M. Kessels, and M. C. M. van de Sanden, SID Symposium Digest **35**, 695 (2004).
95. H. Lifka, H. A. van Esch, and J. J. W. M. Rosink, SID Symposium Digest **35**, 1384 (2004).
96. M. E. Becker, J. Laur, and J. Neumeier. SID Int. Symp. Dig. Tech. Pap. **1**, 322 (2001).
97. M. E. Becker. J. Soc. Inf. Disp. **13**, 81 (2005).
98. M. E. Becker. J. Soc. Inf. Disp. **14**, 1003 (2006).
-

Bo-Ru Yang's resume

楊柏儒的履歷

Postal: Room 502, CPT building, 1001 Ta-Hsueh Road, Hsin-chu, Taiwan.

E-mail: Ybr.eo93g@nctu.edu.tw.

Mobile: 0928018147

Education:

- 2008 summer **PhD visiting, Tohoku University, Japan (日本東北大學)**
- "OCB-LCD" at **Prof. Tatsuo Uchida's group**.
- 2007-2008 **PhD visiting, University of Oxford, United Kingdom (英國牛津大學)**
- "Fast switching LCD" at **Prof. Peter Raynes's group**.
 - Two publications in A-class journal, two presentations in conferences, one patent filed
- 2004-2008 **PhD (Opto-electronic engineering), National Chiao Tung University, Taiwan (交通大學)**
- "Portable Emi-flective LCD/OLED" at **Prof. Han-Ping D. Shieh's group**.
 - Three publications in journal, three presentations in conference, one patent granted
- 2004-2008 **MBA program for international students, National Chiao Tung University (交通大學)**
- Completed many team reports with international classmates
- 2002-2004 **M. S. (Material science and engineering), National Tsing Hua University, Taiwan (清華大學)**
- "Nano-technology executed by near-field optoelectronic microscopy"
- 1998-2002 **B. S. (Material science and engineering), NCTU, Taiwan (交通大學)**
- "GaAs semiconductor technology"

Academic awards:

- 2008 **Scholarship for visiting Tohoku University provided by Interchange Association, Japan**
- Received a two-month allowance for studying at Tohoku University
- 2007 **Scholarship for visiting Univ. of Oxford provided by National Science Council, Taiwan**
- Received an one-year allowance for studying at Univ. of Oxford
- 2007 **Distinguished researcher award**
- Awarded to 10 out of 150 PhD students in Institute of Electro-Optical Engineering, NCTU
- 2006~2008 **Society for Information Display (SID) 2006, 2007, 2008 student travel grants**
- Nominated as distinguished student paper award in 2007
- 2005 **Applied Materials Scholarship**
- Awarded to 10 out of 400 applicants for visiting Silicon Valley companies, UC Berkley, and Stanford University

Work experience:

- 2005 **Summer Intern, Industrial Technology and Research Institute (ITRI), Taiwan**
- Chief inventor of TW patent #287142 on LCD field.
- 2004 **Summer Intern, Chunghwa Picture Tube (CPT), Taiwan**
- Had a patent filed in TW, CN, and US.
- 1998-2004 **High school tutor, Taiwan**

Leadership:

- 2008 **Completion of lectures on "building a business" at SAID Business School in University of Oxford**
- 2006 **Project leader, Acer's Entrepreneurship Contest**
- Grouped a team with multidisciplinary background to come up with a project for Acer
- 2000 **President, hip-hop dancing club of National Chiao Tung University**
- Led 90 members to make demonstrations, dancing camps, and sponsored performances

Skills:

Computing Language Liquid crystal simulation programs, C++, Matlab, Office, Origin, and Photo-impact
Chinese (native), English (fluent), Japanese (conversational)



Bo-Ru Yang's publication list

Journal papers

1. **B.R. Yang**, S. J. Elston, P. Raynes, H.P. D. Shieh, "High-Brightness Relaxed Bend State in a Pi-cell stabilized by Synchronized Polymerization", *Appl. Phys. Lett.* **92**, 221109 (2008).
2. **B.R. Yang**, S. J. Elston, P. Raynes, and H.P.D. Shieh, "Investigation of the transient symmetric H state in a pi cell", *Appl. Phys. Lett.*, **91**, 071119 (2007).
3. **B.R. Yang**, Kang-Hung Liu, Shih-Nan Lee, Jen-Chieh Hsieh, Han-Ping D. Shieh, Chin H. Chen, "Volumetric Scattering Layer for Flexible Transflective Display", *Jpn. J. Appl. Phys.*, **47**, 1016 (2008)
4. **B.R. Yang**, K.H. Liu, and H.P. D. Shieh, "Emiflective Display with Integration of Reflective Liquid Crystal Display and Organic Light Emitting Diode" *Jpn. J. Appl. Phys.*, **46**, 182 (2007).
5. **B.R. Yang**, C.W. Hsu, and H.P.D. Shieh, "Emi-Flective Display with Attribute of High Glare-Free-Ambient-Contrast-Ratio", *Jpn. J. Appl. Phys.*, **46**, 7418 (2007).

Conference papers

1. **B.R. Yang**, S. J. Elston, P. Raynes, H.P. D. Shieh, "Stabilization of High-Brightness Relaxed Bend State and Investigation of Fast-Switching Symmetric H State in a Pi-cell by Synchronized Illumination Technique", Society for Information Display 2008 (SID'08) p-174.
2. **B.R. Yang**, S. J. Elston, P. Raynes, H.P. D. Shieh, "Flow effect on the dynamic polymerization", International Liquid Crystal Conference 2008 (ILCC '08) accepted.
3. **B.R. Yang**, K.Y. Lin, H.P. D. Shieh, S.N. Lee, and C.H. Chen, "High Contrast Ratio Emi-flective LCD with Nano-Particle Transflector", Society for Information Display 2007 (SID'07), pp 1813~1816.
4. K.Y. Lin, **B.R. Yang**, and H.P. D. Shieh, "A Novel Pixel Circuit Compensating for Poly-Si Threshold-Voltage Shift and Degradation of OLED for Emi-flective Display" (IDMC'07)
5. S.H. Lin, **B.R. Yang**, and H.P. D. Shieh, "A Novel Pixel Structure for the Emi-flective Hybrid Display System" (SID'06), pp. 902~904
6. C.W. Hsu, **B.R. Yang**, and H.P. D. Shieh, "A Hybrid Display of Organic Electroluminescence Devices and Reflective Liquid Crystal Displays", Taiwan Display Conference 2006 (TDC'06).
7. C.W. Hsu, **B.R. Yang**, and H.P. D. Shieh, "A Hybrid Display of Transflective LCD and OLED" Optics and Photonics Taiwan'04 (OPT'04).

Patents

Granted

楊柏儒, 劉康弘, 王興龍, 鄭協昌, 廖奇璋, 謝漢萍, "自發光反射式液晶顯示器及其製造方法" 中華民國專利 287142 號。

Pending

- [1] **楊柏儒**, 劉康弘, 王興龍, 廖奇璋, 謝漢萍, "自發光反射式液晶顯示器及其製造方法" filed for Taiwan in Sep. 2005
- [2] 韋安琪, **楊柏儒**, 謝漢萍, "有機發光元件之增光膜製作方法" filed for TW in Sep. 2006 (assignee: CPT, 華映)
- [3] **楊柏儒**, 劉康弘, 王興龍, 許傳偉, 簡良吉, 謝漢萍, "以單基板製程製作自發光反射式液晶顯示器" filed for TW in Dec. 2006.
- [4] **B.R. Yang**, S. J. Elston, P. Raynes, H.P. D. Shieh, "Liquid crystal device and method of manufacture thereof" filed for UK in Nov. 2007.